Interplay between magnetism, thermodynamics and diffusion in bcc Fe-Mn alloys : from first principles to finite temperatures

Anton Schneider

université PARIS-SACLAY

NNT : 2019SACLS367

Thèse de doctorat

Corrélations entre le magnétisme, la thermodynamique et la diffusion dans les alliages Fe-Mn cubiques centrés : *des premiers principes aux températures finies*

Thèse de doctorat de l'Université Paris-Saclay
préparée à l'Université Paris Sud,
au sein du Commissariat à l'énergie atomique et aux énergies alternatives

Ecole doctorale n°572 Ondes et Matière (EDOM)
Spécialité de doctorat: Physique

Thèse présentée et soutenue à Gif sur Yvette, le 18 octobre 2019, par

ANTON SCHNEIDER

Composition du Jury :

Dr. Fabienne Berthier Université Paris-Saclay, ICMMO	Présidente
Prof. Dr. Ralf Drautz Ruhr Universität Bochum, ICAMS, Allemagne	Rapporteur
Prof. Lionel Calmels Université de Toulouse 3, CEMES	Rapporteur
Prof. Pavel Korzhavyi KTH Royal Institute of Technology, Stockholm, Suède	Examinateur
Dr. Christian Meny Université de Strasbourg, IPCMS	Examinateur
Dr. Cyrille Barreteau Université Paris-Saclay, CEA-CNRS-SPEC	Directeur de thèse
Dr. Chu Chun Fu Université Paris-Saclay, CEA-SRMP	Encadrante de thèse
Dr. Mikhail Lavrentiev Culham Center for Fusion Energy, Royaume-Uni	Invité

Résumé

Dans les alliages 3*d*, les propriétés magnétiques des solutés peuvent être extrêmement sensibles aux environnements chimiques et structurels locaux. Ainsi, les propriétés de ces solutés sont souvent à l'origine de désaccords entre les différentes études de la littérature, aussi bien théoriques qu'expérimentales. C'est par exemple le cas pour les propriétés magnétiques des solutés de Mn dans le fer cubique centré. D'autre part, les alliages présentant une compétition entre les interactions magnétiques soluté-soluté et soluté-hôte exhibent souvent des structures magnétiques particulièrement complexes. Par ailleurs, de nombreuses études ont montré que le magnétisme dans les alliages de fer joue un rôle crucial sur diverses propriétés thermodynamiques et cinétiques. L'objectif de ce travail est d'identifier et de comprendre le couplage entre les propriétés magnétiques et énergétiques des alliages Fe-Mn cubiques centrés à l'état fondamental, mais aussi à température finie, et d'évaluer les effets du magnétisme sur les propriétés thermodynamiques et cinétiques. Afin de comprendre correctement les propriétés fondamentales de ces alliages, la première partie de ce travail est dédiée à l'étude ab-initio des effets de l'environnement chimique local sur l'état magnétique des solutés de Mn dans le Fe-Mn cubique centré (Théorie de la Fonctionnelle de la Densité). Diverses configurations contenant du Mn, isolé ou sous forme d'amas, en présence de lacunes ou d'impuretés interstitielles sont étudiées. La configuration magnétique de plus basse énergie de chaque configuration atomique est déterminée et des tendances générales sont identifiées. A la lumière des résultats obtenus, une explication possible à des désaccords entre des études expérimentales et théoriques de la littérature est proposée.

Un modèle effectif d'interactions est ensuite paramétré à partir des données *ab-initio* afin d'étudier les propriétés des alliages Fe-Mn à température finie. Les propriétés clés de ces alliages sont identifiées et le modèle est validé à basse température en reproduisant les résultats ab-initio. L'utilisation de ce modèle couplé à des simulations Monte Carlo permet de simuler l'évolution chimique des alliages Fe-Mn en fonction de la température et de la concentration en Mn, tout en relaxant la structure magnétique en temps réel. Afin d'illustrer les possibles applications de ce modèle, diverses propriétés sont étudiées telles que la dépendance en concentration de la température de Curie ou encore l'évolution de l'énergie de mélange et de l'ordre atomique à courte distance en fonction de la température et de la concentration en Mn.

Puisque dans ces alliages la diffusion substitutionnelle est en général régie par mécanisme lacunaire, nous proposons aussi un formalisme prenant en compte explicitement les effets de l'ordre magnétique local sur les propriétés des lacunes. Par

simulations Monte Carlo de traceurs, cette approche prédit la dépendance en température de l'auto-diffusion dans le Fe en excellent accord avec les études expérimentales. La déviation de la loi d'Arrhénius proche de la température de Curie est directement prédite, ainsi que le changement de pente entre les régimes ferromagnétique et paramagnétique. La précision du modèle de Ruch, couramment utilisé dans la littérature, est discutée au vu des résultats obtenus. Enfin, cette approche est appliquée à la diffusion d'un soluté de Mn dans le Fe pur. En utilisant d'une part la simulation Monte Carlo de traceurs et d'autre part le modèle de LeClaire, on montre que l'accélération de la diffusion autour de Tc est fortement réduite dans le cas du Mn, comparé à l'auto-diffusion du Fe. Ces résultats sont en accord avec les observations expérimentales, ce qui représente un pas en avant en comparaison des études théoriques antérieures. De manière générale, ce travail fournit de nouveaux éléments concernant les effets du magnétisme dans le fer et les alliages Fe-Mn cubiques centrés, aussi bien à l'état fondamental qu'à température finie, mettant à contribution la simulation Monte Carlo couplée à un modèle d'interactions effectives innovant prenant en compte explicitement les variables magnétiques et chimiques du système.

Abstract

In 3*d* alloys, magnetic properties of solutes can be extremely sensitive to local chemical and structural environments. Therefore, the properties of these solutes are often at the origin of discrepancies between various data from both theoretical and experimental investigations. This is for instance the case of Mn solutes in bcc iron. Also, alloys presenting a magnetic competition between solute-solute and solute-host atom interactions often exhibit complex magnetic structures. Moreover, previous studies have shown that magnetism in Fe-based alloys has a crucial impact on various thermodynamic and kinetic properties.

The objective of this work is to identify and understand the coupling between the magnetic and energetic properties of bcc Fe-Mn alloys at ground-state but also at finite temperature, and to evaluate the effects of magnetism on thermodynamic and kinetic properties.

In order to properly understand the fundamental properties of these alloys, the first part of this work is dedicated to the study of the effects of local chemical environment on the magnetic state of Mn solutes in bcc Fe-Mn by means of Density Functional Theory. Namely, configurations containing Mn solutes, being isolated or forming a cluster, and in the presence of vacancies or interstitial impurities are investigated. The lowest-energy magnetic configuration of each system is determined, and general trends are identified. Based on the obtained results, we also provide possible explanations for the existing discrepancies between theoretical and experimental studies.

The ab-initio data produced are then used to parameterize an effective interaction model in order to study the properties of Fe-Mn alloys at finite temperature. The key features of Fe-Mn alloys are identified, and the model is validated at low temperature by reproducing *ab-initio* predictions. Using this model coupled to Monte Carlo simulations, we simulate the chemical evolution of Fe-Mn properties depending on temperature and Mn concentration while relaxing the magnetic structure on-the-fly. In order to illustrate the validity and the applicability of the model, we examine certain finite temperature properties of bcc Fe-Mn alloys such as the concentration dependence of the Curie temperature or the temperature evolution of the mixing energy and the atomic short-range order.

Since diffusion in Fe and Fe-Mn alloys is frequently ruled by vacancy-mechanism, we also propose a formalism to take explicitly into account the properties of vacancies in the interaction model and the effect of local magnetic state on these properties. By performing tracer diffusion Monte Carlo simulations, this approach predicts the

temperature dependence of self-diffusion in bcc Fe in excellent agreement with experimental results. This prediction directly includes the deviation from Arrhenius law around the Curie temperature and the change of slope between the ferromagnetic and paramagnetic regimes. The accuracy of the widely used Ruch model is discussed in the light of the present results.

Finally, we apply this approach to the diffusion of a Mn solute in bcc Fe at the infinite dilution limit. Using both tracer diffusion simulations and the LeClaire model, we show that the acceleration of diffusion near T_C is highly reduced in the case of Mn compared to the self-diffusion of Fe, in good agreement with experimental observations, which is a step forward compared to the available theoretical literature.

This work provides some new insights on the effects of magnetism in bcc Fe and Fe-Mn alloys, both at ground-state via DFT calculations and at finite temperatures using Monte Carlo simulations with a newly developed effective interaction model that takes explicitly into account the magnetic and chemical variables of the system.

Acknowledgements

First of all, I would like to thank the reviewers of this thesis, Ralf Drautz and Lionel Calmels who have accepted to spend some time during the summer in order to read this manuscript. I also would like to thank the jury members Fabienne Berthier, Pavel Korzhavyi, Christian Meny and Mikhail Lavrentiev for accepting to be present at my PhD defense.

I would like to address my entire gratitude to Chu Chun Fu, for the fundamental role that she played in this journey. Our daily discussions and your brilliant advises have highly contributed to this work. Thank you for all the time you spent guiding me, for your patience and for your appetite for science, which pushed me to constantly go further and deeper into this very interesting topic.

I would also like to thank Cyrille Barreteau, the director of this thesis, for his support, his kind advises and for spending some time in the review of this manuscript.

I am also very thankful towards Frédéric Soisson, for his expertise and all the brilliant advises and ideas he provided, which highly contributed to the completion of this work.

I also thank the head of SRMP Jean-Luc Béchade for welcoming me in his service and more generally all the SRMP members for their kindness. I spent more than three years in this laboratory and I eventually felt like home there. Especially, I thank Elric Barbé for his support (when I was a DFT-rookie, some time ago) and for all the great conversations we've had, more than a colleague he became a real friend.

During my PhD, I was closely involved in the Magikid international project. I would like to thank all the members of this project, for all the fruitful discussions, and the very interesting remarks and suggestions during our meetings. Especially, I thank Tilmann Hickel and Osamu Waseda for the very interesting collaboration we had, and for their welcome during my stay at Max-Planck Institute last year in Düsseldorf.

I would also like to thank my family, for their long term support. They strongly believed in me during all these years, which without any doubt led me through this long journey.

Finally, I would like to thank my fiancee and companion of many years Pauline, who supported me during these hard-working years. The simple idea of finding her at home each evening helped a lot through the most difficult times.

Contents

List of Abbreviations

DFT	**D**ensity **F**unctional **T**heory
EIM	**E**ffective **I**nteraction **M**odel
MC	**M**onte **C**arlo
DOS	**D**ensity **O**f **S**tate
PDOS	**P**rojected **D**ensity **O**f **S**tate
FM	**F**erro**M**agnetic
AF	**A**nti**F**erromagnetic
PM	**P**ara**M**agnetic
NM	**N**on **M**agnetic
AFD	**A**nti**F**erromagnetic **D**ouble-layer
AFQ	**A**nti**F**erromagnetic **Q**uadruple-layer
NMR	**N**uclear **M**agnetic **R**esonnance
VASP	**V**ienna **A**b-**I**nitio simulation **P**ackage
NEB	**N**udged **E**lastic **B**and
BCC	**B**ody **C**entered **C**ubic
US	**U**ltra **S**oft (pseudo-potential)
NC	**N**orm **C**onserving (pseudo-potential)
PAW	**P**rojector **A**ugmented **W**ave
GGA	**G**eneralized **G**radient **A**pproximation
LDA	**L**ocal **D**ensity **A**pproximation
SQS	**S**pecial **Q**uasi-random **S**tructure
FIA	**F**oreign **I**nterstitial **A**tom
NN	**N**earest-**N**eighbor
CPA	**C**oherent **P**otential **A**pproximation

Physical Constants

Boltzmann constant	$k_B = 8.617 \times 10^{-5}\,\mathrm{J\,K^{-1}}$
Reduced Planck constant	$\hbar = 6.582 \times 10^{-16}\,\mathrm{eV\,s}$
Debye frequency (Fe)	$\nu_D = 1 \times 10^{13}\,\mathrm{Hz}$
Bohr magneton	$\mu_B = 5.788 \times 10^{-5}\,\mathrm{eV\,T^{-1}}$

To Pauline

Introduction

Many industrial applications are based on steels, as these alloys exhibit a lot of interesting properties which can be enhanced through the addition of many alloying elements (Cr, Ni, Co, Mn...etc). In fact, steels are adaptable to almost every industrial application by selecting the right composition and thermo-mechanical treatment. Manganese is a common alloying element in austenitic steels, because of its ability to trap sulfur and its deoxidization properties. Depending on its concentration, Mn may provide improved mechanical properties, act against corrosion and also increase the hot workability of steels by preventing the formation of sulphides. Also, ferritic/martensitic steels containing manganese are especially interesting as structural materials in nuclear applications due to their reduced activation properties. For instance, such alloys are used nowadays in pressurized water reactors vessels (16MND5) and considered as promising candidates for future nuclear fission and fusion technologies (EUROFER97). More recently, manganese is also involved in the emerging field of high entropy alloys (for instance Cr-Mn-Fe-Co-Ni [143]).

In the field of materials atomistic modelling, complex systems such as multi-component steels are often represented by simpler model alloys, in order to simplify the studies, to limit the computational cost, and to investigate separately on the properties of each alloying element. In this matter, a lot of research effort has been involved over the last decades in the study of binary Fe-based alloys, such as Fe-Cr, Fe-Ni, Fe-Mn... Although these alloys have been widely studied, many open questions remain concerning some crucial properties.

This work is focused on the body-centered cubic (bcc) phase of Fe-Mn model alloys. According to the existing Fe-Mn phase diagram [176], the bcc structure is the stable phase at low Mn concentration (for instance up to 5 at.% at room temperature). It was also shown that this bcc phase can be extended up to 11 at.% of Mn at room temperature with cold-rolling. [121] On the theoretical side, density functional theory (DFT) results suggest that the bcc phase is more stable than face-centered cubic (fcc) and hexagonal close-packed (hcp) phases at 0K up to approximately 13 at.% Mn [96].

Magnetic interaction between a 3*d* solute and host atoms in a ferromagnetic lattice is known to depend on the solute *d*-band filling. It tends to be anti-ferromagnetic (AF) for the early-3*d* elements and ferromagnetic (FM) for the elements with a large *d*-band filling. In between, magnetic properties of solutes with around half *d*-band filled can be extremely sensitive to local chemical and structural environment. Therefore, they are often at the origin of discrepancies between various data from both

theoretical and experimental investigations. This is for instance the case of Mn solutes in bcc iron [5] and Cr solutes in fcc nickel[16, 183]. In addition, metal alloys presenting a magnetic competition between solute-solute and solute-host atom interactions often exhibit complex magnetic structures. The interplay between local magnetic order and structural and chemical defects have been widely studied in the past few years for Fe-Cr systems [125, 122, 123, 76, 155, 88, 40, 154]. In particular, previous studies have shown that magnetism in Fe-Cr alloys has a crucial impact on various thermodynamic and kinetic properties [134, 146]. Such behaviours remain poorly understood for Fe-Mn systems, although it is known that pure bulk Mn shows a complex magneto-structural phase diagram [63, 55] and that there is a strong magneto-elastic coupling in Fe-Mn alloys [118].

The analysis of the existing experimental and theoretical literature concerning the low temperature magnetic properties of bcc Fe-Mn alloys reveals significant discrepancies. For instance, various theoretical studies (using various methodologies described in chapter 2) suggest that at low Mn concentration, Mn magnetic moments tend to couple antiparallel with Fe moments [52, 110]. Some of these studies reveal a transition around 7 at. % Mn to the opposite behavior (parallel coupling of Fe and Mn moments) [110]. From the experimental point of view, some inconsistencies exist between the two only studies at very low Mn concentration (less than 2 at. % Mn) while beyond 2 at. % Mn experiment all agree on the fact that the Fe-Mn interaction is ferromagnetic [119, 25, 132]. On the other hand, the theoretical results concerning the magnetic properties of Mn solutes in bcc Fe are known to be sensitive to approximations within DFT, such as the exchange-correlation functional, for instance.

More generally, the simulation of magnetism effects on the thermodynamic and kinetic properties of Fe alloys at finite temperature remains a challenge, which leads to a limited predictability of the materials properties at application temperatures. Previously, various studies with distinct approaches have attempted to provide a proper description of magnetic alloys at finite temperature.

A major contribution in this field has been made using the disordered local moment (DLM) approach [2, 3, 135], mostly combined with either Coherent Potential Approximation (CPA) calculations or a supercell approach. These studies attempt to describe ideally paramagnetic alloys by ensuring a negligible correlation between the spins. Although a lot of valuable information has been obtained adopting this approach, its main limitation is that it neglects in principle the magnetic short-range order. Thus, the DLM approach does not allow to directly study the intermediary temperature range, especially the domain around the Curie transition which is critical for these materials. It is however possible to interpolate such properties using empirical approaches such as the Ruch model [137], which validity is discussed in this thesis.

Another more recent approach allowing to study the finite temperature magnetic

properties of alloys is the spin-lattice dynamics [179, 173, 174]. One of the major advantages of this approach is to take intrinsically into account the coupling between lattice and magnetic excitations. However, the use of empirical interatomic potentials (e.g. EAM type), which are generally not trivial to parameterize for alloys. Finally, the computational cost of this approach prevents it (for now) from be applied to larger size and time scales, compared to Monte Carlo simulations.

Over the last decades another formalism was developed, with for instance contributions of Pierron-Bonhes *et al.* [130], Lavrentiev *et al.* [87], Ruban *et al.* [135]. It consists in using an effective interaction model which takes explicitly into account the magnetic and chemical variables of the system. This approach allowed to predict, for instance, the evolution of Curie temperature as a function of Cr concentration in Fe-Cr alloys. However, this formalism has never been applied to the study of structural defects, which is essential to understand many materials properties. Also, this kind of approach was used to predict the magnetic state of given atomic structures, but the combined evolution of the magnetic and the atomic structures (eventually correlated) has not really been simulated.

Before the beginning of this work, there are significant inconsistencies in the literature concerning the magnetic properties of Mn in bcc Fe-Mn alloys at the ground-state. Also, no theoretical study so far has undertaken the description of Fe-Mn alloys at finite temperature. It is therefore interesting to have a deeper understanding of this system. For instance, recent experimental works (unpublished data kindly provided by S. Divinski) carefully confirmed that Mn diffusion coefficient in bcc Fe does not show any deviation from the Arrhenius law, which is atypical as all other substitutional solutes diffusion in bcc Fe shows a significant acceleration near the Curie temperature.

This is what justifies this study. It consists in understanding the interplay between the chemical structure and the magnetic order in Fe-Mn alloys via first principles and developing an approach which allows to study the effects of magnetism on thermodynamic and diffusion properties, at finite temperature.

The key points of methodology are described in chapter 1.

In chapter 2, our purpose is to identify the effects of local chemical environment on the magnetic state of Mn solutes in bcc Fe-Mn. To do so, we study by means of Density Functional Theory, the dependence of Mn magnetism in various local environments in bcc Fe-Mn alloys. Namely, configurations containing Mn solutes, being isolated or forming a cluster, and in the presence of vacancies or interstitial impurities are investigated. The dependence of Mn magnetic state on the alloy concentration and the chemical short-range order is determined and discussed. Based on the obtained results, we also provide plausible explanations for the existing discrepancies between theoretical and experimental studies.

The ab-initio data produced in this work are then used in chapter 3 to parameterize an effective interaction model in order to study the properties of Fe-Mn alloys at finite temperature. To do so, the key features of Fe-Mn alloys are identified, and the

parameters are fitted on ab-initio data. The model is validated at low temperature by reproducing ab-initio predictions via spin Monte Carlo simulations (at 1K). Using this model coupled with atomic and spin Monte Carlo simulations, we simulate the evolution of Fe-Mn systems depending on temperature and Mn concentration. To do so, we developed a simulation code to combine an atomic exchange Monte Carlo algorithm with a Spin relaxation Monte Carlo algorithm on-the-fly. This code is used in order to simulate the unmixing behaviour with the corresponding spin relaxation of the Fe-Mn solid solutions at various temperatures and concentrations.

These simulations allow to describe the equilibrium state of the system, but the prediction of the kinetic properties is also of main interest. Since diffusion in Fe-based alloys is frequently ruled by vacancy-mechanism, we propose in chapter 4 a formalism to take explicitly into account the properties of vacancies in the interaction model and the effect of local magnetic configurations around the vacancy on these properties. To do so, we extend the model to take into account the formation and migration energies of a vacancy, in various magnetic environments. We perform tracer diffusion simulations via Monte Carlo in order to validate the approach by comparing the obtained temperature dependence of the self-diffusion coefficient in pure Fe to the available experimental data. In the light of the obtained results, we evaluate the validity of the widely used Ruch model. We also investigate on the importance of considering quantum effects when simulating diffusion properties. Finally, we study the diffusion of a Mn solute in bcc Fe at infinite dilution limit, in order to investigate on the absence of deviation from the Arrhenius law near the Curie temperature, contrary to most other solutes in bcc Fe.

Chapter 1

Methods

In this chapter are presented the main tools applied in the studies within this thesis. The theoretical fundamentals of both ab-initio calculations and Monte Carlo simulations are presented, along with the description of specific methodologies used throughout this work. Many physical expressions are also explicited in order to avoid any ambiguity in the following chapters.

Computational materials modeling is a discipline which aims at describing and predicting as accurately as possible key properties of specific materials, using more or less empirical numerical tools. It has become a major field of materials research and development efforts and it keeps progressing along with the never-ending increase of computational power.

Given that the field of application of each method is generally limited to certain size and time scales, it is in principle of great interest to combine several complementary approaches. In this thesis, electronic structure calculations are performed in order to identify the key energetic and magnetic properties of various systems. However, due to the intrinsic limitations of ab-initio methods, the obtained data are used to parameterize an effective interaction model in order to study the finite temperature properties of alloys with defects using Monte Carlo simulations.

This chapter aims at introducing the tools and gathering the technical features applied in the studies within this thesis.

1.1 Density functional theory calculations

1.1.1 Principle

Almost a century ago, in the premises of quantum mechanics, Erwin Schrödinger [144] discovered that understanding the behavior of a quantum particle requires to determine its wavefunction $\psi(\mathbf{r})$ for every point $\mathbf{r}$ in space, which can be achieved by solving his eponymous equation. For the case of stationary electronic states of a system, this equation is reduced to the time-independent Schrödinger equation:

$$[\widehat{T}_e + \widehat{T}_N + \widehat{V}_{ee} + \widehat{V}_{NN} + \widehat{V}_{eN}]\psi = E\psi \tag{1.1}$$

where $\widehat{T}_e$ and $\widehat{T}_N$ respectively represent the kinetic energy of electrons and nuclei, and where $\widehat{V}_{ee}$, $\widehat{V}_{NN}$ and $\widehat{V}_{eN}$ respectively denote the electron-electron, nuclei-nuclei, electron-nuclei interaction potentials. E is the energy eigenvalue of the stationary state described by the wavefunction ψ.

Finding the lowest energy eigenstate - the ground-state - of this equation for a given system allows to deduce many key properties of this system. Unfortunately, except for extremely simple systems, this many-body Schrödinger equation is practically unsolvable. Throughout the years, many approximations have been developed to make such problems solvable.

First of all, the Born-Oppenheimer approximation [19] consists in considering the nuclei immobile as these are extremely heavier and slower than electrons. It helps to reduce the complexity of the equation by suppressing the kinetic term of nuclei $\widehat{T}_N$, and making the nuclei-nuclei interaction term $\widehat{V}_{NN}$ a constant.

In 1964, P. Hohenberg and W. Kohn published the first pillar of Density functional theory [64]. What is now called the Hohenberg-Kohn theorem showed that since the energy E of any state is a functional of the many-body wavefunction ψ (3N variables), then the energy of the ground-state is a functional of the electron density n(**r**), only depending on 3 variables. Despite being a leap forward, this theorem does not give any clue on how to build such functional.

Kohn and Sham proposed in 1965 [79] to decompose the total energy into the known energy contribution of the independent electron (including kinetic, potential and Hartree energies) and another term E_{xc} called the exchange and correlation energy, which value is unknown. The Kohn-Sham energy E_{KS} is expressed as:

$$E_{KS} = T_s[n] + \int d\mathbf{r} V_{ext}(\mathbf{r}) n(\mathbf{r}) + E_{Hartree}[n] + E_{NN} + E_{xc}[n] \tag{1.2}$$

T_s being the kinetic energy of the independent electron, V_{ext} is the potential induced by nuclei or any other external source and E_{NN} is the constant nuclei-nuclei interaction energy. $E_{Hartree}$ arises from the interaction between electronic densities in two points of space **r** and **r'**, according to the following expression:

$$E_{Hartree}[n] = \frac{1}{2} \int d^3r d^3r' \frac{n(r)n(r')}{|r - r'|} \tag{1.3}$$

Finally, the exchange-correlation energy E_{xc}, which contains both the correction of T_s and $E_{Hartree}$ is expressed as:

$$E_{xc}[n] = \langle \widehat{T}_e \rangle - T_s[n] \langle \widehat{V_{ee}} \rangle - E_{Hartree}[n] \tag{1.4}$$

The point of DFT calculations is to determine the Kohn-Sham energy through a self-consistent process. It consists in generating a first electronic density, for instance as a linear combination of corresponding isolated atoms. The eigenvalues, eigenstates and E_{KS} are calculated for this state and the density is then updated, and so

on until the convergence is reached, which leads to the electronic ground-state of the system.

Among other properties, DFT allows to calculate the forces and stresses of each electronic ground-state associated to a given atomic configuration, using the Hellmann-Feynman theorem. The forces and stresses obtained may then be used to optimize the atomic configuration of a system, or to perform molecular dynamics simulations, for instance.

As the exchange and correlation energy E_{xc} is unknown, it must be approached with a density functional. The simplest and most commonly used functional is called the *Local Density Approximation* (LDA), which only depends on the electronic density at each point of the space, as shown in the following expression:

$$E_{xc}^{LDA}[n] = \int n(\mathbf{r})\epsilon_{xc}[n]d\mathbf{r} \tag{1.5}$$

Despite being very useful in many contexts, it presents major contraindications for the study of iron based alloys, as it is not able to predict the correct ground-state of pure Fe. Using LDA, DFT calculations do not predict ferromagnetic body-centered cubic phase to be the ground-state, in disagreement with experiments [171]. Another very common functional is the *Generalized gradient approximation*, which not only depends on local electronic density, but also on the gradient of this density, as shown in the following expression:

$$E_{xc}^{GGA}[n] = \int n(\mathbf{r})\epsilon_{xc}[n, \nabla n]d\mathbf{r} \tag{1.6}$$

The GGA exchange-correlation functional is much more robust for the study of iron based alloys [56].

In order to drastically improve the computional cost of DFT calculation, it is common to use *pseudo-potentials*. Contrary to valence electrons, core electrons have a minor effect on chemical bonds and thus materials properties, while the wavefunctions near the nuclei show very sharp oscillations leading to high computational costs. It seems then reasonable not to treat these core electrons explicitely. Several approaches are commonly used: norm-conserving (NC) pseudo-potentials , ultra-soft (US) pseudo-potentials and finally the projector augmented wave method (PAW). NC and US pseudo-potentials are parameterized following the same general idea: core electrons are represented by smoother potentials and wavefunctions, while it is not the case for PAW. NC and US pseudo wavefunctions and all-electrons wavefunctions are identical beyond a defined cut-off radius. Inside the cut-off sphere however, in the case of NC pseudo-potentials, eigenvalues and charge are identical between pseudo-potential and all-electrons calculations. In the case of US pseudo-poentials, the charge equality condition is not verified, which allows faster calculations. The main drawback of these pseudo-potentials is that most information concerning the wavefunction near the nuclei is lost, which may affect some properties such as magnetism. As shown in a previous study [124], distinct pseudo-potentials may lead to

dramatically different magnetic ground-states of Mn in bcc Fe. The PAW approach is a bit different from NC and US pseudo-potentials: beyond the cut-off radius, the all-electrons wavefunction is used, while inside the cut-off sphere, the wavefunction is defined as a linear transformation of the all-electron wavefunction (frozen core approximation). The major advantage of PAW is the possibility to re-build the all-electrons wavefunction which makes it more robust than pseudo-potentials while being much more computationally efficient than all-electrons calculations.

Wavefunctions are represented using basis functions. Usually, we either use localized basis (for instance gaussians or pseudo-atomic orbitals) as in the SIESTA code [153], or plane-waves basis as in PWscf [45, 46] or the VASP code [82, 80, 81]. In this study, the latter form is used.

1.1.2 Computational details

In this work, Density Functional Theory calculations are performed with the Projector Augmented Wave (PAW) method [15, 83] as implemented in the VASP (Vienna Ab-initio Simulation Package) code[82, 80, 81]. The results presented are obtained using the generalized gradient approximation (GGA) for the exchange-correlation functional in the Perdew-Burke-Ernzerhof (PBE) form [129] (if not explicitly indicated). All the calculations are spin-polarized. $3d$ and $4s$ electrons are considered as valence electrons. The plane-wave basis cutoff is set to 400 eV. Electronic projected densities of states (PDOS) and atomic magnetic moments are obtained by a projection scheme based on the PAW method as implemented in the VASP code. If using the projection on spheres around atoms as a criterion, we checked that a 10% variation of the sphere radius from half the $1nn$ interatomic distance induces at most a 1% change of the local magnetic moments. The projection operators are evaluated in the reciprocal-space.

Please note that only spin moments are considered while orbital moments are neglected. Indeed, we know from litterature that the orbital moment in Fe bulk systems is very small compared to the total magnetic moment (less than 5% [22]). Concerning Mn, such results are not available in the literature for the bcc bulk but very small values of the orbital moment are reported in various stuctures, suggesting that this approximation is reasonable. [37, 42]). Some ab-initio results of this thesis are obtained using non-collinear magnetism calculations, in which spin-orbit coupling is not considered.

Supercell calculations are performed to simulate Mn solutes in bcc ferromagnetic Fe with and without a vacancy or impurities. Clusters containing up to 15 Mn atoms were simulated using cubic supercells of $4 \times 4 \times 4$, $5 \times 5 \times 5$ and $6 \times 6 \times 6$ times the lattice parameter of the cubic unit cell (a_0), containing respectively 128, 250 and 432 atom sites. The solid solutions were represented by Special Quasirandom Structures (SQS)[184] in cubic supercells of $3 \times 3 \times 3$ and $4 \times 4 \times 4$ times a_0, containing respectively 54 and 128 sites. All the calculations were performed at constant volume. For

the SQS systems, the lattice parameters of such systems were set according to Vegard's law. The residual stresses of every studied system were checked to remain lower than 10 kbar.

The $k-$point grids used in our calculations were adjusted according to the size of the supercell. They were chosen to achieve a k-sampling equivalent to a bcc cubic unit cell with a $16 \times 16 \times 16$ shifted grid, following the Monkhorst-Pack Scheme.[112] The Methfessel-Paxton broadening scheme with 0.1 eV width was used.[109] The convergence threshold for the electronic self-consistency loop was set to $\Delta E = 10^{-6}$ eV and atomic relaxations at constant volume were performed down to a maximum residual force of 0.02 eV/Å. We have verified that the magnetic structures and cluster formation energies are well converged with respect to the choice of $k-$point grids and the cutoff conditions. The resulting error bars for energy differences and magnetic moments of Fe and Mn are respectively 0.02 eV, 0.01 μ_B and 0.1 μ_B. These are mainly associated to the convergence of the plane-wave energy cutoff and the $k-$grid density.

All the alloy concentrations given in the thesis are expressed as atomic percent, if not explicitly otherwise indicated.

1.1.3 Method validation on pure Fe and pure Mn

The described computational method was used to calculate the relevant crystallographic and magnetic structures of pure Fe and Mn bulks. The results were then compared with existing literature data in order to validate our approach and to give additional insights into the magnetic structures of bulk Mn. All these results are obtained with collinear magnetism calculations.

Pure iron is widely known to have a ferromagnetic body-centered cubic ground state. It is correctly predicted by our calculations which lead to a magnetic moment of 2.20 μ_B per atom, at the optimal lattice parameter which is found to be 2.832 Å. Elementary properties for other states are also in excellent agreement with previous results [60, 120, 115, 70]. A detailed comparison is summarized in Table 1.1.

Pure manganese is known under various allotropic forms with distinct magnetic orderings. The lowest energy and most common structure, shown in Fig. 1.1 is called α-Mn. Its 58-atom cubic unit cell contains four sub-lattices, each one showing (with collinear magnetism) an anti-ferromagnetic ordering, eventhough the actual lowest energy state was predicted to exhibit a non-collinear behavior, almost degenerate with the collinear AF order.[63] β-Mn is the second most stable cristallographic structure, found at higher temperatures, with 20 atoms per cubic unit cell forming two sublattices, as shown in Fig. 1.1. The magnetic structure of β-Mn is ferrimagnetic (FiM): each sub-lattice has a ferromagnetic order, opposed to each other with distinct magnitudes.[55] γ-Mn shows a face-centered cubic cell which magnetic order is anti-ferromagnetic.[55] And finally, we predict the body-centered cubic δ-Mn to have a double-layer anti-ferromagnetic (AFD) ground state, at variance with the

Phase	Mag.	ΔE (eV)	a_0 (Å)	$\mu_{Fe}(\mu_B)$
bcc	FM	0 (GS) (0.00)[60] (0.00)[70]	2.832 (2.843)[60] (2.83)[70]	2.20 (2.17)[60] (2.20)[70]
bcc	AFD	0.178	2.841	2.18
bcc	AF	0.442 (0.44)[60] (0.44)[70]	2.793 (2.803)[60] (2.79)[70]	1.29 (1.25)[60] (1.22)[70]
bcc	NM	0.475 (0.47)[60] (0.46)[70]	2.757 (2.771)[60] (2.76)[70]	0.00 (0.00)[60] (0.00)[70]
fcc	AFD	0.104 (0.10)[60] (0.10)[70]	3.544 (3.538)[60] (3.52)[70]	1.93 (1.80)[60] (1.79)[70]
fcc	AF	0.124 (0.10)[60] (0.11)[70]	3.486 (3.503)[60] (3.48)[70]	1.27 (1.30)[60] (1.23)[70]
fcc	FM(hs)	0.154 (0.15)[60] (0.16)[70]	3.625 (3.643)[60] (3.64)[70]	2.57 (2.57)[60] (2.62)[70]
fcc	FM(ls)	0.155 (0.13)[60] (0.14)[70]	3.480 (3.495)[60] (3.47)[70]	1.03 (1.02)[60] (0.94)[70]
fcc	NM	0.163 (0.15)[60] (0.14)[70]	3.446 (3.464)[60] (3.45)[70]	0.00 (0.00)[60] (0.00)[70]

TABLE 1.1: Fe bulk elementary properties for each phase. ΔE stands for the energy difference between the considered phase and the ground state (GS) (bcc FM Fe), a_0 is the optimized lattice parameter and μ_{Fe} is the magnetic moment per atom. Values between parenthesis were obtained by Herper et al.[60] using full potential linear augmented plane-wave method within the GGA approximation and by Jiang et al[70] using the PAW method within the GGA approximation. Please note that some reference values are deduced from figures if the precise numbers are not given in Refs. [60, 70].

Phase	Mag.	ΔE	a_0(Å)	$\mu_{Mn}(\mu_B)$
α	AF	0 (GS) (0)[63]	8.599 (8.668)[63]	2.9/2.2/0.5/0.1 (2.8/2.2/1.0/0.0)[63]
α	NM	0.024 (0.04)[63]	8.538 (8.532)[63]	0.00 (0.00)[63]
β	FiM	0.074 (0.063)[63]	6.005 (6.007)[63]	0.5/0.1 (0.3/0.0)[63]
β	NM	0.075 -	6.003 (6.007)[63]	0.00 (0.00)[63]
bcc	AFD	0.128	2.850	1.89
bcc	c(2x2)	0.145 (0.146)[55]	2.815 (2.81)[55]	1.49 (1.35)[55]
bcc	FM	0.170 (0.17)[55]	2.790 (2.80)[55]	0.85 (0.9)[55]
bcc	NM	0.188 (0.19)[55]	2.777 (2.77)[55]	0.00 (0.00)[55]
bcc	AF	0.251	2.800	2.45
fcc	AF	0.068 (0.067)[55]	3.572 (3.55)[55]	1.84 (1.60)[55]
fcc	NM	0.106 (0.11)[55]	3.495 (3.51)[55]	0.00 (0.00)[55]

TABLE 1.2: Mn bulk elementary properties for each phase. ΔE stands for the energy difference between the considered phase and the ground state (GS) (AFM α-Mn), a_0 is the optimized lattice parameter and μ_{Mn} is the magnetic moment per atom. Values between parenthesis were obtained by Hobbs et al.[63] and Hafner et al.[55] using the PAW method within the GGA approximation. Please note that some reference values are deduced from figures if the precise numbers are not given in Refs. [63, 55].

prediction from an earlier DFT study[55] of a c(2x2) in-plane anti-ferromagnetic ordering. From our results, the AFD magnetic state presents a magnetic moment of 1.89 μ_B per atom at its optimal lattice parameter of 2.850 Å, and the previously described c(2x2) in-plane anti-ferromagnetic state is 0.02 eV per atom more energetic at its own optimal lattice parameter (2.815 Å). The magnetic moment in this case is found to be 1.49 μ_B. Since both these magnetic orders tend to induce tetragonal deformation to the lattice, we have checked that the AFD state remains lower in energy than the c(2x2) state with full shape and volume relaxations of the simulation cells (ΔE = 0.01 eV). Please note that the energy difference found between AFD and c(2x2) magnetic states is comparable to the energy uncertainty of our calculations. These magnetic states may then be considered degenerate. For consistency, we consider in the rest of the thesis the lowest-energy magnetic state of bcc Mn to be AFD. The calculated lattice parameters, relative energies and magnetic moments for all the considered phases, together with the comparison with previous data are shown in Table 1.2. All our results are in excellent agreement with previous DFT data findings[63, 55], the only exception being the lowest energy AFD state of the δ-Mn phase for which no data was found in the literature.

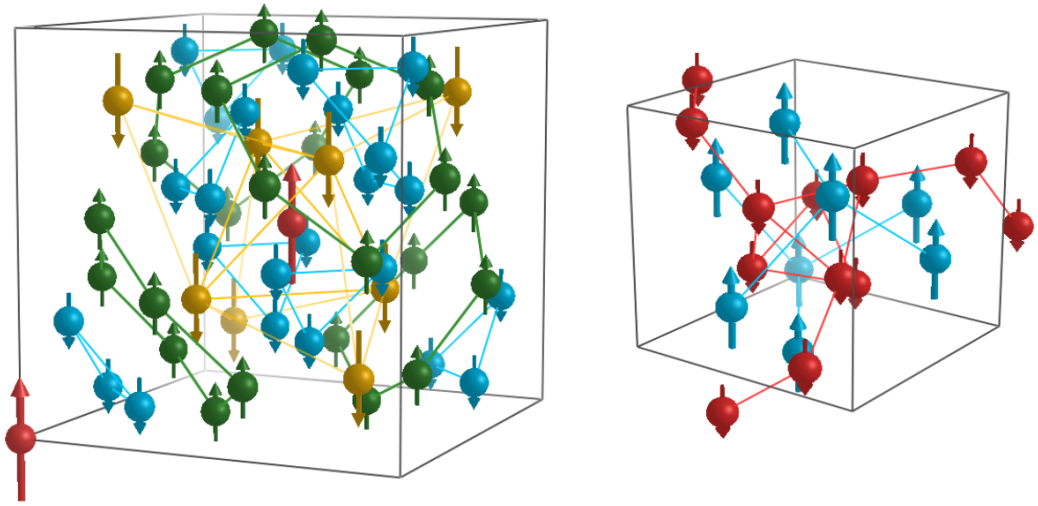

FIGURE 1.1: Visual representation of (a) the α-Mn unit-cell, at collinear magnetic ground-state with four sub-lattices and (b) the β-Mn unit-cell at Ferrimagnetic ground-state. Different colors denote the distinct sub-lattices.

1.1.4 Constrained local magnetism within the collinear approximation

In the attempt of exploring an energetic landscape or generating data for parameters fitting, the ability to constrain some magnetic moments to a particular direction or even a particular magnitude may be required. To do so, the VASP code natively offers the possibility to constrain the local magnetic moment on each atom. It consists

in specifying along with the initial magnetic moments, the list of "target" magnetic moments. A penalty energy is then added to the total energy of the system.

If only the direction of the magnetic moments is to be constrained, according to Ma *et al.* the penalty energy has the following expression [101]:

$$E_P = \sum_i \lambda(|\overrightarrow{M_i}| - \overrightarrow{e_i} \cdot \overrightarrow{M_i})^2 \tag{1.7}$$

where $\overrightarrow{M_i}$ is the magnetic moment of the $i-$th atom and where $\overrightarrow{e_i}$ is the unit vector of the target direction of the $i-$th atom magnetic moment.

If both the direction and the magnitude of the magnetic moments are to be constrained, the penalty energy has the following expression:

$$E_P = \sum_i \lambda(\overrightarrow{M_i} - \overrightarrow{M_i^0})^2 \tag{1.8}$$

where $\overrightarrow{M_i}$ is the magnetic moment of the i-th atom and where $\overrightarrow{M_i^0}$ is the target magnetic moment of the i-th atom.

Note that the λ parameter is to be set by the user. A small value of λ leads to a softer constraint while a high value of λ leads to a more strict constraint, but may have a significant impact on self-consistency convergence. Each constrained local moment calculation was performed incrementing the λ constraint parameter up to the obtaining of a satisfactory low penalty energy term (less than one hundredth of the considered energy differences).

Although the VASP code natively includes this feature, some slight homemade modifications were performed on the concerned subroutine in order to make it more convenient:

- An option that allows us to constrain the magnetic moment of a selected set of atoms only.
- In the VASP code, this magnetic constraint feature is only available when considering non-collinear magnetic moments. In our study, it is also very convenient to constrain local magnetic moments of atoms within the collinear approximation as the non-collinearity induces high computational costs. Thus the analogous feature was implemented in the case of collinear magnetism approximation.

1.1.5 Vacancy formation and migration properties

In order to study diffusion properties via Monte Carlo simulation, it is necessary to parameterize the interaction model with vacancy ground-state properties predicted from DFT calculations. To do so, vacancy formation enthalpy is calculated for various magnetic configurations (see chapter 4) using the following expression:

$$E_{vac}^f = E^{tot}((n-1)\mathrm{Fe} + V) - \frac{n-1}{n} E^{tot}(n\mathrm{Fe}) \tag{1.9}$$

where $E^{tot}((n-1)\text{Fe}+V)$ and $E^{tot}(n\text{Fe})$ are respectively the total energy of the Fe system with and without a vacancy. Since the equilibrium unit-cell volume and atomic positions depend on magnetic state, the influence of considering or not these variations is discussed in chapter 4.

Ab-initio calculations are also used in order to find the saddle-point energy of vacancy migrations. These saddle-points configurations are computed using the Nudged Elastic Band (NEB) method, as implemented in the VASP code. It consists in generating several images all along the reaction path (by linear interpolation from the initial and final configurations). Atomic forces are minimized in the hyperplane of the reaction path and tangential forces between the images, arising from spring constants between these images, are also minimized. The NEB method allows to obtain the minimum energy path, given the initial and the final states of the migration.

In order to be sure to sample the saddle-point among the images, the climbing-NEB option is also used, as implemented in the VASP code. It allows the highest energy image to be freed from spring constants with the other images. Instead, this image tries to maximize its energy along the reaction path, which drives it to the migration saddle-point.

As shown in Fig. 1.2, we consider as migration enthalpy (also referred as barrier energy) the energy difference between the migration saddle-point and the initial stable configuration.

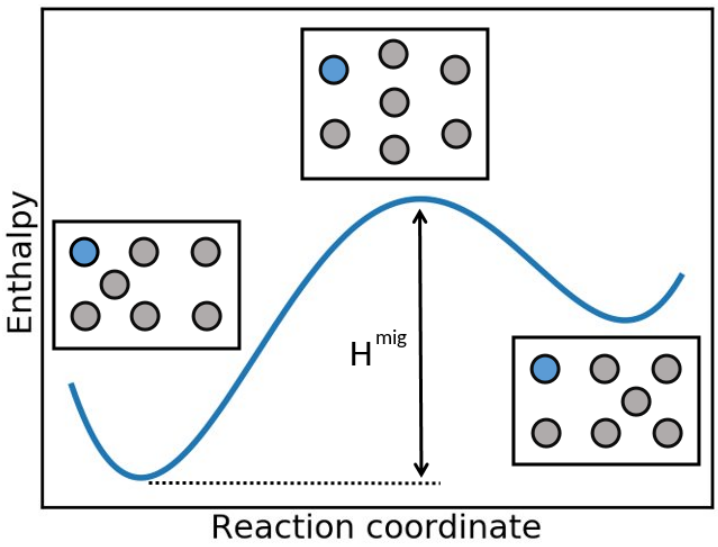

FIGURE 1.2: Schematic representation of the vacancy migration enthalpy as calculated from DFT

1.1.6 Solute diffusion

When considering diffusion in alloys, the presence of a solute is expected to have an effect on the surrounding migration barriers. The formalism of LeClaire [92] allows to estimate the isolated solute diffusion by calculating various jump frequencies in

the neighborhood of the solute atom. Especially, if the interaction between the solute and a vacancy can be considered negligible from the $3nn$ distance (the validity of this hypothesis is discussed in chapter 4), then a 10 frequencies model as shown in Fig. 1.3 is adequate.

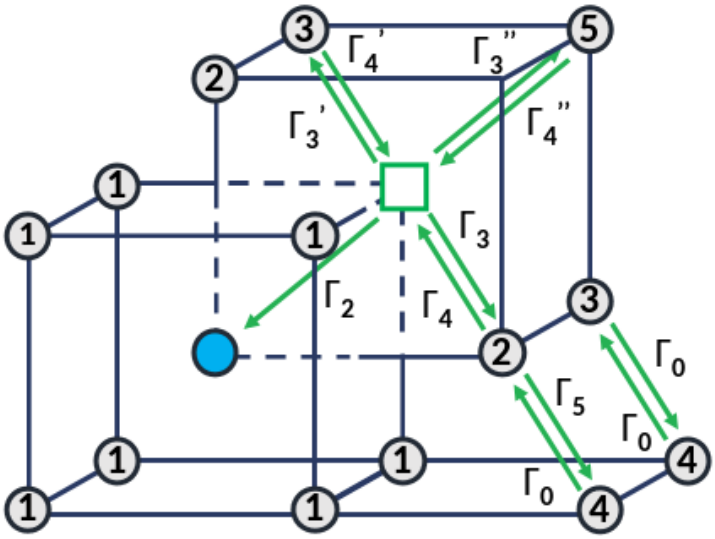

FIGURE 1.3: Schematic representation of the ten jump frequencies necessary to calculate the solute diffusion following the model of LeClaire [92].

All the migration barriers are obtained using the NEB method, as described in Section 4.1. The diffusion coefficient of the B solute in the A matrix (if the diffusion is only driven by monovacancy jump mechanism) is given by the following analytical expression [92]:

$$D^A_{B*} = a^2 C^A_v \frac{\Gamma'_4}{\Gamma'_3} f_2 \Gamma_2 \tag{1.10}$$

where Γ_i are the jump frequencies identified in Fig. 1.3. It is obtained from the migration enthalpy with the following expression:

$$\Gamma_i = \nu \exp\left(\frac{-\Delta H^{mig}_i}{k_B T}\right) \tag{1.11}$$

with ν the attempt frequency and H^{mig}_i the migration enthalpy of the i-th jump as identified in Fig. 1.3.

In equation 1.10, C^A_v is the equilibrium vacancy concentration in pure A and f_2 is the solute diffusion correlation factor, expressed as:

$$f_2 = \frac{1 + t_1}{1 - t_1} \tag{1.12}$$

where t_1 is expressed as a function of jump frequencies as indicated in Fig. 1.3.

$$t_1 = -\frac{\Gamma_2}{\Gamma_2 + 3\Gamma_3 + 3\Gamma_3' + \Gamma_3'' - \frac{\Gamma_3\Gamma_4}{\Gamma_4 + F\Gamma_5} - \frac{2\Gamma_3'\Gamma_4'}{\Gamma_4' + 3F\Gamma_0} - \frac{\Gamma_3''\Gamma_4''}{\Gamma_4'' + 7F\Gamma_0}} \tag{1.13}$$

where Γ_i are the distinct jump frequencies identified in Fig. 1.3 and F is a structure-dependent parameter, its value is 0.512 in the bcc structure [92]. However, this analytical model is only valid in magnetically ordered systems, as only a countable number of barriers need to be calculated. In magnetically disordered systems, Monte Carlo simulations are required to determine the solute diffusion coefficient.

1.1.7 Frozen phonons method

In chapter 4, the determination of diffusion coefficients requires to determine some thermal properties such as vacancy formation vibrational entropy and the attempt frequency for atomic jumps. An approximated value of these vibrational properties can be obtain via DFT calculations using the *frozen phonons* methodology [24, 177]. Phonons are quasi-particles representing the quantization of vibration normal modes of oscillating atoms in a crystal. In practice, the frozen phonons method consists in slightly displacing one atom of a supercell, and calculating the forces induced by this displacement, using the Hellmann-Feynman theorem. This procedure performed on all the atoms, in the three spatial directions, allows to build the force constants matrix and the dynamical matrix, which lead to the vibration normal modes of the system. Note that the symmetries of the system may help to drastically reduce the number of required displacements. Also, for more accurate calculations, we perform two distinct displacements for each direction. Please note that VASP only allows to calculate the phonons using the Γ point. We used the Phonopy software [160] in order to consider more $q-$points, which allows to reach convergence with a smaller supercell.

The vibrational entropy can finally be determined from the calculated phonons frequencies using the following expression[41]:

$$S_{vib} = k_B \sum_{i}^{3N} \left[-\ln(1 - e^{-\beta\epsilon_i}) + \frac{\beta\epsilon_i}{e^{\beta\epsilon_i} - 1} \right] \tag{1.14}$$

where $\epsilon_i = \hbar\omega_i$ is the phonon energy (ω_i the phonon frequency and $\hbar$ the reduced Planck constant), and where $\beta = (k_B T)^{-1}$ (k_B the Boltzmann constant, T the temperature).

From Vineyard transition-state theory, the jump frequencies can be expressed as follows[164, 58]:

$$\Gamma = \left[\prod_{i=1}^{3N-3} \nu_i^{vac} \Big/ \prod_{i=1}^{3N-4} \nu_i^{sad} \right] \cdot e^{-\beta \Delta H_v^{mig}} \tag{1.15}$$

where ν_i^{vac} is the i-th normal mode of the system containing a vacancy, ν_i^{sad} is the i-th normal mode of the system with a migrating atom at saddle-point and H_v^{mig} is the migration enthalpy through the considered saddle-point, defined in this work as the energy difference between the system with the atom at saddle point and the system containing a vacancy in the stable configuration (see section 4.1). Please note that the imaginary mode of the saddle point is not considered here, hence the 3N-4 superior limit of the saddle-point product, as opposed to 3N-3 in the stable site product (the three modes corresponding to the global translation of the system are also excluded in both cases).

1.2 Monte Carlo simulations

1.2.1 Principle

Monte Carlo simulation is a family of numerical methods based on the stochastic evolution of a given system, widely used in many contexts. The overall principle consists in attributing a success probability to each event and accept or not said event based on the generation of a random number. In this work, the system is a population of atoms, arranged on a rigid lattice. To each atom is associated a magnetic moment, defined as a vector M = (r,θ,ϕ) , and a chemical species. The general purpose of Monte Carlo simulations in this context is to explore the phase-space in order to find the equilibrium state of both the atomic and the magnetic structures of the system.

1.2.2 Algorithms

This exploration may be performed using several algorithms, among which two were used in this work: the *Metropolis Algorithm* (MA) and the *Residence Time Algorithm* (RTA). [86]

In the Metropolis algorithm, the energetic cost of a random transition is evaluated and translated to a probability of realizing this transition. A Monte Carlo step is executed as follows:

- The current system energy is calculated
- A random transition is performed
- The energy difference $\delta E = E_f - E_i$ is calculated
- The transition is accepted if $\begin{cases} \delta E < 0 \\ \delta E > 0 \text{ and } \exp(\frac{-\delta E}{k_B T}) < r,\ r \in]0,1[\end{cases}$
- If the transition is refused, the system is brought back to the initial state

If using the residence time algorithm, the energetic cost of every possible transitions is calculated, in order to associate probabilities to these transitions. The generation of a random number finally decides which transition will be executed. A Monte Carlo step is done as follows:

- The current system energy is calculated
- For each possible transition, the energy difference $\delta E = E_f - E_i$ is calculated
- Each transition energy is expressed in term of a jump frequency, analogous to a probability of happening
- A random number selects the transition to perform

In both algorithms, these steps are performed in loops as many times as needed to reach the equilibrium state. The advantage of RTA is that a transition is performed at each MC step, contrary to the Metropolis algorithm. For instance, in the case of low temperature vacancy migration, Metropolis algorithm may not be usable in practice as vacancy jumps are extremely rare events.

1.2.3 Effective interaction models

In this study, magnetic and non-magnetic interactions are explicitly treated as two distinct contributions in order to independently perform Monte Carlo simulations on the magnetic state (spin relaxations) or the chemical state (atomic pair-exchanges) of the system. In this section, the Hamiltonians for the magnetic and the non-magnetic interactions are presented separately, along with the Monte Carlo methodology for the relaxation of each degree of freedom (spin relaxations and atomic exchanges). Please note that the approximation of atomic spins is assumed in this study.

Concerning the magnetic contribution of the Hamiltonian, three distinct formalisms are generally considered [87, 130, 135], being from the simplest to the most accurate: Ising, Heisenberg and Generalized-Heisenberg models.

Without any external field, these models express the magnetic interactions energy of a N-atoms system as follows:

$$H_I = \sum_{i}^{N} \sum_{n}^{P} \sum_{j}^{Z} J_{ij}^{(n)} \mathbf{M}_i \cdot \mathbf{M}_j \tag{1.16}$$

$$H_H = \sum_{i}^{N} \sum_{n}^{P} \sum_{j}^{Z} J_{ij}^{(n)} \mathbf{M}_i \cdot \mathbf{M}_j \tag{1.17}$$

$$H_G = \sum_{i}^{N} A_i \mathbf{M}_i^2 + B_i \mathbf{M}_i^4 + \sum_{i}^{N} \sum_{n}^{P} \sum_{j}^{Z} J_{ij}^{(n)} \mathbf{M}_i \cdot \mathbf{M}_j \tag{1.18}$$

where N is the number of atoms in the system, n is the range of interactions in terms of neighbor shells (the largest interaction range considered being P), Z is the

number of neighbors of each interaction range and $\mathbf{M}_i$ is the magnetic moment of the i*th* atom. $J_{ij}^{(n)}$ represent the magnetic pair-interaction between species of atoms i and j, at range n. In the case of the Ising model, magnetic moments are considered collinear and are only allowed to have a $+\mu$ or $-\mu$ magnitude. Concerning the Heisenberg model, the magnitude of the magnetic moment is constrained to a constant value while the angle of the magnetic moment is free to have any value. Finally, the Generalized-Heisenberg model allows spin longitudinal fluctuations. A_i and B_i parameters characterize the on-site magnetism and allow to bound the variation of the magnetic moment magnitude (which otherwise would diverge in Monte Carlo simulations). [148, 87, 135] It is essential in some systems to consider these longitudinal fluctuations. For instance, when a vacancy is inserted in pure Fe, the magnitudes of the surrounding spins are significantly changed (see chapter 4). Also, in Fe-Mn bcc alloys, the magnetic moments of Mn atoms have very variable magnitudes (see chapter 2).

The evolution of the magnetic state of the system is performed using the Metropolis algorithm, defined in Section 1.2.2. The spin transition depends on the considered magnetic model. In the case of an Ising model, the concerned transition is a spin flip, from spin-up to spin-down or reverse. In the case of a Heisenberg model, the transition is the random selection of a new spin, conserving the norm of the vector. In practice, it consists in drawing two random numbers $rn_1 \in [0; 2\pi[$ and $rn_2 \in [0; 1[$ and defining new spin components as $\phi = rn_1$ and $\theta = arccos(1 - (2 \cdot rn_2)$. Indeed, the simple selection of a random (θ, ϕ) angle leads to a biased angle distribution where $\phi = 0$ and $\phi = 180$ "poles" are more frequent than the $\phi = 90$ "equator", as can be seen in Fig. 1.4. Finally, in the case of the Generalized-Heisenberg model, the tridimensional variation of a magnetic moment is performed by adding to its initial vector, a random vector (δX,δY,δZ).

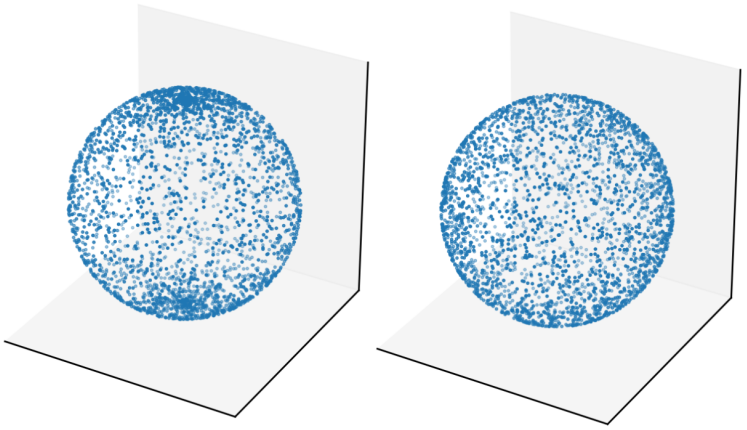

FIGURE 1.4: Comparison of a random distribution of angles obtained choosing (a) a random (θ, ϕ) angle set, or (b) drawing two random numbers $rn_1 \in [0; 2\pi[$ and $rn_2 \in [0; 1[$ and defining new spin components as $\phi = rn_1$ and $\theta = arccos(1 - (2 \cdot rn_2)$.

When simulating alloys or pure systems with defects (e.g. vacancies, see chapter 4), not only the magnetic but also the chemical evolution of the system must be taken

into account. The non-magnetic interactions of the system (chemical interactions) are expressed using the following formalism:

$$H_C = \sum_{i}^{N} E_0 + \sum_{i}^{N} \sum_{n}^{P} \sum_{j}^{Z} V_{ij}^{(n)} \tag{1.19}$$

where N is the number of atoms in the system, n is the range of interactions in terms of neighbor shells (the largest interaction range considered being P), Z is the number of neighbors of each interaction range. Here E_i is the on-site energy of the i-th atom, depending on its chemical species, and $V_{ij}^{(n)}$ represent the chemical pair-interaction between species of atoms i and j, at range n.

As the Monte Carlo simulations of this work are performed on a rigid lattice, the term *chemical relaxation* will be used in this thesis to describe atomic exchanges, and not actual position relaxations. In chapter 3, these atomic exchanges are performed using the Metropolis algorithm, in the canonical ensemble. It consists in selecting two randoms atoms in the system, exchanging their position and accept or not the change following the Metropolis criterion (see section 1.2.2).

Please note that it is possible to perform spin relaxations on-the-fly during chemical relaxations, which is done by equilibrating spins between two distinct atomic exchanges. The practical details are discussed in Chapter 3.

1.2.4 Vacancy formation calculations

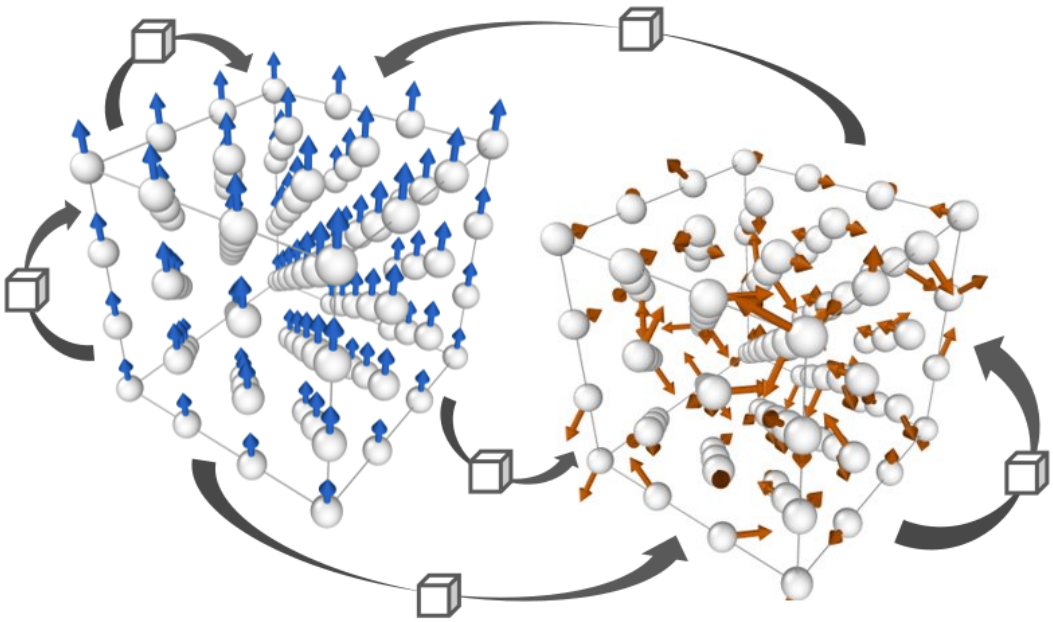

FIGURE 1.5: Schematic representation of the vacancy formation energy calculation principle. One vacancy is continuously exchanged with any atom of the two systems.

The determination of the vacancy formation energy via Monte Carlo simulations is not as straightforward as in DFT calculations. Indeed, the latter allows to directly

calculate the energy difference between systems with and without vacancies. In the case of Monte Carlo simulations, the energy noise leads to inconsistent energy differences when using equation 1.9, and prevents from using this approach. Instead, we propose a methodology in order to study the vacancy formation as a function of temperature. Considering two identical atomic systems, the first one (S1) being at thermal equilibrium while the other one (S2) remains in the 0K magnetic ground-state (in the case of bcc Fe, perfectly ferromagnetic). A single vacancy is randomly inserted in one of these two systems. The approach consists in performing Metropolis exchanges between the vacancy and any random atom of any system, as shown schematically in Fig. 1.5. The fraction of Monte Carlo steps that the vacancy spends in S1 compared to S2 gives the ratio between equilibrium vacancy concentration $C_v^{eq}(T)$ at temperature T and equilibrium vacancy concentration C_v^0 in the ideally ferromagnetic system. The concentration ratio between S1 and S2 leads to the vacancy formation free energy $G_v^{for}(T)$ at the equilibrium temperature of S1, as expressed in equation 1.20 (the 0K vacancy formation energy $G_v^{for}(0)$ is known from DFT calculations).

$$G_v^{for}(T) = G_v^{for}(0) - k_B T \cdot \ln(\frac{C_v^{eq}(T)}{C_v^0}) - G_{Fe}(0) + G_{Fe}(T) \tag{1.20}$$

where $G_{Fe}(0)$ and $G_{Fe}(T)$ are respectively the atomic energy of S2 and S1, determined by dividing the system total energy by the number of atoms composing it.

The same principle is used for the determination of vacancy equilibrium concentration concentration near a Mn solute in bcc Fe. One Mn atom is pinned in the S1 system and the number of Monte Carlo steps that the vacancy spends in the nearest-neighbor shell of the Mn atom is compared to the number of MC steps that the vacancy spends in the S2 system. The ratio between these two quantities provides the difference between vacancy equilibrium concentration in pure Fe at 1K with the vacancy equilibrium concentration in the nearest-neighbor shell of the Mn solute, at a given temperature.

1.2.5 Vacancy migration calculations

In order to compute vacancy migration via Monte Carlo simulation, the energy barrier of an atomic jump has to be calculated. To do so, we use a saddle-point Hamiltonian which formalism and parameterization are explicited in Chapter 4. The choice of a jump among the nearest-neighbors of the vacancy may be done using either Metropolis or residence time algorithm (see Chapter 4).

The approach is similar to many studies in the litterature [152, 146, 103], the only specificity being here that magnetic disorder is taken explicitly into account, so the calculation of the barrier depends on local magnetic moments, in addition to the local chemical environment dependence.

In practice, the target atom is virtually considered off-lattice at migration saddle-point. The saddle-point Hamiltonian is applied to calculate the interaction energy of this atom with its temporary neighbors. The energy difference between the saddle-point configuration and the initial stable lattice configuration is considered as migration enthalpy (see Fig. 1.2).

1.2.6 Self-diffusion

In this work, we consider the monovacancy nearest-neighbor jump as the only diffusion mechanism, which is a reasonable hypothesis in compact materials such as bcc Fe, out of irradiation. In that approximation, and without considering the influence of magnetic disordering on the correlation factor, the self-diffusion coefficient can be expressed as follows [1]:

$$D^* = a^2 f_0 C_v \Gamma \tag{1.21}$$

where a is the lattice constant, f_0 is the correlation factor, C_v is the equilibrium vacancy concentration and Γ is the jump frequency. For the ideal bcc lattice, without considering the magnetic disorder, the correlation factor equals 0.727 [1]. The validity of considering this value of correlation factor at any temperature is discussed in Chapter 4. The equilibrium vacancy concentration can be expressed as:

$$C_v = \exp(\frac{\Delta S_v^f}{k_B}) \cdot \exp(-\frac{\Delta H_v^f}{k_B T}) \tag{1.22}$$

with ΔS_v^f and ΔH_v^f being respectively the vacancy formation entropy and enthalpy. The jump frequency Γ is expressed in Section 1.1.7, in equation 1.15.

Another way to express the self-diffusion coefficient D^* is to simulate tracer diffusion experiments. In the Monte Carlo simulations, it is indeed possible to consider each atom as a tracer, and to follow its displacements during the whole simulation. Then, the self-diffusion can be expressed as follows [35, 36, 167]:

$$D^* = \frac{< r^2 >}{6t} \tag{1.23}$$

where $< r^2 >$ is the mean square displacement of the atoms and t is the physical time. In our simulations, the limited system size imposes an exaggerated vacancy concentration. Thus, in order to obtain the physical time, the simulation time has to be re-scaled as follows [151]:

$$t = \frac{t_{MC} C_{MC}}{C_v} \tag{1.24}$$

The expression of t depends on the algorithm: In the case of Metropolis simulations,

$$t = \frac{t_{MC} C_{MC}}{C_v} = \frac{N_{steps}}{Z C_v N_{atoms} \nu_0} \tag{1.25}$$

with N_{steps} and N_{atoms} being respectively the number of MC-steps performed in the simulation and the number of atoms composing the system, Z being the coordination number ($Z = 8$ for a bcc lattice) and ν_0 being the jump attempt frequency. If instead a residence time algorithm is used, then the eight nearest-neighbor jump frequencies are calculated and the characteristic time of a jump equals:

$$\tau = \frac{1}{\sum_{i=1}^{8} \Gamma_i} \tag{1.26}$$

The tracer diffusion method has the advantage of not attributing a value for the correlation factor, which is intrinsically taken into account. In fact, comparing both methods allows to estimate the effects of magnetic disorder on the correlation factor f_0 as shown in Chapter 4. As we consider in this work that the magnetic structure relaxation is infinitely faster than the chemical evolution, the determination of the f_0 correlation factor allows to ensure the convergence of the magnetic relaxations, by verifying that its value remains approximately 0.73 at any temperature.

In chapter 4, we also perform tracer diffusion simulations in the presence of a Mn solute, in order to predict the solute and solvent diffusion coefficients via Monte Carlo simulations. The principle is the same, although the mean square displacement must be calculated separately for distinct chemical species.

1.2.7 Effect of Quantum statistics

In the framework of classical physics, the energy distribution of spin excitations (magnons) is considered continuous, which implies that infinitesimal spin fluctuations are always possible even at low temperatures as a sufficient thermal energy is available to excite the system. This feature leads to contradictory results as the heat capacity don't reach 0 and the magnetic entropy diverges as the temperature tends to 0K. [179]

If considering discrete energy levels, these infinitesimal thermal excitations are no more possible as the thermal energy is calculated using the quantized Planck's energy distribution. According to several literature studies, magnon energy quantization could be so important in bcc Fe that the use of classical statistics should be avoided over the whole ferromagnetic temperature domain. [57, 113, 78]

In chapter 4, we investigate on the influence of such quantum effects on diffusion properties.

As explained in section 1.2.2, the transition probability using the classical Metropolis algorithm is:

$$\begin{cases} 1 \text{ if } \delta E <= 0 \\ \exp(\frac{-\delta E}{\eta}) \text{ if } \delta E > 0 \end{cases}$$

where the scaling factor is $\eta = k_B T$ using the Boltzmann distribution. Switching from classical to quantum statistics (using the Bose-Einstein distribution) leads to the following expression of the scaling factor [179]:

$$\eta(T) = \int_0^\infty \frac{E}{\exp(E/k_B T) - 1} \cdot g(E,T) dE \tag{1.27}$$

where E is the energy of a magnon at a wavevector $\mathbf{q}$, $g(E,T)$ is the magnons density of states (mDOS) at temperature T and magnon energy E. As arises from equation 3.5, the corner-stone of this quantum correction is the knowledge of the mDOS. In order to obtain the magnons dispersion relation, the approach of Bergqvist *et al.* [12] is applied.

The practical details of this approach are described in Chapter 3 (section 3.0.1).

Chapter 2

Local environment dependency of Mn magnetism in bcc Fe-Mn alloys

---

In this chapter, the effects of local chemical environment on Mn magnetism is studied in bcc Fe-Mn alloys by means of DFT calculations. The energetic and magnetic properties of Mn solutes are discussed regarding the chemical order, the presence of a vacancy, and the presence of typical interstitial impurities. This study provides a good understanding of key properties of Fe-Mn alloys, which are also necessary for the finite temperature simulations in the following chapters.

2.0 State of the art

The magnetic behavior of Mn solutes in dilute Fe-Mn systems, which is a first step towards the understanding of properties in Fe-Mn alloys with various concentrations, is still unclear despite previous efforts [110, 85]. Existing theoretical studies do not all agree on even the magnetic ground state of a single substitutional Mn atom in bcc Fe. The reported Mn magnetic moment ranges from -3.0 to 1.0 μ_B. Positive and negative moments respectively denote an AF and a FM state with respect to the lattice Fe moments. The value seems to be very sensitive to the various DFT approximations such as the parameterization of the GGA exchange-correlation functional and the use of different types of pseudo-potentials, as pointed out by Olsson *et al.* [124]. The large discrepancy may also arise from the presence of two collinear energy minima for a Mn solute in bcc Fe, showing a moment either parallel or antiparallel to the lattice Fe moments, as mentioned in an early theoretical work [5]. These two minima must be taken into account for an accurate description of Mn magnetism in bcc Fe-Mn alloys. To the best of our knowledge, it is not the case in most of previously published studies, which may be a possible cause for many discrepancies described in the following paragraphs.

Several DFT studies were focused on Mn interaction with another Mn solute, and with point defects and impurities. Systematic studies of 3*d*-solutes in α-Fe including Mn show some controversial results. DFT based calculations performed with

projector augmented wave (PAW) potentials reveal an attractive behaviour between two nearest-neighbors Mn atoms [124, 9], whereas another study performed using Vandebilt ultra-soft pseudo-potentials (USPP) showed the opposite [163]. As for the isolated Mn, these energetic results need to be discussed considering different magnetic coupling possibilities of the two Mn atoms. It was also shown that a vacancy and a Mn solute exhibit an attractive behavior[124, 107, 162, 116, 34, 9]. Concerning a Mn solute interacting with an interstitial impurity, a DFT-USPP study reported an attraction, with a binding energy between Mn and a first-neighbor C (resp. N) interstitial of 0.26 eV (resp. 0.19 eV) [182]. This attractive behavior for C is confirmed by another DFT-PAW study which reports a lower binding energy (0.12 eV) between Mn and a first-neighbor C interstitial impurity [9]. However, these studies have not explicitly discussed the magnetic state variation of the Mn atom. Further investigation is required to address this feature and magneto-energetic interplay.

Concerning Fe-Mn alloys beyond the extremely dilute limit, it has been shown via DFT that the heat of formation of bcc Fe-Mn is always positive, in a study performed over the whole range of concentration [96]. This finding agrees with earlier data from Tight Binding - Linear Muffin Tin Orbitals (TB-LMTO) calculations[110]. These results are consistent with available experimental works[147, 128] revealing an unmixing tendency. However, a systematic concentration dependent magnetic analysis is still missing.

Experimentally, some magnetic properties of Fe-Mn alloys have been studied a few decades ago using Mössbauer spectroscopy [72, 175, 158], nuclear magnetic resonance (NMR) [68, 149, 136], small angle neutron scattering [27] and magnetization measurements [181]. The motivation of these studies was to understand the linear decrease of the total magnetization of Fe-Mn systems with increasing Mn concentration, following closely the Slater Pauling curve, up to 11 at.% Mn, before a sharp drop [126, 13, 85]. Assuming the Fe moment to be constant, it was deduced that the average Mn moment ranges between 0.8 and 1 μ_B, parallel to the Fe moments. This simple scenario could explain the linear decrease of the total magnetic moment by a magnetic dilution effect.

Polarized neutron diffuse scattering experiments [71] have reported an average Mn magnetic moment of -0.82 and -0.23 μ_B for respective Mn concentrations of 0.8 and 1.8 at.%. It must be noted however that this study was performed at room temperature, while a more recent study of the same group [128] has shown a different result (0.62 μ_B at both 0.9 and 2.9 at.% Mn) using the same experimental technique at 77K. Several hypotheses may explain this discrepancy: firstly the room temperature study [71] may involve significant phononic effects, which may have an impact on the obtained results. Also, the value obtained from neutron scattering experiments is actually a $\Delta\mu$ difference between the average μ_{Fe} and μ_{Mn}, meaning that the uncertainty on the value may also lead to a change of the Mn magnetic moment sign. Some local stress may also be present in experimental samples due to thermal treatments, the precise microstructures were not reported. Finally, the most recent

of these studies [128] also reveals the existence of atomic short-range order in the solution (at 2.9 at.% Mn), which may have an effect on the average magnetic moment of Mn atoms. While these two studies are the only existing experimental data at concentrations lower than 2 at. % Mn, some other experimental works showed moments between 0.6 and 1.0 μ_B for a Mn concentration of 2-5 at.% Mn.[128, 119, 25, 132] Compiling these data seem to show a transition from an AF to a FM Fe-Mn coupling tendency with increasing Mn concentration. A quantitative conclusion is however difficult to draw because the discrepancies at concentrations lower than 2 at. % Mn. None of these works offer a systematic study over a large concentration range. Overall, it is noticeable that low concentration results remain uncertain while higher concentration studies show a FM Fe-Mn coupling tendency. The transition between these two regimes appears at approximately 2 at.% Mn.

On the theoretical side, previous results on Fe-Mn magnetic interactions in the alloys also showed some discrepancies. Some calculations performed using TB-LMTO showed negative Mn moments going from -2.5 to -3.0 μ_B over the 5-20 at.% Mn concentration range [52]. The latter method also predicted a transition between a large negative moment and a smaller positive one (from -1.5 to 1 μ_B) [110], although the critical concentration of this transition (6-8 at.% Mn) is overestimated compared to experimental data (most authors report positive values for Mn concentrations larger than 2 at.% Mn in experimental studies) [71, 119, 25, 132]. Calculations were also performed using the coherent potential approximation with the Korringa-Kohn-Rostoker (KKR-CPA) method and showed a transition between a strong AF state and a weaker FM state at 12 at.% Mn [85]. However, CPA is known not to be suitable for addressing properties depending on chemical short range order (SRO), which is the case of Mn magnetism in bcc Fe [132]. It is clear that theoretical results do not agree with the experimental data on the AF to FM transition of the Fe-Mn interaction. One possible reason may be due to the presence of multiple magnetic minima in the Fe-Mn alloys, which are not all considered in the calculations. Also, all these studies only considered random solutions while it was shown that bcc Fe-Mn alloys show significant unmixing tendencies [147, 128]. It is then necessary to investigate the effects of Mn clustering on the magnetic properties.

This work aims at elucidating the dependence of Mn magnetism in various local environments in bcc Fe-Mn alloys, namely a Mn solute, being isolated or forming a cluster, and in the presence of vacancies or interstitial impurities, and the dependence of Mn magnetism on the alloy concentration. Based on the obtained results, we also attempt to provide explanations for the existing discrepancies between theoretical and experimental studies.

The chapter is organized as follows: The first section is focused on the behavior of isolated Mn solutes in a bcc iron lattice. The second part concerns the magnetic structures of bcc Fe-Mn solid solutions as a function of Mn concentration. The third section deals with Mn clusters in bcc Fe. Finally the fourth and the fifth parts are

devoted to the interaction between Mn atoms and respectively vacancies and interstitial impurities (C,N,O) and their impact on the Mn magnetism.

2.1 Mn solutes in bcc Fe

The magnetic properties of isolated single-atom Mn solutes in bcc iron show an atypical feature, as described in a previous theoretical study using LMTO Green's functions [5]. Anisimov *et al* have indeed noticed two energy minima with distinct Fe-Mn magnetic interactions. The present calculations within a collinear approximation with constrained local magnetism (see chapter 1 for more details) confirm the presence of these two energy minima, as shown in Fig. 2.1. For a Mn concentration of 1.9 at.% (1 Mn atom in a 54 atom-site Fe system), the lowest energy minimum is found with a Mn moment of -1.9 μ_B anti-ferromagnetically (AF) coupled with Fe moments in the lattice (referred as AF-Mn in the following). The other rather flat minimum is found for FM coupled Mn with Fe moments (referred as FM-Mn in the following), with a smaller magnitude of approximately 0.7 μ_B. In order to verify if the used 54-atom cell is large enough for the Mn atom to be considered isolated, we studied the convergence of the relative energy between these two states and their respective magnetic moment magnitude as functions of the simulation supercell size. The results are given in Table 2.1. We note from this table that the energy differences between the AF-Mn and the FM-Mn are all similar, the discrepancy being at most 0.03 eV, which is close to the estimated DFT error bar (0.02 eV, see section 1.1.2 of chapter 1). The change of the magnetic moment of the AF-Mn is also close to the DFT error bar (0.1 μ_B, see section 1.1.2), while the moment of the FM-Mn shows a larger variation. The latter may be due to the shape of the energy minimum, which is rather flat, as shown in Fig. 2.1. Remaining in the collinear approximation, the estimated energy barrier from the AF to the FM-Mn state is 0.07 eV (Fig. 2.1).

System size	Mn at.%	$k-$grid	ΔE (meV)	$\mu_{\text{Mn-AF}}$	$\mu_{\text{Mn-FM}}$
54	1.9 at.%	$5\times5\times5$	50.7	-1.91 μ_B	0.72 μ_B
128	0.8 at.%	$4\times4\times4$	68.5	-1.98 μ_B	0.67 μ_B
250	0.4 at.%	$3\times3\times3$	52.7	-1.94 μ_B	0.85 μ_B
432	0.2 at.%	$3\times3\times3$	38.4	-1.86 μ_B	0.56 μ_B

TABLE 2.1: Magnetic and energetic properties of an isolated Mn solute in bcc Fe for various supercell sizes resulting in different Mn concentrations. ΔE is the energy difference between AF-Mn and FM-Mn magnetic states. $\mu_{\text{Mn-AF}}$ and $\mu_{\text{Mn-FM}}$ are the magnetic moment magnitudes of the respective AF-Mn and FM-Mn.

Fe and Mn are close neighbors in the Periodic Table of Elements. As expected, only minor lattice distortion is induced by the substitution of a Mn atom in bcc Fe. In the case of AF-Mn, the Fe-Mn $1nn$ interatomic distance is very slightly larger than the $1nn$ Fe-Fe distance in pure Fe (Δd = 0.0025 Å) while in the case of FM-Mn,

the 1*nn* Fe-Mn distance is shorter compared to the pure Fe bulk (Δd = -0.0144 Å). Consistently, AF-Mn has a slightly larger Voronoï volume (11.37 Å^3) than pure Fe (11.36 Å^3) which itself has a higher one than FM-Mn (11.20 Å^3). Also, we notice that the local charge density around the Mn atom is higher in the FM-Mn state than in the AF-Mn state.

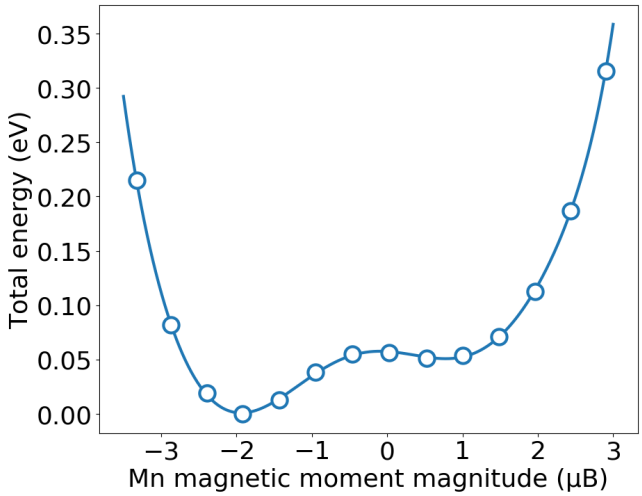

FIGURE 2.1: Total energy as a function of the magnetic moment magnitude of an isolated Mn atom in bcc Fe.

Concerning the electronic projected density of states (PDOS), we observe in Fig. 2.2 that a NM Mn atom in bcc Fe (from a constrained Mn moment calculation) has a sharp peak on its spin-up PDOS at the Fermi level, indicating (as expected) an instability against the development of magnetism. The spin-down states are mainly concentrated in two peaks located respectively above and below the Fermi level. The AF-Mn state appears by shifting a major part of the spin-down states to lower energies, including some states initially located above the Fermi level, while the main peak of the spin-up band is shifted to above the Fermi level. The PDOS changes are consistent with the high energetic stability of this AF-Mn state. On the other hand, in the FM-Mn case, there is no major difference between the NM and the FM PDOS on the spin-up band, except a slight split of the peak at the Fermi level, decreasing weakly the density of states at the Fermi level. Concerning the spin-down band, a slight shift to higher energies is noticeable, which explains the appearance of a small magnetic moment. The FM-Mn state is only 5 meV below the NM-Mn state.

Non-collinear (NC) magnetism calculations were also performed to explore the possible presence of NC minima. For a Mn concentration of 1.9 at.% (1 Mn atom in a 54 atom Fe system), no other minimum was found besides the two collinear solutions, as shown in Fig. 2.3. Instead, a significant barrier separates these two minima. One can notice that the non-collinear energy barrier between the two minima is slightly higher than the collinear barrier. Note that the difference between these barriers is close to the estimated error bar (0.02 eV, see section 1.1.2). To calculate this energy-angle curve, the direction of the Mn magnetic moment was constrained

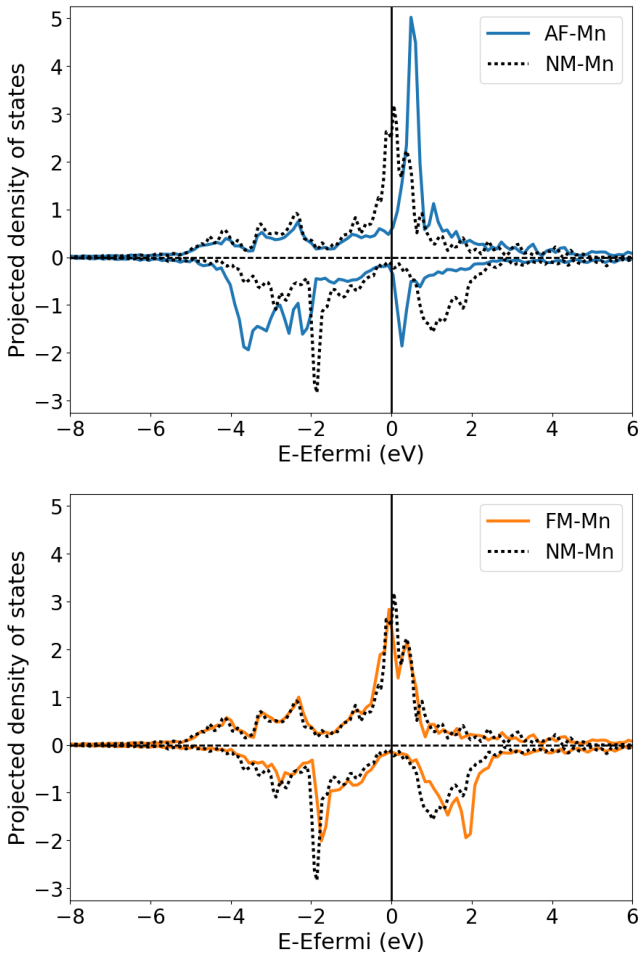

FIGURE 2.2: Projected density of states on an isolated AF-Mn or a FM-Mn, compared to the PDOS on an isolated non-magnetic Mn atom in bcc Fe.

to certain angles, and we allowed the magnetic moment magnitude to relax. The bottom plot of Fig. 2.3 shows that, overall, the Mn moment magnitude gradually increases from the FM-Mn state to the lowest energy AF-Mn state, except for the case of 90 where two energetically degenerate states are found, with a particularly small moment in one of them. These non-collinear data are useful to parameterize Heisenberg-like models for Monte Carlo simulations, in order to describe the magnetic behavior of Fe-Mn alloys at finite temperatures [40].

It is also worth mentioning that the impact of the Mn solute on the local magnetic moment of surrounding Fe atoms is rather limited. For a Mn concentration of 0.2 at.% (1 Mn atom in a 432 atom-sites Fe system), the variation of Fe atoms magnetic moment magnitude is at most 5%, similar to what has been shown in Fe-Cr alloys [76].

We note that the energy difference between AF-Mn and FM-Mn states highly depends on the lattice constant of the system. Namely, lower lattice constants tend to favor the FM-Mn state, and vice-versa. It was shown by King *et al.* [74] that a hydrostatic compression modeled by a 2% strain is sufficient to switch from AF-Mn

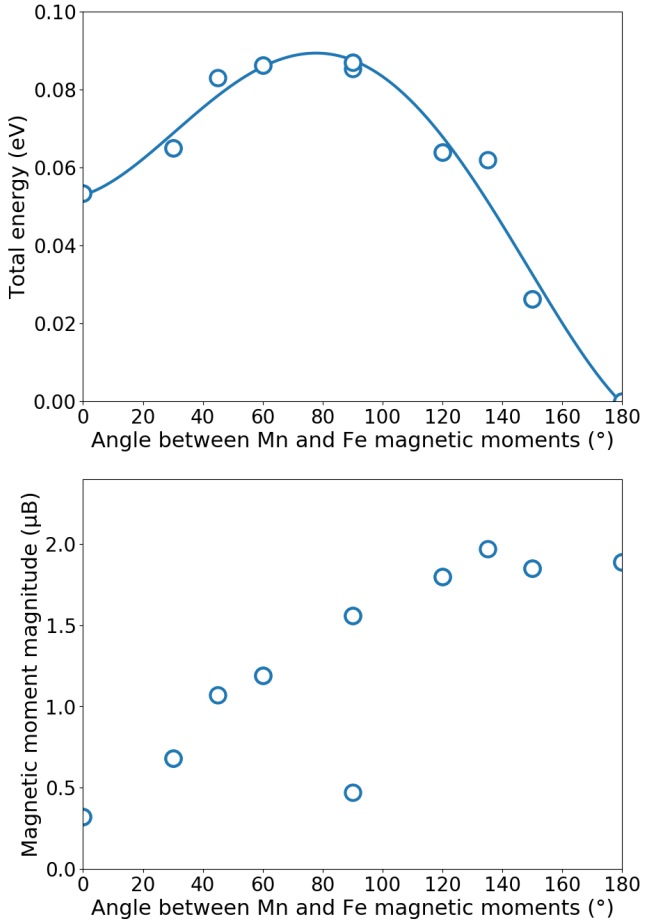

FIGURE 2.3: Total energy (top) and magnetic moment magnitude (bottom) as functions of the angle between moments of an isolated Mn and the lattice Fe atoms.

to FM-Mn. Because of this dependence, we have observed that when using the experimental lattice constant of bcc Fe (2.856Å) instead of the GGA equilibrium lattice constant (2.832Å), the energy difference between AF-Mn and FM-Mn increases from 0.05 eV to 0.15 eV.

Finally, the energy difference between AF-Mn and FM-Mn is also sensitive to the exchange-correlation functional. We have performed some tests using the LDA functional (all the other computational details remaining identical) which show that with experimental lattice constant, $\Delta E = 0.01$ eV in favor of the AF-Mn state, in the range of the method accuracy (see chapter 1). When performing LDA calculations using either the GGA or the LDA equilibrium lattice constant (respectively 2.832Åand 2.727Å), the AF-Mn state is found unstable. Hence, it should be kept in mind that the magnetic state of Mn at ground-state may depend on the ab-initio methodology. We have opted in this work for the GGA exchange-correlation functional as it is known to be more reliable for the study of Fe-based alloys. Concerning the pseudo-potential effects, we have calculated the relative stability between AF-Mn and FM-Mn states with an all-electron GGA-PBE approach, FP-LAPW as implemented in Wien2k. The results are very close to the present GGA-PBE-PAW results.

2.2 Bcc Fe-Mn solid solutions

Most of the present study is devoted to properties of dilute Fe-Mn alloys, because it is known that the bcc Fe-Mn phase is thermodynamically stable only up to a few percent of Mn, before entering in an α+γ dual-phase domain [176, 96]. However, in order to have a thorough understanding of the dependence of the magnetic behavior on the alloy concentration, it is interesting and relevant to perform a systematic study for all concentrations. Special Quasirandom Structures (SQS) [184], which have negligible short range order (SRO), are adopted to mimic the random solid solution even with rather small simulation cells. In the SQS systems, Fe and Mn atoms were distributed in 54 and 128 atoms cells. Mixing energy of these configurations was calculated using the following expression:

$$E^{mix}(\text{Fe-Mn}) = \frac{E^{tot}(n\text{Fe} + p\text{Mn}) - nE(\text{Fe}) - pE(\text{Mn})}{n+p} \tag{2.1}$$

where $E^{tot}(n\text{Fe} + p\text{Mn})$ is the total energy of the Fe-Mn solid solution, $E(\text{Fe})$ is the energy per atom of pure bcc Fe (in its lowest energy magnetic state: FM) and $E(\text{Mn})$ is the energy per atom of pure bcc Mn (in the lowest energy magnetic state: AFD). As can be seen in Fig. 2.4, the obtained mixing energies are positive for all the concentrations, which reveals an unmixing tendency. Moreover, the shape follows well the regular solution model (shown with the orange curve corresponding to the expression $E^{mix} = A \cdot x_{\text{Fe}} \cdot x_{\text{Mn}}$) with A = 192 meV (18500 J/mol). It is in good agreement with earlier DFT results showing A = 20000 J/mol [96] and an experimental value (A = 19500 J/mol)[62]. A previous TB-LMTO calculation also obtained a value of the same order of magnitude (A = 23700 J/mol) [110]. In Fig.2.4, there are noticeable energy differences between systems at the same concentration with the same atomic configuration but with different magnetic states.

Concerning the magnetic properties, we rather focus on bcc Fe-Mn alloys in the Fe-rich domain, up to 50 at.% of Mn. Fe and Mn local magnetic moments are plotted in Fig. 2.5 for all the atoms in all the considered SQS configurations up to 50 at.% Mn. We note a sharp peak for Fe moment around 2.2 μ_B showing a very small perturbation of the bcc-Fe moment due to the presence of Mn atoms. On the other side, Mn moment shows a large dispersion. The average magnetic moment in these SQS solid solutions from Fig. 2.6 shows a linear decrease with increasing Mn concentration, in agreement with available experimental studies. Indeed, it was shown experimentally that the average magnetic moment of Fe-Mn alloys tend to decrease linearly up to 11 at.% of Mn, before a sharp drop. It was hypothesized that the linear decrease is due to the magnetic dilution effect (Mn having a constant magnetic moment lower than the Fe moment) and that the sharp drop at higher Mn concentrations is due to the emergence of non-ferromagnetic phases, [181] but none of these studies led to a final conclusion. From the present results, we suggest that the slope change should correspond rather to a structural phase transition because if the bcc lattice is theoretically kept up to 50 at.% of Mn as in this study, a linear decrease of the average

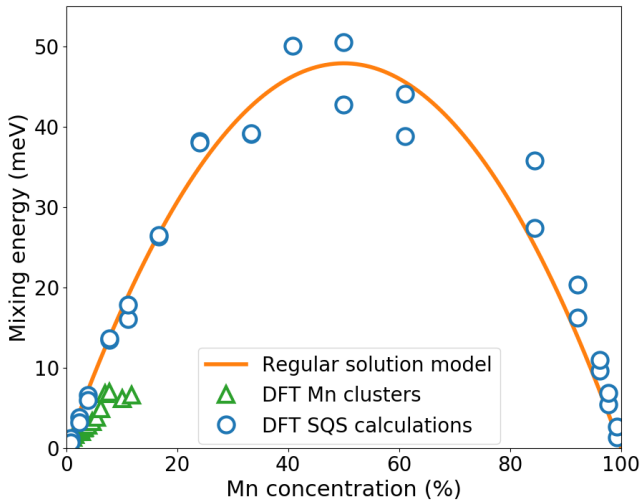

FIGURE 2.4: Mixing energy as a function of Mn concentration (expressed in atomic percent) in bcc Fe-Mn SQS solid solutions and systems composed of Mn clusters in bcc Fe, taking as references the FM bcc Fe and the AFD bcc Mn.

magnetic moment is observed for all the concentrations, in very good agreement with the Slater-Pauling curve. Although we may expect a slight deviation from the linear behavior at low Mn concentration because of the magnetic transition of Mn atoms (Fig. 2.6), the effect is not visible.

Having a closer look on the magnetism of Mn atoms, Fig. 2.6 shows an average Mn moment antiparallel to Fe moments at the lowest concentration, followed by a rapid decrease of the moment magnitude with increasing Mn concentration. This finally leads to a transition from AF to FM Fe-Mn coupling tendency at approximately 6 at.% Mn (with the SQS systems only), and then the average Mn magnetic moment stabilizes to a value around 0.8 μ_B, parallel to Fe moments. As mentioned above, most of Mn atoms at the dilute limit are isolated and remain in an AF-Mn state. At a high concentration (above 10 at.% Mn) the rather constant value of 0.8 μ_B results from the presence of an approximately constant fraction of 75% FM-Mn and 25% AF-Mn atoms in each SQS configuration, as can be seen in Fig. 2.7. Interestingly, both types of Mn present an average moment magnitude of around 1.6 μ_B (Indeed, 1.6*0.75-1.6*0.25=0.8). These features lead to a scenario compatible with the simple magnetic dilution model proposed from experimental data, assuming a constant Mn moment which is parallel and smaller than Fe moments. Of course, those experiments have only access to average (instead of individual) magnetic moments [119, 25, 132].

If we focus on Mn magnetism in the dilute Fe-Mn alloys, up to a few percent of Mn, some experimental data, summed up in Table 2.2 tend to show that Mn is coupled FM with Fe between 2 and 9 at.% of Mn concentrations while another experimental study finds an AF Fe-Mn coupling at Mn concentrations below 2 at.% [71]. By compiling these results, we note that an AF-Mn to FM-Mn transition is also found in experimental works but at a lower Mn concentration (around 2 at.% Mn)

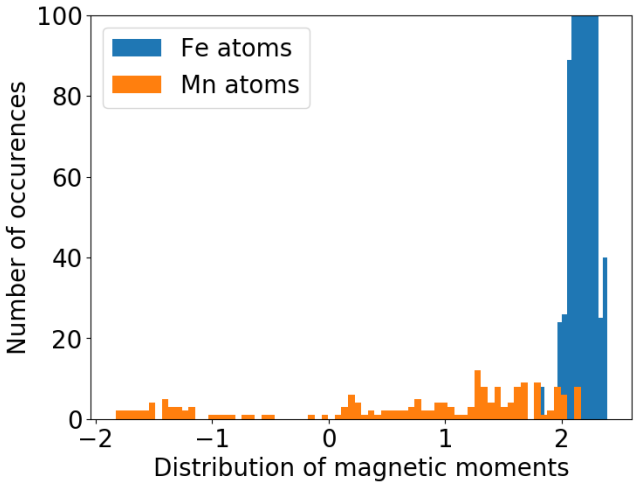

FIGURE 2.5: Distribution of Fe and Mn local magnetic moments in Fe-Mn SQS alloys, up to 50 at.% Mn.

than our prediction based on SQS systems. Previously, a theoretical study using TB-LMTO method also predicted a transition concentration around 6-8 at.% Mn, in good agreement with our DFT results [110]. However, as explained in section 2.0, another study [128] from the same group shows contradictory results, obtained with the same method at another temperature. The existence of this transition from the experimental point of view is still debatable.

This discrepancy between experimental data and the DFT results may be due to various possible phenomena: For instance, bcc Fe-Mn alloys have an unmixing tendency, the formation of Mn clusters in Fe should be energetically favorable compared to random solid solutions. Indeed, a recent Mössbauer based study [147] reported that bcc Fe-Mn alloys tend to increase their short range order through clustering. Depending on the thermal treatments and the speed of quenching applied to the experimental samples, the considered Fe-Mn solutions may not be fully disordered. This may be a possible source of discrepancy on the magnetic behavior based on experimental and theoretical studies, if the latter account for SQS solid solutions only. Also, recent DFT works [105] have shown that the presence of carbon impurities in bcc Fe tend to have significant effects on Mn solutes magnetism. The presence of interstitial impurities (often found in iron based alloys) in experimental samples could also affect the magnetic moment of Mn atoms, even though it is not expected to be a major cause because of the generally low impurity content. In addition, the discrepancy may also be related to the presence of structural inhomogeneities in the samples such as grain boundaries and precipitates, but these features are out of the scope of this study. In the following sections, we will focus on Mn clustering, vacancy and impurities effects.

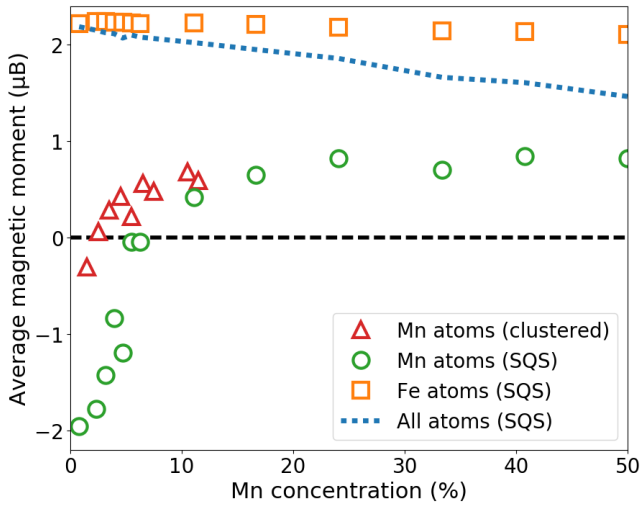

FIGURE 2.6: Average magnetic moment of Fe atoms, of Mn atoms and of all the atoms in Fe-Mn alloys either with a SQS structure or containing a Mn cluster, as a function of Mn concentration (expressed in atomic percent).

Reference	[Mn]	Avg. μ_{Mn}
Kajzar et al[71]	0.8 at.%	-0.82 μ_B
Kajzar et al[71]	1.9 at.%	-0.23 μ_B
Parette et al[128]	0.9 at.%	0.62 μ_B
Parette et al[128]	2.9 at.%	0.62 μ_B
Child et al[25]	2 at.%	1.0 μ_B
Radhakrishna et al[132]	3 at.%	0.8 μ_B
Radhakrishna et al[132]	6 at.%	1.0 μ_B
Radhakrishna et al[132]	9 at.%	0.8 μ_B
Nakai et al[119]	5 at.%	0.7 μ_B

TABLE 2.2: Experimental values of Mn average magnetic moment in dilute bcc Fe-Mn for various Mn concentrations.

2.3 Mn clusters in bcc Fe

Before addressing Mn clusters, the interaction between two isolated Mn solutes was investigated as a function of the distance between them. It was found that as nearest neighbors (1nn) or second nearest neighbors (2nn), Mn atoms tend to be AF with each other. One of them is therefore FM to the lattice Fe atoms, at variance with the isolated Mn case. This results from a dominance of Mn-Mn AF tendency over the Fe-Mn anti-ferromagnetism at such short separation distances. This behavior is opposite to the Fe-Cr alloy case, where Fe-Cr AF interactions prevail over the Cr-Cr anti-ferromagnetism [40]. The Mn local moments for the 1nn separation are -1.7 μ_B (AF-Mn) and 1.4 μ_B (FM-Mn). For the 2nn case, the corresponding Mn moments are -1.8 and 1.1 μ_B. Please note that the FM-Mn within the dimer has a significantly increased moment magnitude compared with an isolated FM-Mn, especially for the 1nn case. At a larger Mn-Mn distance, with the two Mn atoms as third nearest

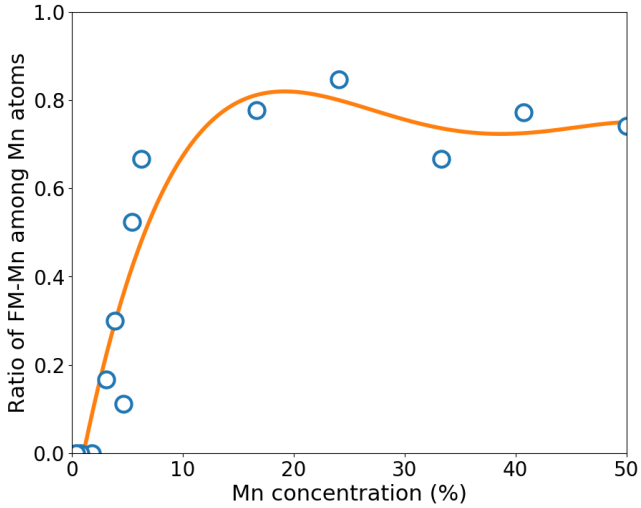

FIGURE 2.7: Ratio of FM-Mn among Mn atoms in Fe-Mn random solutions as a function of Mn concentration (expressed in atomic percent). The fitted polynomial function (orange curve) aims at illustrating the general trend.

neighbors ($3nn$) and beyond, both of them prefer to couple AF with Fe moments with magnetic moments converging towards the value of an isolated Mn in bcc Fe. Fig. 2.8 shows the binding energy between two Mn atoms in bcc Fe as a function of the separation distance for various collinear magnetic configurations. The Mn-Mn binding energy is calculated as follows:

$$E^{bind}(\text{Mn-Mn}) = -E^{tot}((n-2)\text{Fe+2Mn}) + 2E^{tot}((n-1)\text{Fe+1Mn}) - E^{tot}(n\text{Fe}) \quad (2.2)$$

with $E^{tot}((n-1)\text{Fe+1Mn})$ at the magnetic ground state (Mn coupled AF with Fe). Using this expression, positive binding energies stand for attractive behaviors, while negative binding energies stand for repulsion. Fig. 2.8 shows that, in the lowest-energy magnetic state, the $1nn$ Mn dimer exhibits a very slight attraction (0.012 eV), whereas there is a repulsion from a $2nn$ to a $7nn$ distance. Note that the magnitude of the attraction is within the error bar of the present DFT calculations (0.02 eV). The binding energy converges to 0 from the 8nn, Mn atoms are then considered fully isolated. At a $1nn$ distance, the dimer composed of two FM-Mn or two AF-Mn atoms is respectively 0.045 eV or 0.062 eV higher in energy than the magnetic ground-state dimer (AF-Mn + FM-Mn). The trend remains the same for a $2nn$ dimer. It is worth mentioning that the dimer with two AF-Mn comes to have even a slightly higher energy than the dimer with two FM-Mn atoms (0.017 eV higher for the $1nn$ case). This scenario may be understood assuming a dominant Mn-Mn AF interaction, over the Fe-Mn anti-ferromagnetism at these shortest separations: the two-AF-Mn dimer (FM coupling between the Mn atoms) exhibiting large Mn moments: -2.43 μ_B per Mn for the $1nn$ case, is energetically penalizing, while the two-FM-Mn dimer develops a magnetically less unfavorable situation by decreasing the

moment magnitudes (0.18 μ_B per Mn for the 1*nn* case).

Bakaev *et al.* [9] have noticed that among several substitutional solutes, Mn is the only one to show attractive solute-solute interactions in bcc Fe at a 1*nn* distance. That study leads to the conclusion that this specificity is mainly due to the flexibility of the Mn magnetic moment, which means an easy variation of the moment magnitude, to adapt different local environments. Our study also reveals such flexibility, as reflected by the existence of distinct moment magnitudes of Mn in bcc Fe (Fig. 2.5). Furthermore, as mentioned above, two minima (AF-Mn and FM-Mn) exist for a single Mn solute, which provides an additional possible state for each Mn in the dimer. To our knowledge, the possibility of a Mn dimer with one AF-Mn and one FM-Mn was not considered in Ref. [9]. Also, the results from Bakaev *et al.* and the present ones may not be directly comparable, as different parameterization of GGA are used (PW91 in Ref. [9]).

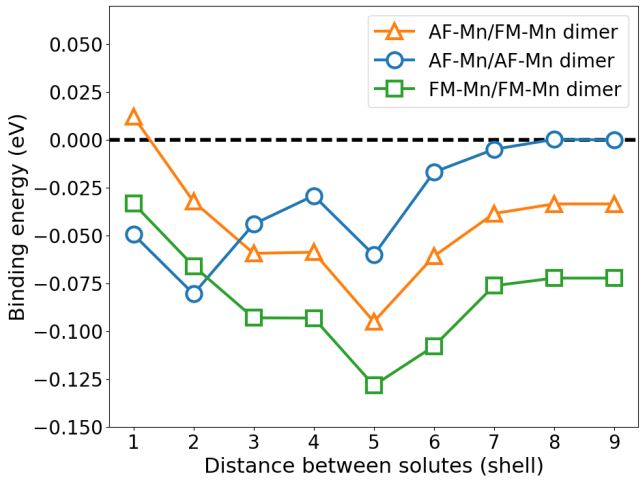

FIGURE 2.8: Binding energy between two Mn atoms in a 432-atom bcc Fe supercell as a function of Mn-Mn separation distance, taking isolated AF-Mn as the reference. Positive binding energies mean attraction.

In addition, non-collinear magnetism calculations were performed in the case of 1*nn* Mn atoms to explore the possible presence of non-collinear energy minima, which may provide a compromise between the preference for a single Mn to be AF to Fe, and the emergence of a FM-Mn in the dimer, due to Mn-Mn interaction. From our NC calculations, no configuration was found with a lower energy than the collinear magnetic ground state. Fig. 3.13 shows the binding energy for some non-collinear configurations obtained, along with the respective spin configurations. Calculations were performed with several different initial spin arrangements. All the cases converged to either the collinear ground state (a) or the NC (b) configuration, which seems to be the only stable NC state. At variance, the (c), (g) and (e) configurations were obtained using constrained local magnetism, by imposing the Mn spin directions but relaxing the spin magnitudes. As can be seen in Fig. 3.13, the NC

metastable (b) state is higher in energy than the collinear ground state (lower in binding energy), but less energetic than other collinear states ((d) and (f)). Also, please note that these energy differences are rather close to the estimated error bar of the calculation method or even fall within it. Moreover, we may expect a non-negligible occupation rate of the metastable states, including the NC-(b) state at finite temperatures. It is in principle also relevant to perform the study of various-sized Mn clusters beyond the collinear approximation. However, such a systematic NC magnetic study is significantly computationally demanding and out of the scope of this chapter. A full non-collinear study will be considered in a future work. The following sections only deal with collinear calculations.

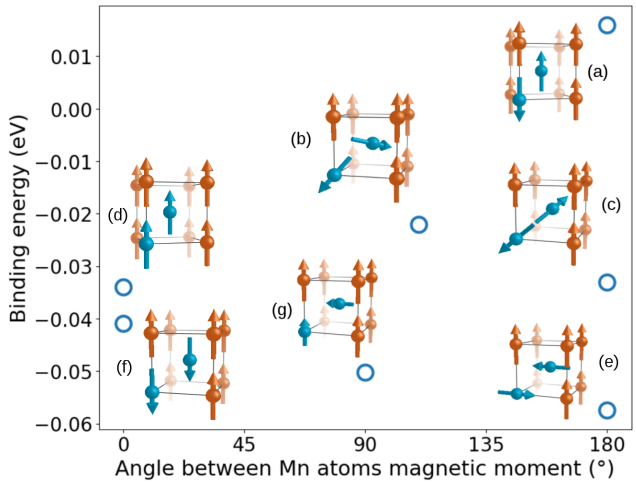

FIGURE 2.9: Binding energy (denoted by blue circles) of a 1*nn* Mn dimer, with the AF-Mn as reference, for various shown collinear and non-collinear magnetic configurations. Mn and Fe atoms are respectively represented by blue and orange spheres, and orientations of local magnetic moments are indicated with arrows.

Concerning the study of n-Mn clusters in bcc Fe with n = 3 to 15, we employed 250-atom supercells and various atomic configurations (more or less compact) and magnetic arrangements were considered for each cluster size. The lowest energy atomic and magnetic configurations of these clusters are shown in Fig. 2.10. It was found that the average binding energy of these clusters, calculated using the following equation:

$$E^{bind}_{avg}(p\text{Mn}) = \frac{-E^{tot}((n-p)\text{Fe} + p\text{Mn}) + pE^{tot}((n-1)\text{Fe+1Mn}) - (p-1)E^{tot}(n\text{Fe})}{p} \tag{2.3}$$

is all positive (energetically favorable) and increases with the number of Mn atoms, as shown in Fig. 2.11. The attraction between Mn atoms confirms the unmixing tendency showed in the previous section on solid solutions. As can be seen in Fig. 2.4, for Mn concentrations ranging from 1 to 12 at.%, mixing energy of Fe-Mn systems containing clusters, in their lowest-energy magnetic state is indeed lower

than the energy of random Fe-Mn alloys with the same Mn content. This result is in agreement with an experimental study which revealed via polarized neutron scattering the clustering tendency of a dilute Fe-Mn alloy containing 2.9 at.% Mn [128].

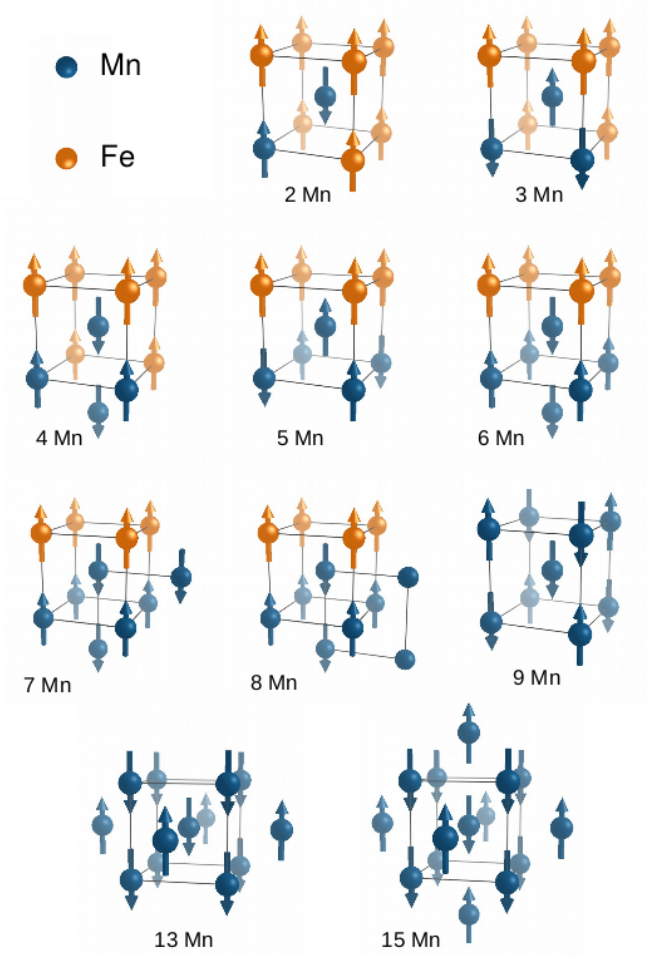

FIGURE 2.10: Schematic representation of the lowest energy atomic and magnetic configuration found for n-Mn clusters in a bcc Fe lattice, for n = 2 to 15. Magnetic moment orientations are indicated by arrows. In the case of negligible moment magnitudes, atoms are represented without arrows.

Regarding the magnetic ordering of the Mn clusters, it is noticeable from the lowest energy magnetic configurations (Fig. 2.10) that the Mn-Mn magnetic interaction is dominant compared to Fe-Mn coupling, as already noted for the Mn dimer. Indeed, these magnetic arrangements tend to satisfy in priority the AF Mn-Mn 1nn and 2nn coupling. For example, at least 50% of 1nn Mn-Mn pairs in a cluster show an AF coupling. Some n-Mn clusters (n = 2, 3, 4, 6, 7) present 100% of AF 1nn Mn-Mn pairs. At variance, Fe-Mn magnetic interaction does not show any clear tendency, the fraction of 1nn AF Fe-Mn pairs varies from 20 to 70%. Moreover, switching every Mn atom magnetic moment (from AF-Mn to FM-Mn and vice-versa) changes significantly the number of AF Fe-Mn pairs without changing any Mn-Mn magnetic interaction. It induces rather small energy modifications (less than 10 meV per

Mn), and the sign of the energy variation shows no dependence on the sign of number variation of AF Fe-Mn pairs. However, switching some Mn magnetic moments (changing the number of AF Mn-Mn pairs) generally leads to unstable states. A particular case is noted in Fig. 2.10, the 8-atoms cluster, where two atoms have a very small magnetic moment (0.2 μ_B) which results certainly from magnetic frustrations between several interactions which cannot all be satisfied within the collinear approximation. Since these clusters are small, they can obviously not develop the AFD structure as in the lowest-energy state of pure bcc Mn, because of finite size effects. However, we notice that in the 15-Mn cluster, the ratios of AF 1nn and 2nn interactions are respectively 75% and 33%, which are not too far from the values for pure bcc AFD Mn (respectively 50% and 33%).

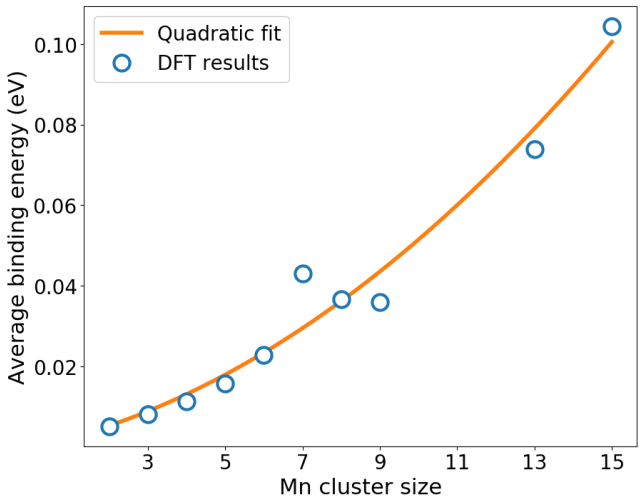

FIGURE 2.11: Average binding energy (per atom) of lowest energy atomic and magnetic configurations of Mn clusters versus the number of Mn atoms composing the cluster, taking the isolated AF-Mn as reference. Positive values indicate an attraction.

Average magnetic moment magnitudes of the two types of Mn atoms forming the clusters: the AF-Mn and the FM-Mn are shown in Fig. 2.12. We note a generally larger moment magnitude for the FM-Mn forming a cluster than isolated. The opposite occurs for the AF-Mn atoms in the case of the smallest clusters. The intermediate sized clusters between 7 and 9 atoms show some particular values, mostly lower than the corresponding Mn moments in the considered clusters. This behavior may be due to a transition between the very small clusters (arranged within a cubic unit cell) in which every Mn atom is an interface atom (mainly surrounded by Fe atoms) and more extended clusters, in which Mn atoms have a lot of Mn nearest neighbors.

Considering the average Mn magnetic moment of a cluster in its lowest energy magnetic configuration, we observe that the magnetic Fe-Mn coupling tendency shows the same trend as in the random solutions, except that the transition point appears at a lower concentration (around 3 at.% Mn in Fig. 2.6). This feature may be one possible explanation of the discrepancy between experimental and theoretical

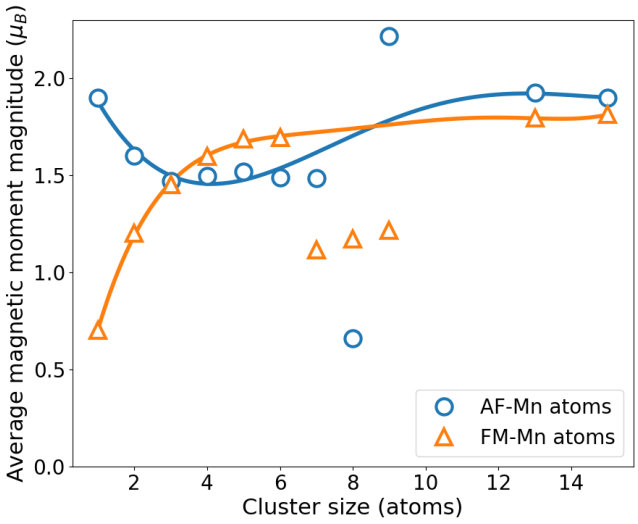

FIGURE 2.12: Average magnetic moment magnitude of Mn atoms coupled AF (respectively FM) with Fe atoms as a function of the number of Mn atoms composing the cluster. Solid lines are polynomials fitted on the data points which follow a general trend (see text), in order to evidence the behavior of the intermediate-size points which deviate from this trend.

data concerning the transition concentration of the average Mn moment behavior, from an AF to a FM state with respect to the Fe moments, in Fe-Mn alloys. Fig. 2.6 shows that clusters resulting average Mn moment is indeed FM at concentrations for which Fe-Mn random solutions exhibit an AF Fe-Mn average magnetic coupling (for Mn concentrations between 3 and 6 at.%). Indeed, the existing discrepancy comes from data based on random solid solutions assumed in theoretical calculations [85, 52, 110], whereas experimental samples may contain Mn clusters in Fe which are more stable systems at low temperatures. Of course, the detailed composition of the experimental samples is strongly related to the thermal treatments such as the speed of quenching [71, 119, 25, 132, 128].

2.4 Mn interaction with vacancies in bcc Fe

Beyond the magnetic and energetic properties of idealized Fe-Mn alloys, another focus of this study is the variation of these properties in the presence of point defects, for instance vacancies. First, we have investigated the effects of a vacancy on a single Mn solute in bcc Fe. To do so, a vacancy was inserted in a 128-sites bcc Fe lattice containing one Mn atom (in either AF-Mn or FM-Mn state), at various distances from the Mn atom, from $1nn$ to $6nn$. The presence of the vacancy increases the energy gap between the two energetic minima of Mn from ΔE = 0.05 eV in the isolated case to ΔE = 0.28 eV for the $1nn$ Mn-vacancy case. This behavior may be qualitatively understood by a local electronic redistribution. The presence of a nearby vacancy induces a depletion of the Mn charge (see Fig. 2.19), which is expected to favor further the AF-Mn state compared to the FM-Mn state. In addition, lattice distortion

considerations can also contribute to rationalize the same behavior, since the FM-Mn has a lower effective volume than the AF-Mn (see section 2.1). We estimated in both cases the lattice distortion energy by replacing both the vacancy and the Mn solute in the relaxed supercell by Fe atoms, without further optimizing the atomic positions. The lattice distortion energy is calculated as the difference between the resulting supercell energy and the energy of a perfect bulk bcc Fe with the same number of atoms. This energy is respectively 0.36 and 0.30 eV for the FM-Mn and AF-Mn case. In comparison, the lattice distortion energy for an AF-Mn and a FM-Mn, without the vacancy is practically the same, differing in only 0.005 eV.

The binding energy between the vacancy and the Mn solute was calculated with the following expression:

$$\begin{aligned} E^{bind}(\text{V-Mn}) = -E^{tot}((n-2)\text{Fe+Mn}+V) \\ +E^{tot}((n-1)\text{Fe+1Mn}) + E^{tot}((n-1)\text{Fe}+V) - E^{tot}(n\text{Fe}) \end{aligned} \tag{2.4}$$

with $E^{tot}(n\text{Fe})$ being the total energy of a pure n-atoms Fe system, $E^{tot}((n-1)\text{Fe}+V)$ the total energy of a n-atoms Fe system with one of the Fe atoms replaced by a vacancy (V), $E^{tot}((n-1)\text{Fe+1Mn})$ the total energy of a n-atoms Fe system with one of the Fe atoms replaced by an AF-Mn atom, and $E^{tot}((n-2)\text{Fe+Mn}+V)$ the total energy of a n-atoms Fe system containing both a Mn atom and a vacancy. As shown in Fig. 2.13, there is a strong attraction between the vacancy and the AF-Mn at a short range (from $1nn$ to $3nn$) which decays to zero at longer distances except for the $5nn$ case. The relatively high value for the $5nn$ case may be due to the fact that, in a bcc lattice, it is actually the second nearest neighbor in the densest (111) direction. This feature is however not observed in the case of FM-Mn, which has a smaller effective volume than Fe. (see section 2.1)

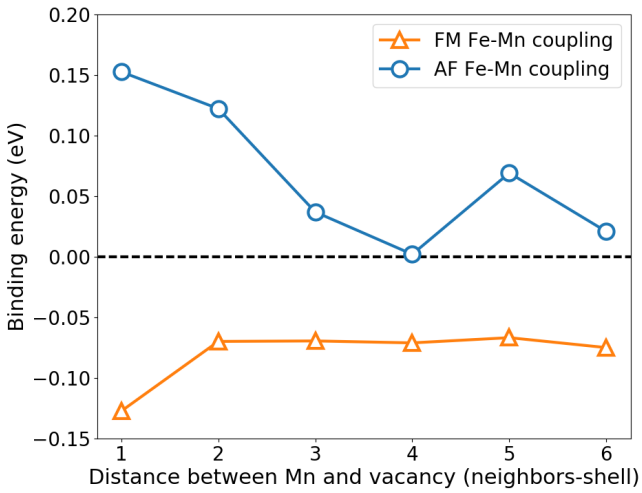

FIGURE 2.13: Binding energy between a vacancy and an isolated Mn solute in bcc Fe as a function of their separation, taking the AF-Mn as reference. Positive values mean attraction.

Mn-Mn dist.	μ_{Mn} (μ_B)	E_{bind}(MnV-Mn)	E_{bind}(Mn-Mn)	E^{tot}_{bind}	E^{pair}_{bind}
1nn	-2.87/-2.29	0.058 (eV)	0.012 (eV)	0.181 (eV)	0.287 (eV)
2nn	-2.63	0.108 (eV)	-0.032 (eV)	0.261 (eV)	0.273 (eV)
3nn	-2.74	0.208 (eV)	-0.044 (eV)	0.361 (eV)	0.261 (eV)
5nn	-2.67	0.171 (eV)	-0.060 (eV)	0.324 (eV)	0.245 (eV)

TABLE 2.3: Magnetic and energetic effects of a vacancy on a Mn dimer. The first column shows the distance between two Mn atoms and the second column shows their magnetic moments in the presence of vacancy. The binding energies between Mn atoms with and without vacancy are given respectively in third and fourth columns. Finally, the total and pairwise binding energies are given respectively in fifth and sixth columns. Pairwise binding energy is calculated as the sum of Mn-Mn and Mn-V binding energies for the two Mn atoms. Lowest energy magnetic states are taken as references for every binding energy calculation.

The insertion of a vacancy has a noticeable impact on the interaction between two Mn solutes in bcc Fe. Our calculations show that when the Mn atoms are surrounding a vacancy, they tend to couple each AF with Fe atoms of the matrix, regardless the distance between those solutes ($2nn$, $3nn$ or $5nn$). As expected, the magnetic moment magnitude of these Mn atoms is significantly increased compared to the corresponding configuration without the vacancy, due to the magneto-volume effect (see Table 2.3). One can also notice that among the atomic configurations considered, two Mn atoms located at the first-neighbor shell of a vacancy prefer to arrange as $3nn$ to each other. The second lowest energy configuration being as $5nn$ to each other, followed by the $2nn$ case which is the worst arrangement in terms of system energy. Although it is shown in Fig. 2.8 that $2nn$ Mn are less repulsive than $3nn$ Mn in their respective lowest energy magnetic configuration, the presence of the vacancy stabilizes the AF-Mn state and thus $2nn$ Mn atoms become more repulsive because they are constrained in a higher energy magnetic configuration.

The binding energy between two Mn atoms was compared with and without the presence of a vacancy as $1nn$ of both Mn atoms. Except in the case of $1nn$ Mn atoms, where the vacancy is inserted as respectively $1nn$ and $2nn$ of the Mn solutes. In all the studied cases, the vacancy either promote or enhance attraction between the Mn atoms (Table 2.3). Also, the comparison between the total binding energy and the pairwise binding energy reveals a synergistic effect in the cases of $3nn$ and $5nn$ Mn dimers. Pairwise binding energy is calculated as the sum of Mn-Mn and Mn-V binding energies for the two Mn atoms. The opposite trend is observed in the cases of $1nn$ and $2nn$ Mn atoms, which is consistent with a magnetic frustration induced by the vacancy stabilizing both Mn atoms as AF-Mn, while Mn-Mn interactions are favoring a different magnetic state (AF-Mn + FM-Mn.)

In order to study the effect of a vacancy on Mn clusters magnetic properties, further calculations were performed with a vacancy in bcc Fe while replacing, atom by atom, its first nearest neighbors by Mn atoms, as shown in Fig. 2.16. For each

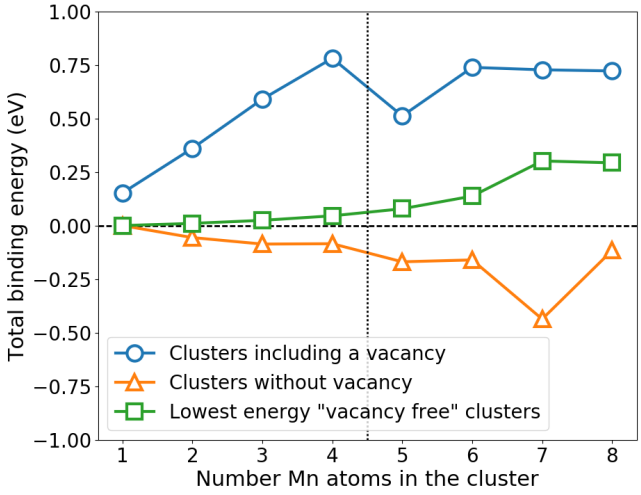

FIGURE 2.14: Comparison of total binding energies of: 1) clusters composed of one vacancy and n-Mn atoms. The corresponding structures are shown in Fig. 2.16. 2) clusters with the same Mn arrangement and the vacant site replaced by a Fe atom, and 3) the lowest-energy n-Mn clusters found. The isolated AF-Mn is taken as reference.

number of Mn atoms, various atomic configurations were studied and for each of them, several magnetic states were considered. More open cluster configurations were also tested, that is, locating some Mn atoms on the $2nn$ shell of the vacancy instead of being $1nn$ of it. The most compact configurations are always found to be the most energetically favorable.

The first observation is that the vacancy tends to stabilize the AF coupling of Mn atoms with Fe atoms of the matrix. Indeed, every atomic configuration tends to exhibit a full AF Fe-Mn coupling while corresponding vacancy-free clusters show more complex spin configurations (see section 2.2).

Two complementary effects may explain this observation. As previously shown in the case of a single Mn atom, the vacancy tends to stabilize the AF-Mn state. It also acts as a magnetic screener reducing the impact of the Mn-Mn interactions described in section 2.3. Such a behavior is also observed in the case of Cr atoms near a vacancy in bcc Fe [102])

The total binding energy between the vacancy and every Mn atom of the cluster is calculated for the lowest energy atomic and magnetic configuration found for each number of Mn atoms, using the following formula:

$$\begin{aligned} E^{bind}(V-p\text{Mn}) = -E^{tot}((n-p-1)\text{Fe}+p\text{Mn}+V) \\ +pE^{tot}((n-1)\text{Fe+Mn})+E^{tot}((n-1)\text{Fe}+V)-pE^{tot}(n\text{Fe}) \end{aligned} \tag{2.5}$$

with $E^{tot}(n\text{Fe})$ being the total energy of a pure n-Fe bcc bulk, $E^{tot}((n-1)\text{Fe}+V)$ the total energy of n-Fe system with one of the Fe atoms replaced by a vacancy,

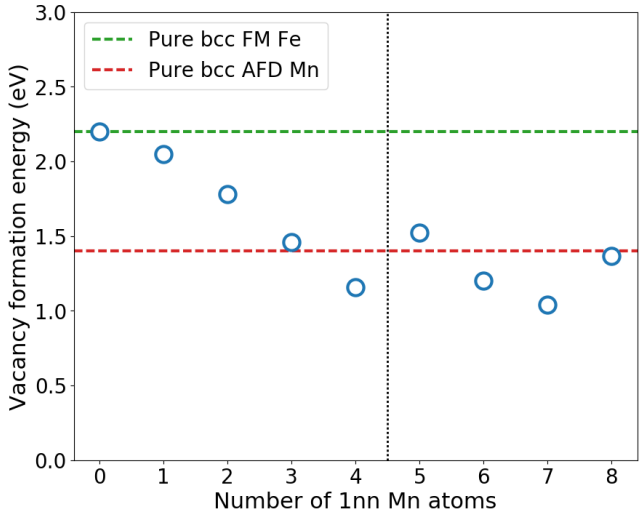

FIGURE 2.15: Vacancy formation energy as a function of the number of Mn atoms on its first-neighbor shell.

$E^{tot}((n-1)\text{Fe+Mn})$ the total energy of a n-Fe system with one of the Fe atoms replaced by a Mn atom, and $E^{tot}((n-p-1)\text{Fe}+p\text{Mn}+V)$ the total energy of a system containing p Mn atoms and a vacancy.

The results shown in Fig. 2.14 reveal that the total binding energy is positive and increases with the number of Mn atoms up to 4 Mn. Then it reaches a plateau and the binding energy remains constant between 6 and 8 Mn cases. We note a rather small value for the 5-Mn case. It can be explained as follows: Up to 4 Mn atoms on the $1nn$ shell of the vacancy, the lowest-energy atomic configuration is such as the Mn atoms are $3nn$ to each other (the most favorable state for two Mn atoms, see Fig. 2.16). From the fifth Mn atom introduced to the $1nn$ shell, such arrangement is no more possible and some Mn atoms have to be as $2nn$, which has a higher energy as seen in the case of a Mn dimer around a vacancy.

Another relevant feature is that the binding energy is much higher than in the corresponding vacancy-free Mn clusters, which indicates an enhancement of Mn clustering due to the presence of vacancies, as also noticed in Fe-Cr alloys [102]. This behavior may be relevant in Fe-Mn systems under some extreme conditions with creation of large amounts of vacancies.

The vacancy formation energy was also evaluated as a function of the number of Mn atoms at the $1nn$ shell of the vacancy. Fig. 2.15 shows that the vacancy formation energy decreases almost linearly with the number of Mn atoms up to 4 Mn atoms, then, it oscillates around the value found in the pure bcc AFD-Mn bulk. This decreasing trend suggests that the vacancy formation is more favorable in a Mn-rich than in a Fe-rich local environment in Fe-Mn alloys. In addition, similarly to the bcc Fe-Cu alloys [152], the mobility of Mn clusters may be significantly enhanced due to the preference of vacancies to be located around a Mn cluster than in the Fe matrix, dictated by the difference of respective vacancy formation energies.

The present study is limited to the case of Mn atoms around a single vacancy. The

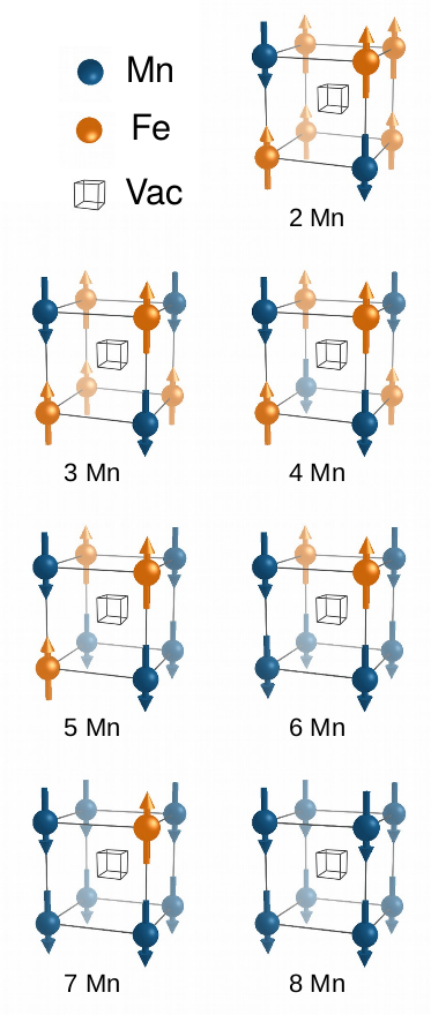

FIGURE 2.16: Schematic representation of the lowest energy atomic and magnetic configuration of Mn clusters in bcc Fe composed of a vacancy surrounded by n Mn atoms.

effects of multiple vacancies may also be relevant, especially for the understanding of the Fe-Mn alloys under extreme conditions such as plastic deformation or irradiation. It is however beyond the scope of this chapter.

2.5 Interstitial impurities and Mn in bcc Fe

Carbon, nitrogen and oxygen atoms, neighbors in the Periodic Table of Elements, are highly common interstitial impurities in iron-based alloys. It is thus important to understand the interaction between these elements and Mn solutes in bcc Fe, in order to clarify the impact of these interstitial atoms on magnetic properties of Mn solutes.

In this study, we only consider the effect of a single interstitial atom, located at the lowest energy octahedral site[10], near a Mn atom. We first evaluated the interaction energy between a single Mn solute and a foreign interstitial atom (FIA = C, N or O), at a $1nn$ distance. The binding energy between the $1nn$ FIA and the Mn solute

in the lowest-energy magnetic configuration is attractive in the three cases (0.08 eV for C; 0.21 eV for N and 0.24 for O). Interestingly, in the case of C and N atoms, the Mn magnetic moment tends to be parallel to the Fe moments (opposite to the case of isolated Mn solutes), whereas in the case of an O atom, Mn moment tends to be antiparallel to the Fe moments, as shown in Fig. 2.17. The results for the case of C are in good agreement with a previous DFT study, on both Mn-C binding energy and Mn magnetic moment.[105, 97]

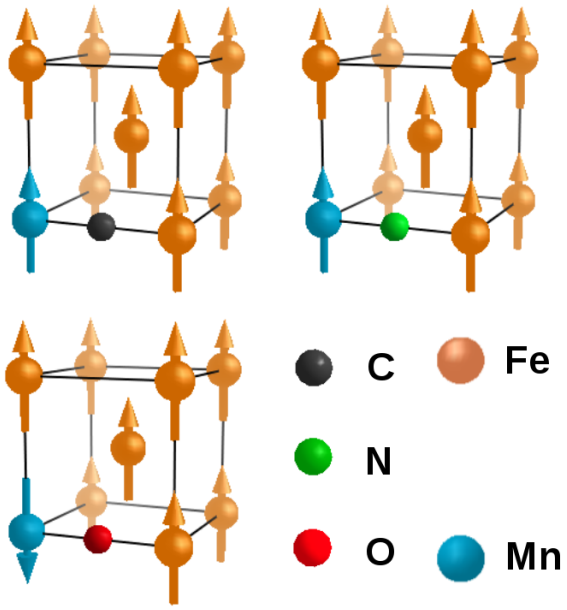

FIGURE 2.17: Schematic representation of the lowest energy magnetic configuration of a Mn atom in bcc Fe, with a X interstitial at its $1nn$ octahedral site (X=C,N,O).

Projected densities of states shown in Fig. 2.18 reveal a strong hybridization between the *p*-shell of C atom and the *d*-shell of Mn. As expected, with increasing *p*-band filling of the FIAs, such hybridization is weaker in the case of the N interstitial and negligible in the case of the O interstitial. The right panel of the same figure shows differential charge density maps obtained by subtracting the charge density of the isolated C, N or O atom and the Fe-Mn system without interstitial defect, to the same Fe-Mn fully relaxed system containing the FIA. Note that the atomic positions are kept identical for the substractions. The charge maps show that, as expected, C exhibits a covalent bond with the Mn atom, increasing the local charge density around the Mn atom whereas the charge density around the O impurity remains very localized, which explains that O has no noticeable effect on the magnetic coupling of the Mn atom. The N interstitial shows an intermediate behavior. As stated in introduction and in section 2.1, the magnetic state of Mn is especially flexible in bcc iron, reflected for instance by the presence of two minima (AF-Mn and FM-Mn) for the single solute. In order to adapt to different local environments, such

as in the Mn dimer, the solute may easily change its preferred magnetic state. In the case of a Mn solute next to a C or a N interstitial, the interstitial atom induces a p-d hybridization which strongly increases the local charge density around the Mn atom (Fig. 2.18), and leads to a significant change in the PDOS of the Mn atom. Both up- and down-spin states approach those of the isolated FM-Mn PDOS (Fig. 2.2). For example, the up-spin PDOS of an isolated AF-Mn atom (without the interstitial) shows a sharp peak just above the Fermi level, which is shifted down toward the Fermi level when the local charge increases (with the interstitial). Then, in order to reduce the density at the Fermi level, the peak becomes splitted. As a consequence, the Mn magnetic state switches to the FM-Mn energy minimum, which has a higher local charge density.

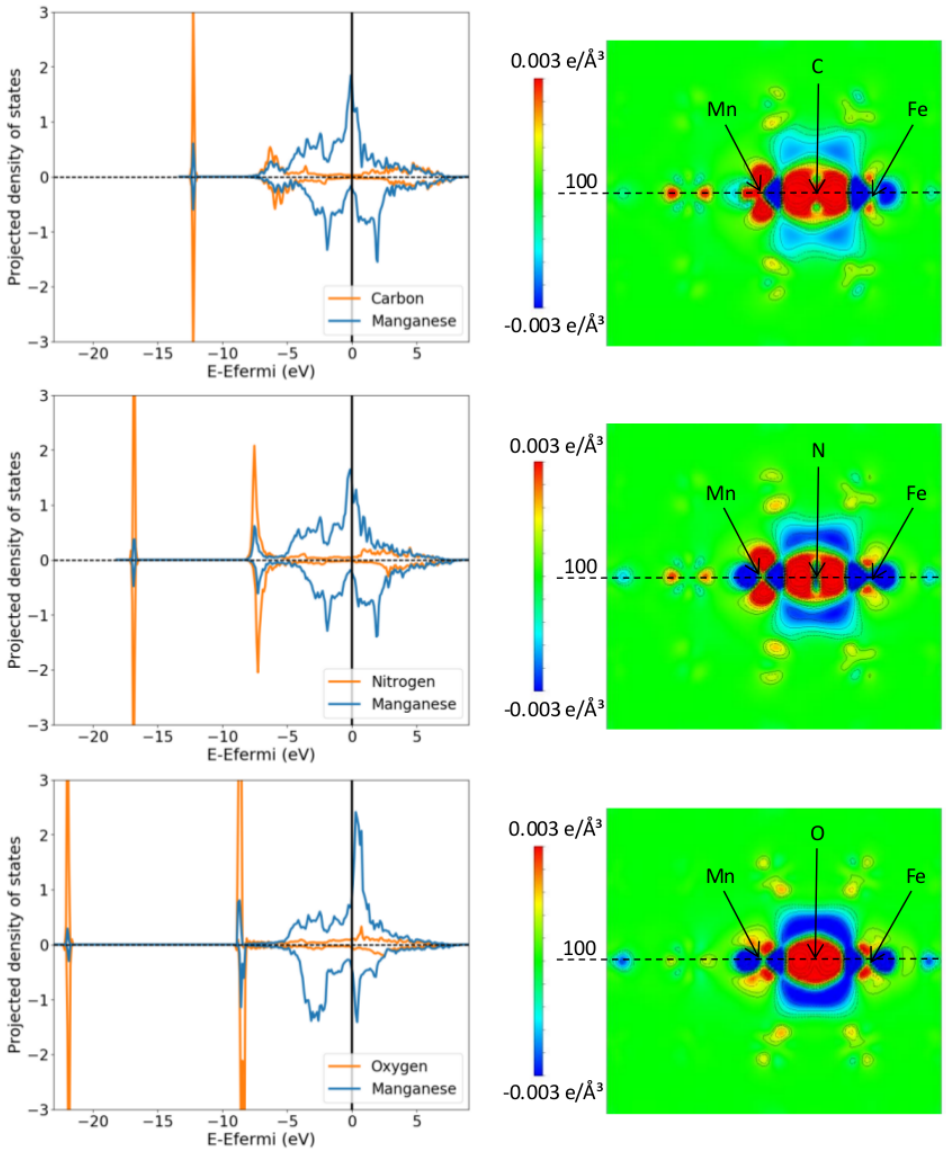

FIGURE 2.18: Projected density of states on Mn atom and X impurity, X being C, N or O (left), and the corresponding differential charge density maps (right). Further details are given in the text.

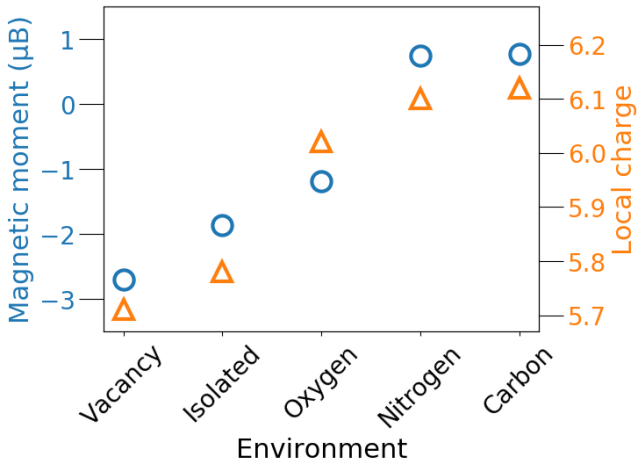

FIGURE 2.19: Correlation between local magnetic moment (triangles) on a Mn atom and its local charge density (circles) for various chemical environments: isolated in Fe, 1*nn* of a vacancy, and 1*nn* of a X interstitial (X = C, N, O).

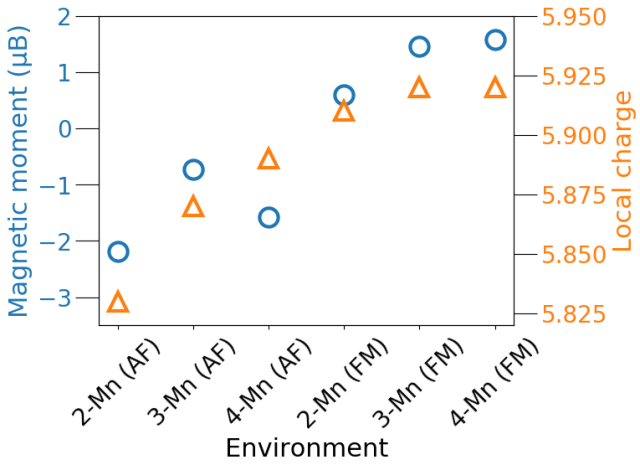

FIGURE 2.20: Correlation between local magnetic moment (triangles) on Mn and the corresponding local charge density (circles). Each moment or charge value results from an average over all the Mn atoms showing the same spin orientation in a *n*-Mn cluster. For example "4-Mn (FM)" in the x-axis means Mn atoms in a 4-Mn cluster, showing a FM interaction with Fe atoms.

The impact of the FIAs on the magnetic state of a Mn solute is rather short ranged. If the FIA is inserted in the 2*nn* octahedral site of a Mn atom, the magnetic moment of the Mn atom remains antiparallel to the lattice Fe moments, the impurity being C, N or O. In this case, the Mn-FIA binding energy is -0.20 eV in the case of C, -0.11 eV for N and 0.04 for O. Clearly, the hierarchy of these energies follows the same trend as for the 1*nn* interactions. Here too, the results in the case of C are consistent with the literature [97].

Due to the expected lattice distortion induced by the interstitial atoms, all the presented results are also verified by complementary fully relaxed calculations. We checked that the relevant results present only minor changes compared to the constant-volume results: variations are in any case lower than 0.01 μ_B for the magnetic moment and lower than 10 meV for the binding energy.

Based on the results presented in previous sections, a correlation can be identified between the magnetic moment of a single Mn solute in bcc Fe and its local charge density. Indeed, the presence of a vacancy, inducing a local charge decrease, tends to favor the AF Fe-Mn magnetic coupling while the presence of an interstitial impurity (particularly the C) may favor the FM Fe-Mn coupling. This trend is illustrated in Fig. 2.19 where the magnetic moment and the local charge of the Mn solute are plotted for various local environments. Both local charge and magnetic moment are obtained by integrating the Mn PDOS, although the absolute values may depend on the integration criterion chosen, the relative values show a clear trend.

In the case of Mn clusters, the Mn-Mn interactions being dominant over the Fe-Mn interactions, this trend is not general. However, for the Mn dimer and the smallest sizes of clusters (up to 4 Mn atoms), the local charge of an AF-Mn is still lower than the charge of a FM-Mn, as shown in Fig. 2.20. Indeed, Mn atoms in these small clusters have a majority of Fe neighbors.

2.6 Conclusions

Density functional theory calculations are applied to investigate magnetic and energetic properties of Mn in bcc Fe-Mn alloys, as functions of the alloy concentration and local chemical environment. Manganese, with a half-filled 3*d* band, exhibits an atypical and complex magnetic behavior.

For the simplest case of an isolated Mn in bcc Fe, we confirm the presence of two collinear energy minima, with the Mn magnetic moment either parallel or antiparallel to the Fe moments, named respectively the FM-Mn and the AF-Mn state. The latter being the ground state. Interestingly, the preference of the Fe-Mn magnetic interaction is highly sensitive to minor changes of the Mn local environment, due to the presence of a high Mn majority-spin electronic density around the Fermi level.

A direct correlation is identified between the local electronic charge and the local magnetic moment on a Mn solute, being isolated or forming a small n-Mn cluster (n = 2 to 4). For instance, the presence of a vacancy near the Mn atom, inducing

a local charge depletion, tends to favor the anti-ferromagnetic Fe-Mn interaction. Also, common interstitial impurities (C, N, and O) present an attraction with a Mn atom if located at its 1nn site. C and N show a strong electronic hybridization with Mn and stabilize the FM-Mn state. At variance, an oxygen atom, with a rather ionic Mn-O interaction and therefore a very localized charge distribution, does not modify the magnetic ground state of an isolated Mn.

Properties of small n-Mn clusters (n = 2 to 15) in dilute Fe-Mn systems are analyzed. Clustering is found to be energetically favorable, consistently with the unmixing tendency found for the bcc Fe-Mn alloys. Various collinear and non-collinear magnetic minima are found for the Mn dimer, which are rather close in energy. It is relevant to point out that our results suggest a dominance of Mn-Mn magnetic interactions over the Fe-Mn interactions, both exhibiting an anti-ferromagnetic tendency, especially for the 1nn and 2nn distances. This behavior is opposite to the Fe-Cr alloy case, where Fe-Cr AF interactions prevail over the Cr-Cr anti-ferromagnetism. A vacancy is found to further stabilize the Mn clusters, by increasing the clusters binding energies. Reciprocally, the formation energy of a vacancy becomes smaller in a Mn-rich than in a Fe-rich local environment. This behavior may promote a rather fast diffusion of Mn nano-clusters, similar to the case of bcc Fe-Cu alloys.

Locally random (SQS) Fe-Mn solid solutions are systematically investigated for a large range of Mn concentrations. Consistently with experimental findings, the average magnetic moment of the alloys decreases linearly with increasing Mn content. In addition, the average Mn moment tends to be antiparallel (resp. parallel) to lattice Fe moments for Mn concentrations smaller (resp. larger) than approximately 6 at.% Mn. It is not clear whether the same trend is observed experimentally or not as there are very few experimental data at low Mn concentrations (less than 2 at.% Mn), which do not agree with each others. However, at concentrations higher than 2 at.%, experimental works all agree on the fact that the Mn moment tends to be parallel to Fe. Various possible reasons for this discrepancy are discussed. In particular, the calculated transition concentration is lowered to approximately 2 at.% Mn if considering clusters instead of random solutions.

Chapter 3

Effective interaction model for bcc Fe-Mn at finite temperatures

---

In this chapter, we parameterize an effective interaction model with ab-initio data in order to simulate, via atomic Monte Carlo simulations, the evolution of magnetic and atomic configurations and their coupling. Some applications of this model are presented, examining certain finite temperature properties of these systems.

In the previous chapter, various results are presented concerning the interplay between the chemical and the magnetic properties in Fe-Mn alloys at electronic ground-state via DFT. As suggested in the literature, thermodynamical and diffusion properties of Fe-based alloys may be strongly influenced by magnetism. For instance, previous studies have shown that magnetism in Fe-Cr alloys has a crucial impact on various thermodynamic and kinetic properties [134, 146]. Such behaviors remain poorly understood for Fe-Mn systems, although it is known that pure bulk Mn shows a complex magneto-structural phase diagram [63, 55] and that there is a strong magneto-elastic coupling in Fe-Mn alloys [118].

This work is mainly focused on the Fe-rich part of the alloys. Indeed, as can be seen in the Calphad phase diagram of Fig. 3.1, the stability domain of bcc Fe-Mn alloys is limited to the dilute alloys (at most 5 at. % Mn).

Up to now, two distinct approaches have been employed in the study of magnetic alloys at finite temperature. On one hand, the disordered local moment (DLM) approach [2, 3, 135] mostly combined with Coherent Potential Approximation (CPA) calculations allow to describe alloys with both chemical and magnetic random structures. It consists in modeling paramagnetic systems by fully random spin configurations, with a negligible correlation between the spins. Such approach offers a good representation of asymptotically high temperatures.

On the other hand, the magnetic cluster expansion (MCE) approach, based upon the parameterization of effective interaction models has also shown interesting results for the study of magnetic alloys. Namely, Pierron-Bohnes *et al.* have used such approach in an early study on Fe-Co alloys [130] and Lavrentiev *et al.* later applied

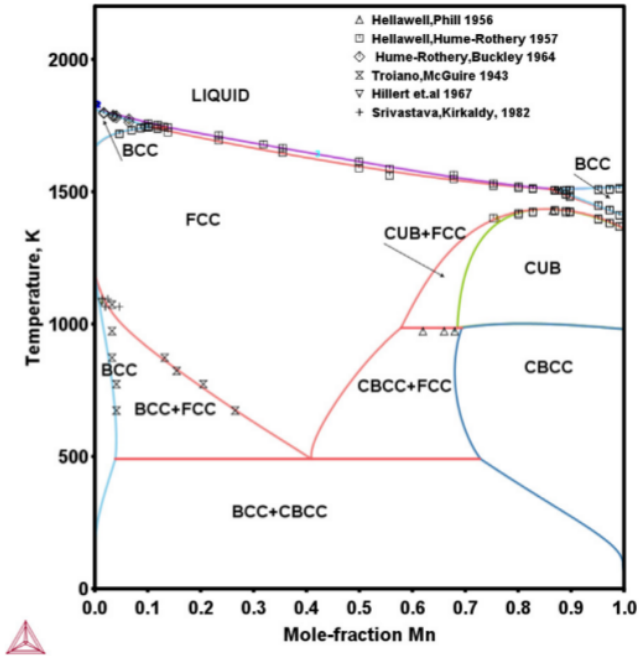

FIGURE 3.1: Calphad Fe-Mn phase diagram generated by Bigdeli *et al.* [14]

this approach to the study of Fe-Ni [89], Fe-Cr [87] and Fe-Ni-Cr [90] alloys. Although such models have shown satisfactory results concerning the prediction of alloys magnetic properties, most of these studies are performed with fixed atomic structures, while only the magnetic structure evolves. More recently, Chapman *et al.* [21] have incorporated the MCE expressions developed by Lavrentiev *et al.* in spin-lattice dynamics simulations for Fe-Cr alloys.

In order to study the interplay between magnetism and thermodynamic properties, we propose to develop such an effective interaction model for Fe-Mn systems, fitted on ab-initio results. Our objective is to perform Monte Carlo simulations on atomic exchanges and spin-relaxations on-the-fly in order to simulate the possible interplay between the chemical and magnetic structures.

In this approach, the complete Hamiltonian of the system has the following expression:

$$H = \sum_{i}^{N} A_i M_i^2 + B_i M_i^4 + \sum_{i}^{N} \sum_{n}^{P} \sum_{j}^{Z} J_{ij}^{(n)} \mathbf{M}_i \cdot \mathbf{M}_j + \sum_{i}^{N} \sum_{n}^{P} \sum_{j}^{Z} V_{ij}^{(n)} \tag{3.1}$$

where P is the maximum range of interactions in terms of neighbor shells, Z is the number of neighbors of each interaction range, $\mathbf{M}_i$ is the magnetic moment of the ith atom, M_i is its magnitude and $V_{ij}^{(n)}$ represents the chemical pair-interaction between species of atoms i and j, at range n. A_i and B_i are the magnetic on-site terms of the i-th atom.

Using this formalism, it is possible to model separately the magnetic evolution via spin relaxations and the chemical evolution via pair atomic exchanges, both

ruled by a Metropolis criterion.

In this chapter, the studied systems are considered without defects. The simulation of defect-free alloys represents a first-step to the study of more complex systems, for instance including vacancies or even extended defects such as interfaces and dislocations.

The first section of the chapter is dedicated to the parameterization of the model, which is not trivial as the Mn magnetic properties induce severe complexities. Then the obtained model is applied in the following sections to the prediction of various temperature dependent properties that cannot be accessed directly from DFT calculations. As much as possible, the agreement with experimental or Calphad results is discussed.

3.0 Parameterization and validity of the model

Considering the Hamiltonian presented in equation 3.1, many parameters have to be determined. From the DFT data generated for the study of chapter 2, a linear least-square regression of all the parameters at once was attempted, using all the available data. This first brute-force approach led to a non-reasonable set of parameters, unable to predict correctly any property of Fe-Mn alloys. This dead-end is not surprising as there are quite complex physical phenomena at stake. Fitting this way a satisfactory model capturing all these phenomena would require a huge amount of configurations (this model requires to fit 30 parameters and our present dataset contains approximately one hundred systems (128 to 250 atoms large) with various atomic and magnetic configurations).

Instead, we chose to perform a more subtle and progressive parameterization methodology which also allows to select the most physically accurate parameterization among the various mathematical solutions that can be found with the present dataset. It consists in fitting in a first time the magnetic parameters of pure Fe and pure Mn on the respective bulk magnetic properties and then in a second step to fit Fe-Mn magnetic interactions progressively, on key physical properties which arise from DFT calculations. This is a heavily back-and-forth iterative process. After each adjustment to a new property, it is necessary to ensure that other properties - previously well predicted - are still correct. In order to fit these magnetic parameters, we calculate the energy difference between systems with identical atomic configurations but distinct magnetic states. It allows to attribute the whole energy difference to the variation of the magnetic state, disregarding the atomic configuration. Finally, once the whole magnetic contribution of the Hamiltonian is satisfactory, the non-magnetic parameters (associated to chemical binding) are fitted on the DFT predicted mixing-energy.

Please note that the numerical values of the parameters described in this section are given in Appendix.

3.0.1 Magnetic parameters for pure bcc Fe

Pure Fe magnetic parameters are fitted up to the fifth nearest-neighbor range with the following principle: DFT calculations are performed on pure Fe systems (4x4x4 supercells, 128 atoms) with various magnetic state, including ferromagnetic (FM), antiferromagnetic (AF), double-layer antiferromagnetic (AFD), quadruple-layer antiferromagnetic (AFQ), non-magnetic (NM) and also a dozen of paramagnetic (PM) systems modeled with locally disordered collinear magnetic random structures. We note that for magnetically ordered structures, the calculations are done with the corresponding equilibrium lattice constant. For the magnetically disordered structures, the FM equilibrium a_0 was conserved, while checking that residual pressure remains lower than 10 $kbar$.

The parameters of the model are fitted by performing a least square regression on the difference of magnetic interactions between two systems, along with the total energy difference between these two systems.

We note that in the case of Fe atoms (in pure bcc Fe and bcc Fe-Mn alloys), the self-magnetism induces a very stiff magnetic moment magnitude, which suggest that the classical Heisenberg hamiltonian may be adequate. However, as it is not the case the magnetic moment magnitude of Mn in bcc Fe-Mn alloys (see Fig. 2.5 in chapter 2), we include spin longitudinal fluctuations in the pure Fe model in order to have a consistent formalism.

The fitting procedure just described provided a set of parameters in which the nearest-neighbor interaction J^1_{Fe} and J^2_{Fe} have opposed signs (i.e. are competing). Although it is in agreement with a previous early study [95], it is not with most others [127, 38, 6, 161, 157, 87, 89]. In order to be consistent with the existing literature, we imposed J^1_{Fe} and J^2_{Fe} to have the same sign and restarted the fitting procedure. We note that longer range interactions (from $3nn$) are almost negligible.

Fig. 3.2 shows the model prediction of the energy difference between the ground-state and various ordered magnetic states of pure bcc Fe, using DFT magnetic configurations as input. The comparison with DFT results shows that the energy hierarchy of the various ordered magnetic states is well represented.

With the magnetic parameters obtained, it is possible to perform rigid-lattice Monte Carlo simulations on pure Fe. Indeed, the atomic configuration being constant (pure Fe), no other parameter is needed here.

Spin Monte Carlo simulations on pure Fe give access to several properties, which are used to control the validity of the approach. We performed spin-MC simulations on a 16000 atoms system (20x20x20 bcc unit cells) using $5 \cdot 10^8$ spin relaxation attempts. We note that for such simulations, the convergence is reached in most temperature regimes after approximately 10^6 steps but the convergence is much more difficult to reach around T_C, where approximately 10^8 steps are necessary. We add $4 \cdot 10^8$ MC-steps after convergence for data collection. The convergence is ensured by initializing each simulation in both ferromagnetic and paramagnetic states and by verifying that both initializations lead to the same results.

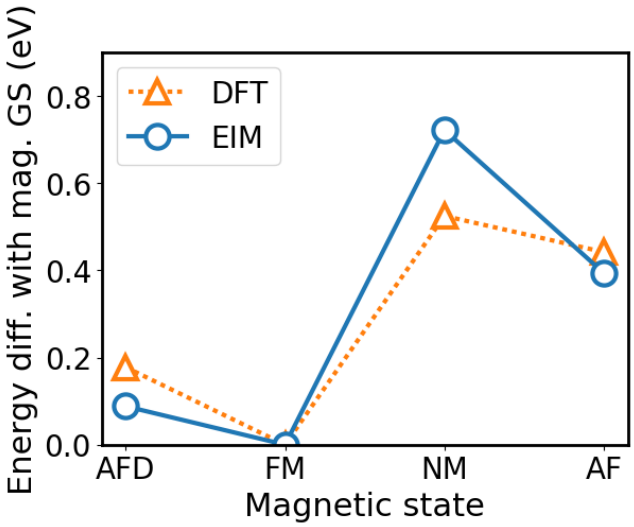

FIGURE 3.2: Model predictions of the energy differences between ordered magnetic states of bcc Fe compared to DFT results

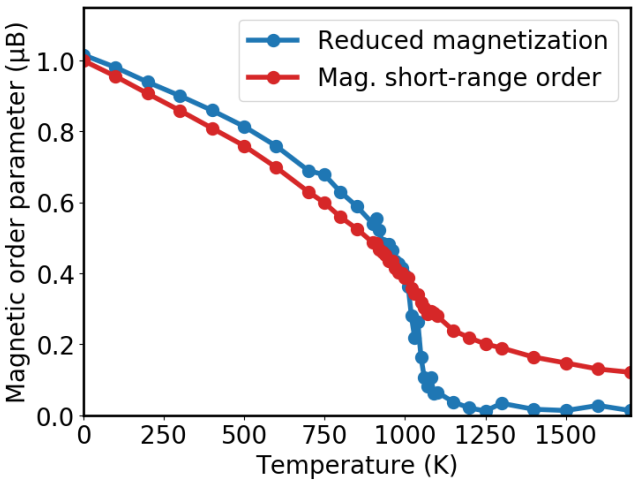

FIGURE 3.3: Temperature evolution of the reduced magnetization and the 1*nn* magnetic short-range order in pure bcc Fe.

The reduced magnetization of pure Fe is shown in Fig. 3.3. It is obtained by averaging the magnetic moments over the whole system and by normalizing by the average magnitude of the magnetic moments. As expected, the reduced magnetization equals to 1 at the low temperature limit (as the ground-state of bcc Fe is ferromagnetic) and tends to 0 at high temperature (as Fe is paramagnetic at the high temperature limit). [8].

The Curie temperature may be obtained from Fig. 3.3 as the inflexion point of the second order transition which is observed on the magnetization curve.

Simulations of the temperature dependence of the bulk magnetization with these parameters first underestimated the Curie temperature (approximately 800K compared to 1044K experimentally [73]). As one of our main purposes is to study the interplay between magnetic and thermodynamic properties, it was necessary to properly predict the Curie temperature. Hence, the parameters were slightly adjusted in order to obtain a closer prediction of T_C in pure Fe. We note that the value of T_C is very sensitive to the parameters, compared to the energetics at 0K which are not disturbed by such slight adjustments. The resulting T_C is approximately 1060K, the agreement with the experimental value (1044K) is not surprising as experimental T_C was explicitly used for the fitting of the model.

The $1nn$ magnetic short-range order (MSRO), defined here as nearest-neighbor spin pair-correlation function is also shown in Fig. 3.3. As can be noticed, in the low temperature domain (below T_C) it decreases with temperature slightly faster than the magnetization. On the opposite, at high temperature (beyond T_C), MSRO remain significant while M converges to 0 almost directly beyond T_C. These significant differences between the two curves suggest that the study of intermediary temperatures (typically in the range of T_C) may require to take into account the local magnetic order. We note that we have observed similar differences between the magnetization and the magnetic short-range order using Ising and Heisenberg models.

As shown in the upper panel of Fig. 3.4, the average magnitude of Fe magnetic moments decreases with temperature up to the Curie temperature. When $T > T_C$, the average magnitude increases very slightly with temperature. This curve is in good agreement with the results of Lavrentiev *et al.* [87] obtained with a similar approach. However, please note that these variations of the average magnitude are very small (contained within 0.1 μ_B) which suggests that the classical Heisenberg model is a good approximation for pure Fe.

The temperature evolution of the magnitude distribution, shown in the bottom panel of Fig. 3.4, is in good agreement with a study of Ruban *et al.* [134], performed with a similar approach.

As Monte Carlo simulations give access to the system total energy as a function of temperature (more precisely its magnetic contribution, with the present model), it is possible to determine the magnetic contribution of the heat capacity of the system. Please note that as we are working on rigid lattice, $C_p(T) = C_v(T)$. The heat capacity

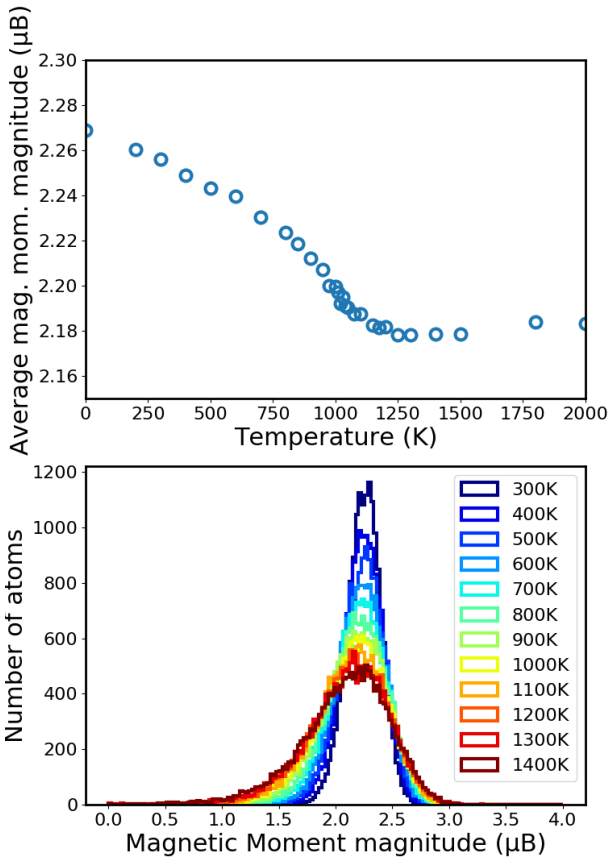

FIGURE 3.4: (top) Temperature evolution of the average magnetic moment magnitude of Fe atoms. (bottom) Distribution of the magnetic moment magnitude of Fe atoms for various temperatures.

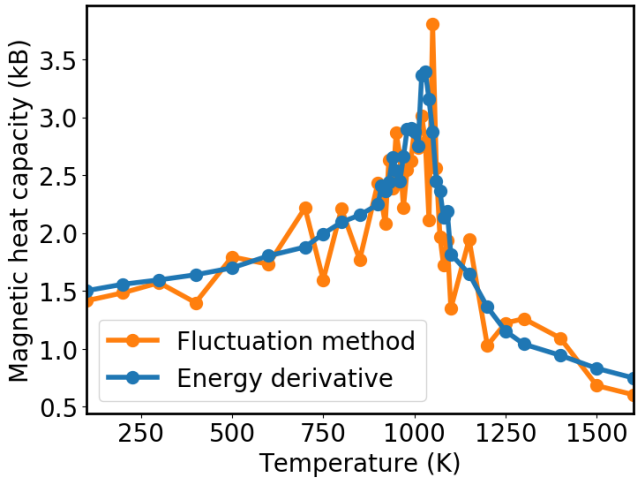

FIGURE 3.5: Temperature evolution of the magnetic heat capacity, obtained via both fluctuation and derivative methods.

can be calculated from our simulations via two distinct methods. On the one hand, C_p^{mag} is related to the mean square fluctuations of the internal energy, calculated using the following expression [87]:

$$C_p^{mag}(T) = \frac{< E^2 > - < E >^2}{k_B T^2} \tag{3.2}$$

By energy fluctuation is meant the variations of the energy with respect to Monte Carlo steps. We note that the data collection only starts after convergence of the energy of the system.

One the other hand, C_p^{mag} can also be calculated by derivating the internal energy over temperature by a finite-difference method with a typical temperature interval of 10K near T_C (between 950 and 1150K) and of 100K far from the Curie temperature.

$$C_p^{mag}(T) = \frac{\partial E}{\partial T} \tag{3.3}$$

As shown in Fig. 3.5, both methods lead to similar results. However, in our case the fluctuation method exhibits much more noise than the direct derivative method. The presence of a peak at T_C is in agreement with previous experimental and calphad studies of the literature [168, 4, 30, 165, 166, 11, 23] but the overall shape of the curve is quite different from what is observed in experiments and calphad calculations. Especially, it can be noticed that the heat capacity doesn't converge to 0 at the low temperature limit. This is a huge conceptual issue and if one attempt to calculate the magnetic entropy using the expression in eq. 3.4, the result diverges at low temperature limit, which is absolutely not physical.

$$S^{mag}(T_X) = \int_0^{T_X} \frac{C_p^{mag}(T)}{T} dT \tag{3.4}$$

As explained in the method chapter (section 1.2.7), this inconsistency is caused by the use of the Boltzmann distribution in the Metropolis algorithm of the spin Monte Carlo simulations (using the scaling factor $\eta = k_B T$). Switching from classical to quantum statistics (using the Bose-Einstein distribution) can be done by replacing the scaling factor η with the following expression [179]:

$$\eta(T) = \int_0^{E_C} \frac{E}{\exp(E/k_B T) - 1} \cdot g(E,T) dE \tag{3.5}$$

where E is the energy of a magnon at a wavevector $\mathbf{q}$, $g(E,T)$ is the magnons density of states (mDOS) at temperature T and magnon energy E. E_C is the highest energy that gives contribution to the magnon density of states. As arises from equation 3.5, the corner-stone of this quantum correction is the knowledge of the mDOS. The approach of Bergqvist *et al.* [12], which consists in determining the 0K mDOS and extrapolating the temperature evolution of $\eta(T)$. The dynamical equation for

the spin system, expressed as follows [180]:

$$\hbar\omega = \sum_{i\neq 0} J(|\mathbf{R_0} - \mathbf{R_i}|)(1 - e^{i\mathbf{k}\cdot(\mathbf{R_0}-\mathbf{R_i})}) \tag{3.6}$$

is solved analytically, using the J_{ij} magnetic interaction parameters of our model. Only considering the $1nn$ and $2nn$ exchange coupling parameters, we solve:

$$\begin{aligned} E = 8J_1 \left[1 - cos(\frac{ak_x}{2})cos(\frac{ak_y}{2})cos(\frac{ak_z}{2})\right] \\ +2J_2(1 - cos(ak_x)) + 2J_2(1 - cos(ak_y)) + 2J_2(1 - cos(ak_z)) \end{aligned} \tag{3.7}$$

where a is the lattice constant. The energy $E(k)$ of a magnon at wavevector k is calculated all along the high-symmetry path Γ-H-P-Γ-N-P-N-H of the Brillouin Zone, as illustrated in green in Fig. 3.6. The obtained magnon dispersion relation is in good agreement with other literature studies [114, 54, 180], although the frequency of the peaks is very sensitive to the parameterization. The mDOS shown in panel C of Fig. 3.6 is then obtained by integrating the dispersion curve.

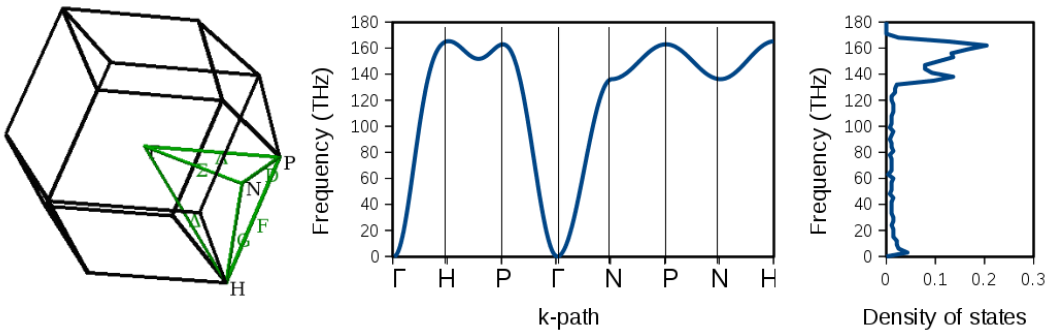

FIGURE 3.6: (a) Schematic representation of the considered high-symmetry path (green) used to sample the Brillouin Zone. (b) The magnon relation dispersion obtained along the k-path. (c) The mDOS obtained from integration of the dispersion curve.

Finally, in order to obtain the temperature dependent mDOS, we apply the quasi-harmonic approximation as explained in the work of Woo *et al.* [179]. The temperature dependent mDOS is calculated by re-scaling the upper limit of the integral (eg. the highest energy that contributes to the mDOS) in eq. 3.5. This cut-off energy is expressed as follows [12]:

$$E_C(T) = E_C(0) \cdot \left(1 - \frac{T}{T_C}\right)^{\beta} \tag{3.8}$$

where $\beta \approx 0.375$ is the critical exponent of the magnetization using a 3D Heisenberg model [12].

Applying this methodology, we observe that the resulting scaling factor does not converge to $k_B T$ when approaching the Curie temperature, as shown in Fig. 3.7. This unphysical discontinuity is due to the approximation which consists in re-scaling the

ground-state mDOS upon temperature without allowing its shape to change, which limits the validity of this approximation at low temperatures [12, 179].

In order to overcome this issue, we fitted a fourth degree polynomial in order to interpolate the low temperature QHA scaling factor with the high temperature classical scaling factor. This interpolation is shown in Fig. 3.7.

Although this is a rough way to obtain a reasonable Bose-Einstein scaling factor, we verified with various distinct interpolations that the resulting scaling factor provides comparable magnetization curves.

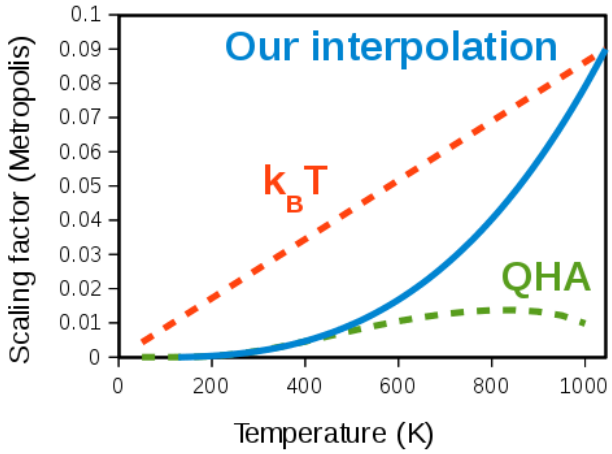

FIGURE 3.7: Temperature dependence of the scaling factor η. The red dashed line shows the classical statistics. The green dashed line shows the scaling factor obtained with the quasi-harmonic approximation as explained in the text. The blue line shows our interpolation which follows the QHA at low temperature and smoothly reverses to classical statistics at T_C.

The Bose-Einstein factor is included in the Monte Carlo simulations by re-scaling the spin temperature in the Metropolis algorithm (only for the spin Monte Carlo) using the interpolated polynomial function shown in blue in Fig. 3.7.

As shown in Fig. 3.8, the use of the Bose-Einstein distribution instead of the Boltzmann distribution leads to a significant difference of magnetization at temperatures below T_C. As can be noticed, the decrease of the magnetization with temperature is negligible up to roughly $T_C/2$ and drops quickly between $T_C/2$ and T_C. This result is in agreement with the literature [12]

The consideration of quantum statistics also has a significant impact on the temperature dependence of the heat capacity. As shown in Fig. 3.9, the heat capacity converges to 0 (compared to $3k_B/2$ with classical statistics) which is in good agreement with previous experimental and calphad studies [168, 4, 30, 165, 166, 11, 23]. We note that the peak at T_C is almost thrice higher than using classical statistics, and that the total area below the curve is equal independently of the distribution.

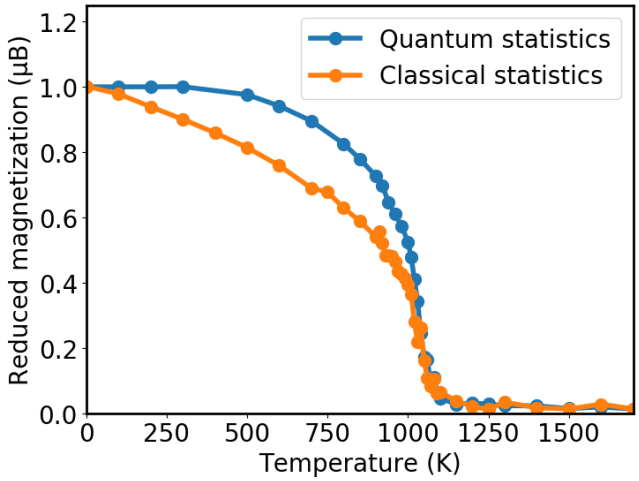

FIGURE 3.8: Temperature evolution of the reduced magnetization of pure bcc Fe using classical and quantum statistics.

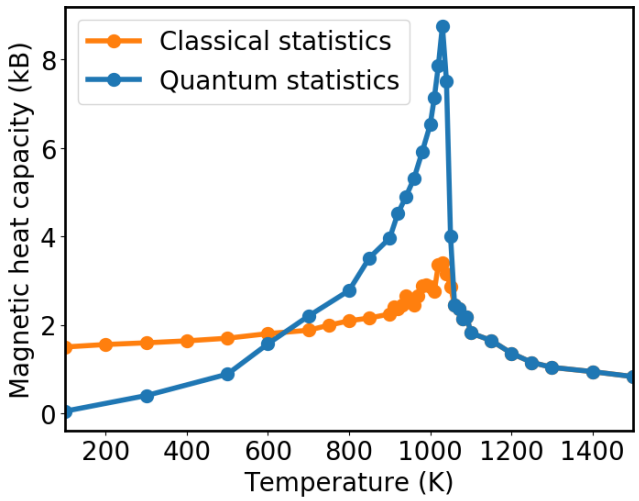

FIGURE 3.9: Temperature evolution of the magnetic heat capacity, obtained using classical and quantum statistics.

3.0.2 Magnetic parameters for pure bcc Mn

Since we are mainly interested in the Fe-rich limit of bcc Fe-Mn alloys, the accurate prediction of bcc Mn bulk properties is a bit out-of-focus. However, it is necessary to fit correctly Mn-Mn parameters in order to predict properly the interaction between several Mn solutes, or eventually the formation of Mn-clusters in Fe.

The overall principle of the fitting of Mn magnetic parameters is similar to Fe. As in the case of Fe magnetic interactions, five interaction ranges are considered for Mn magnetic parameters. DFT calculations of various magnetic configurations of pure bcc Mn have been performed and a least-square regression allows to associate the total energy variations to magnetic interaction and magnetic moment magnitude variations.

Please note that as the relative values of Fe-Mn and Mn-Mn magnetic interactions have a lot of effect on the magnetic ground-state predicted via MC simulations (especially in Mn-cluster configurations), the fitting of these interactions involved an intensive iterative procedure.

As shown in DFT results of chapter 2, Mn-Mn magnetic interactions must also ensure that two $1nn$ or $2nn$ Mn atoms are coupled antiferromagnetic to each other, while at longer distances (isolated Mn solutes), the antiferromagnetic Fe-Mn interaction should be dominant. It is then necessary to constrain the fitting procedure in order to obtain J^1_{Mn} and J^2_{Mn} coefficients with positive values, while longer distance coefficients should have small enough values to be overcome by the Fe-Mn interactions.

More generally, various constraints are added to the fitting procedure in order to obtain a model that predicts properly the ground-state of most Mn clusters in Fe. For instance, in order to predict the same ground-state as DFT for a Mn trimer in Fe (see Fig. 2.10 in chapter 2), it is necessary to ensure that the $2nn$ Mn-Mn AF interactions are weaker than $1nn$ Mn-Mn AF interactions. The same principle is applied to each configuration available in our DFT dataset.

As we are using a quite simple formalism, compared to the complexity of the phenomena at stake, it is difficult to correctly predict the DFT ground-state of each atomic configuration. The best compromise we found so far (eg. the final model) predicts correctly the DFT ground-state of every Mn-cluster configuration from 2 to 8 atoms, except in the case of the 5-Mn cluster where ground-state obtained from Monte Carlo simulations is found 0.01 eV/Mn more energetic by DFT calculations.

Fig. 3.10 shows the model prediction of the energy difference between the ground-state and various ordered magnetic states of pure bcc Mn, using DFT magnetic configurations as input. The comparison with DFT results shows that the energy hierarchy of the various ordered magnetic states is well represented.

A major issue here is that the magnetic ground-state of bcc Mn is found by DFT to be double-layer antiferromagnetic (see section 1.1.3 in chapter 1), which is

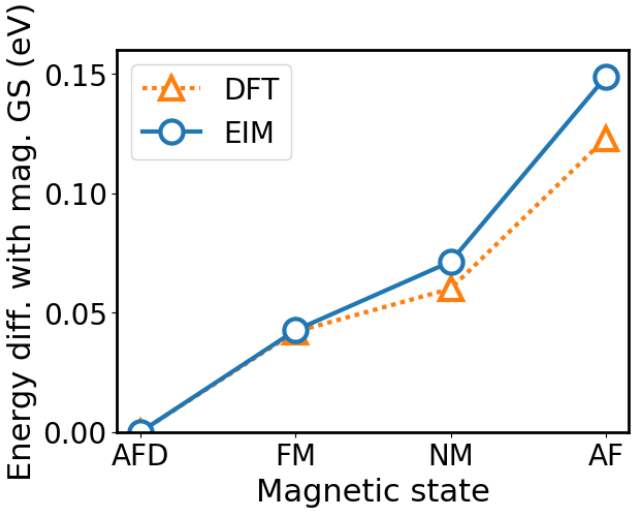

FIGURE 3.10: Model predictions of the energy differences between ordered magnetic states of bcc Mn compared to DFT results

an anisotropic magnetic state. In the formalism which is used in this study, pair-interactions are defined as a function of the neighbor-shell, which prevents the prediction of such AFD magnetic state via Monte Carlo simulation.

When using the DFT predicted magnetic state as an input, the AFD state is properly predicted as the lowest energy magnetic state, compared to FM, AF and NM states (see Fig. 3.10). However, when performing MC simulations, the model cannot handle direction dependent magnetic coupling (for instance at $1nn$ distance, each atom should have a ferromagnetic interaction with its four "right" neighbors and an antiferromagnetic interaction with its four "left" neighbors).

The resulting magnetic ground-state predicted by Monte Carlo simulation is a spin-glass without long-range order. However, the analysis of $1nn$ and $2nn$ magnetic short-range order in this spin-glass shows some similarities with AFD state. In AFD magnetic state, 50% of $1nn$ (67% of $2nn$) interactions are ferromagnetic which translates as a pair-correlation of 0.00 at $1nn$ and 0.33 at $2nn$. In the predicted spin-glass, we calculate a pair-correlation of -0.42 at $1nn$ and 0.33 at $2nn$.

We note that, using 1K spin Monte Carlo simulations, the energy difference between the Monte Carlo predicted ground-state of pure Mn and the AFD state is 0.021 eV/atom.

Fig. 3.11 shows the curves of the magnetic on-site energy as a function of the magnetic moment magnitude for Fe and Mn atoms, defined with the following expression:

$$E_{site}^{mag} = A_i M_i^2 + B_i M_i^4 \tag{3.9}$$

As explained earlier, the role of this term is to prevent the divergence of the magnetic moment magnitudes caused by the spin longitudinal fluctuation. Indeed, if

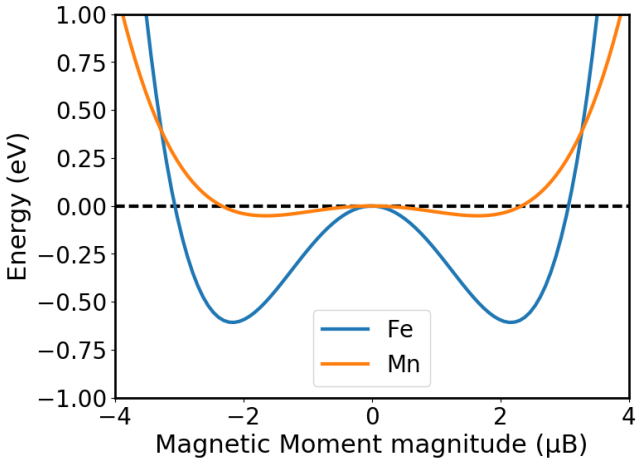

FIGURE 3.11: Evolution of the magnetic on-site energy as a function of the magnetic moment magnitude, calculated using the expression in eq. 3.9. The magnitude of Fe spins is stiffer than the magnitude of Mn spins.

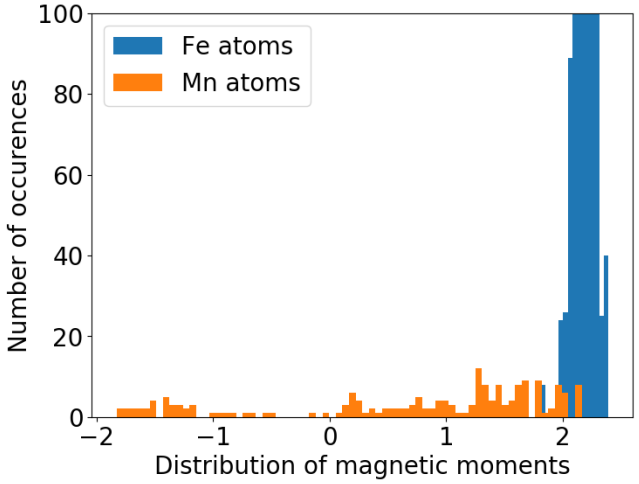

FIGURE 3.12: Distribution of Fe and Mn local magnetic moments in Fe-Mn SQS alloys, up to 50 at.% Mn.

spin longitudinal fluctuations are allowed in a classical Heisenberg model, the system energy can be infinitely minimized by increasing the magnetic moments magnitudes. As can be noticed in Fig. 3.11 the minimum of the Mn curve is more shallow than the one of Fe, which is expected as we have shown in chapter 2 that the magnetic moment magnitude of Mn atoms is much more dispersed than the ones of Fe atoms. Fig. 3.12 shows the distribution of Mn and Fe atoms magnetic moments magnitudes (in random solutions up to 50 at.% Mn) in DFT calculations of chapter 2.

3.0.3 Magnetic parameters for bcc Fe-Mn alloys

The fitting of Fe-Mn magnetic interactions is quite complex because the magnetic subtilities of Mn shown in the DFT results (see chapter 2) have to be reproduced. As in pure Fe and Mn magnetic parameters, five interaction ranges are considered for Fe-Mn magnetic interactions.

The first issue is that when performing Monte Carlo simulations with a Heisenberg-like model, any magnetic frustration may be solved by relaxing the spins to be orthogonal to each other. As the pair-interactions is based on a dot-product, which depends on the cosinus of the angle between the spins, spins orthogonal to each other are not interacting. For instance the magnetic state of Mn-clusters in Fe is highly based on the competition between the various Mn-Mn and Fe-Mn magnetic interactions. If the model is only fitted on collinear DFT data, these competitions lead to highly non-collinear structures which have a high energy according to DFT calculations.

In order to solve this problem, we added to the Fe-Mn magnetic interactions an angle dependence, fitted on DFT non-collinear data obtained for an isolated Mn solute in bcc Fe (see 2). The principle is to add a penalty term that depends on the angle between the Mn atom magnetic moment and the average magnetic moment of the Fe atoms in the two nearest-neighbor shells around the concerned Mn atom.

In Fig. 3.13 is shown the energy difference between an isolated Mn atom in a ferromagnetic Fe matrix with various angles compared to the Fe atoms and the same configuration at ground-state (Mn antiparallel to Fe). As can be observed, our expression is adequate and allows to properly model the non-collinear barrier between the two collinear minima.

As shown in chapter 2, another property to take into account is that Fe-Mn coupling tendency in random solutions depends on Mn concentration. In the dilute limit, the Fe-Mn interaction tends to be antiferromagnetic while at higher concentration (more than 7 % at. Mn) it becomes ferromagnetic. In order to properly reproduce this feature, a local concentration dependent term (fourth degree polynomial) is added to the Fe-Mn magnetic parameters, as explicited in expression 3.10.

This formalism allows to properly simulate the concentration dependency of the Fe-Mn magnetic coupling tendency, as shown in Fig. 3.14, in comparison with DFT calculations. The change of average magnetic state is also explicited by the angle

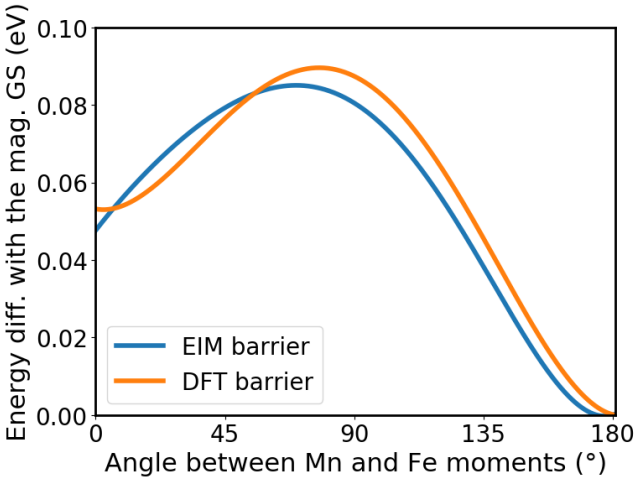

FIGURE 3.13: energy difference between an isolated Mn atom in a ferromagnetic Fe matrix with various angles compared to the Fe atoms and the same configuration at ground-state (Mn antiparallel to Fe).

distribution of Mn magnetic moments compared to the average magnetic moment of Fe atoms. The results shown in Fig. 3.15 are obtained with spin Monte Carlo simulation at 10K in random Fe-Mn solutions at 1, 6 and 10 at. % Mn. It is clear that at 1% the coupling tendency between Mn and Fe is antiferromagnetic while increasing the concentration favors more and more the ferromagnetic coupling.

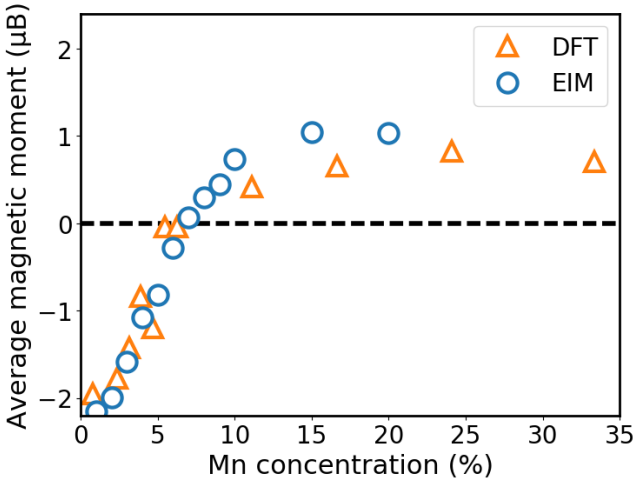

FIGURE 3.14: Average magnetic moment of Mn atoms as a function of Mn concentration, from DFT calculations and Monte Carlo simulations.

The total expression of Fe-Mn interaction parameters is:

$$J^n_{Fe-Mn} = \left[J^n_0 \cdot \frac{\theta - 90}{90}\right] + \left[a \cdot [Mn]^4_{loc} + b \cdot [Mn]^3_{loc} + c \cdot [Mn]^2_{loc} + d \cdot [Mn]_{loc} + e\right] \tag{3.10}$$

where the J^n_0 is the original J^n_{Fe-Mn} parameter, before considering the angle and concentration dependencies. This parameter ensures the range dependence of the

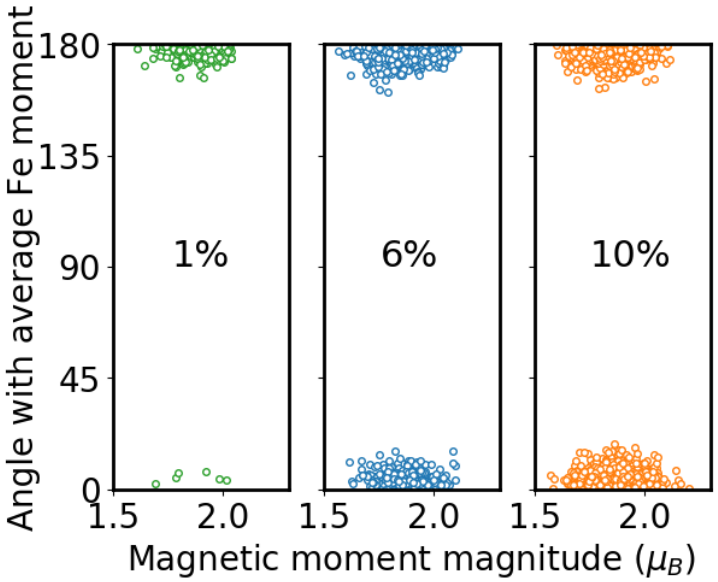

FIGURE 3.15: Angle distribution between Mn magnetic moments and the average magnetic moment of Fe atoms, in random solutions at 1, 6 and 10 at. % Mn concentrations.

interaction (Since the angle and concentration dependencies do not depend on the interaction range). θ is the angle between the Mn magnetic moment and the average of the spins of the Fe atoms in the two nearest-neighbor shells of the considered Mn atom. $[Mn]_{loc}$ is the local Mn concentration (in the five nearest-neighbor shells around the concerned atom).

3.0.4 Non-magnetic parameters

At this point, the whole magnetic contribution of the Hamiltonian is fitted and may be used to determine the magnetic contribution of the energy of a given system. It is then possible to calculate the magnetic mixing energy of various concentration Fe-Mn random solutions. The difference between the mixing energy obtained from DFT calculations (which includes magnetic and non-magnetic contributions) and the model magnetic contribution of the mixing energy provides the model non-magnetic contribution of the mixing energy. Chemical parameters of the model are fitted in order to accurately reproduce the DFT total mixing energy with the model, using DFT configurations as input, as shown in Fig. 3.16.

3.1 Curie temperature of Fe-Mn alloys

The Curie temperature is a fundamental property of ferromagnetic materials. As our ambition is to build a model able to describe properly the thermodynamic properties of Fe-Mn alloys, the Mn concentration dependence of T_C in dilute Fe-Mn alloys is of great interest.

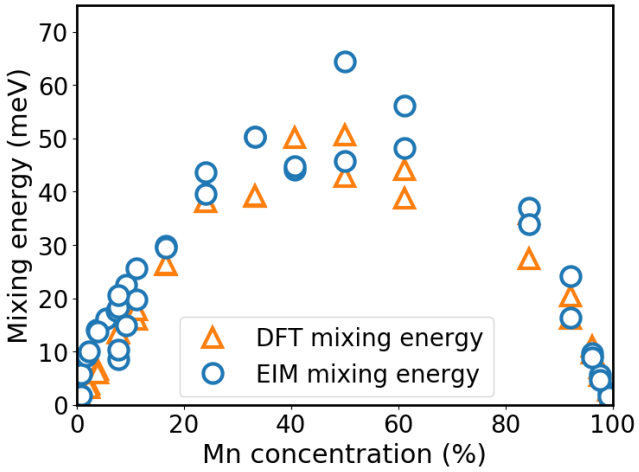

FIGURE 3.16: Total mixing energy obtained from DFT calculations and the effective interaction model with DFT configurations as input

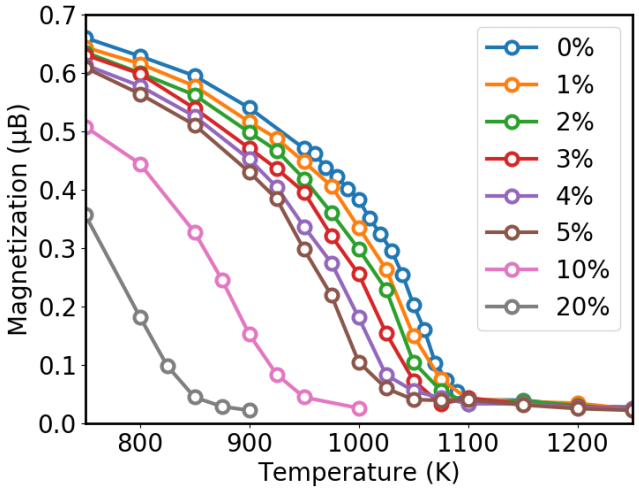

FIGURE 3.17: Temperature evolution of the bulk magnetization, for various Mn atomic concentrations.

We estimate the Curie temperature of dilute bcc Fe-Mn alloys by determining the temperature dependence of bulk magnetization for various Mn concentrations. These calculations are all performed in random solutions. To do so, we performed spin-MC simulations on a 16000 atoms system (20x20x20 cubic unit cells). Random solutions are generated by randomly distributing p Mn atoms in the Fe matrix, where p is defined as the total number of atoms multiplied by the imposed Mn atomic concentration. For each temperature and each concentration, $5 \cdot 10^8$ spin relaxation attempts are performed. In the worst case scenario, the convergence is reached after approximately 10^8 steps. We add $4 \cdot 10^8$ MC-steps after convergence for data collection.

Please note that due to the amount of time needed to determine the magnon density of states in alloys, the whole study (in the whole chapter) is done using classical statistics. Although we are aware that the shape of the $M(T)$ curves is not correct, the value of T_C should not be affected.

T_C is considered as the inflection point of the $M(T)$ curve. As shown in Fig. 3.17 the magnetization curve is shifted to the low temperatures when increasing Mn concentration.

The T_C of each calculated concentration is reported in Fig. 3.18 in order to compare with experimental results. As can be seen, T_C decreases with Mn concentration with a slope of approximately 10K per Mn atomic percent, in excellent agreement with most literature data. Experimental works have shown that T_C tends to decrease linearly with Mn concentration, at a rate of approximately 10K per Mn atomic percent according to most studies [126, 7, 94, 138], as shown in Fig. 3.18. However, a study of Yamauchi *et al.* [181] has found a higher decreasing slope of approximately 43K per Mn atomic percent, in disagreement with all the other studies. One possible explanation to this deviation is that the magnetic measurements of Yamauchi *et al.* are biased by the use of cold-rolling on the samples in order to stabilize the body-centered cubic phase [181], which is not the case in the four other studies mentioned. A recent study indeed suggest that plastic deformation has a significant impact on short-range clustering of α-Fe-Mn solutions [147]. We note that in order to stabilize α-Fe-Mn beyond 5 % at. Mn, Paduani *et al.* have added 3 % at. Ti to the solution [126]. As the low concentration results (below 5% at . Mn) of Paduani *et al.* are in excellent agreement with the studies using pure Fe-Mn, it can be assumed that there is not significant effect of such Ti addition on the magnetic state of the solution. A Recent Calphad assessment [14] also predict such a decrease of T_C with Mn concentration, as shown in Fig. 3.18.

3.2 Temperature dependance of Mn magnetic moment

As shown in section 3.0.3 (Fig. 3.14), the average magnetic moment of Mn atoms in bcc Fe-Mn solid solutions obtained from 1K Monte Carlo simulations shows the same Mn concentration dependence as DFT calculations. It tends to be anti-ferromagnetic

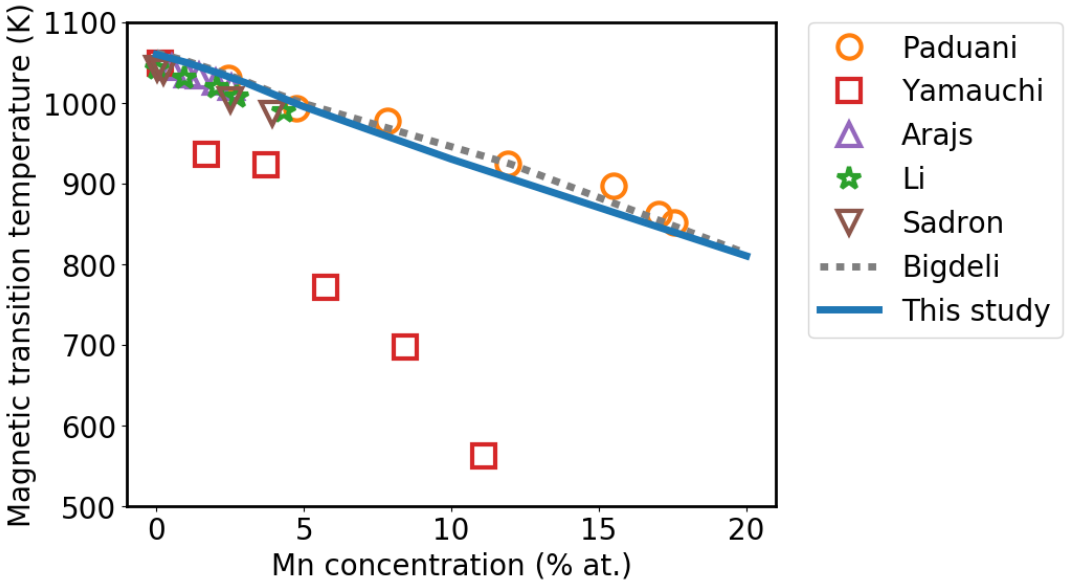

FIGURE 3.18: Curie temperature of dilute bcc Fe-Mn alloys as a function of Mn concentration. The solid blue line show our results while the symbols show literature experimental results. circles: Paduani *et al.* [126], squares: Yamauchi *et al.* [181], upward triangles: Arajs *et al.* [7], stars: Li *et al.* [94], downward triangles: Sadron *et al.* [138], dotted line: Bigdeli *et al.* [14]

at low concentration (under the transition, which occurs around 7% at. Mn) and ferromagnetic at high concentration.

Using our model with spin Monte Carlo simulations, we determine the evolution of the average magnetic moment of Mn atoms with temperature, at fixed atomic random configurations in order to avoid the appearance of atomic short-range order. Fe-Mn random alloys at 0.1, 1 and 10% at. Mn are studied, in order to represent both magnetic regimes, below and beyond the magnetic transition concentration.

These simulations are performed on a 16000 atoms system (20x20x20 cubic unit cells). Random solutions are generated by randomly distributing p Mn atoms in the Fe matrix, where p is defined as the total number of atoms multiplied by the imposed Mn atomic concentration. For each temperature and each concentration, $5 \cdot 10^8$ spin relaxation attempts are performed. In the worst scenario, the convergence is reached after approximately 10^8 steps. We add $4 \cdot 10^8$ MC-steps after convergence for data collection.

As can be observed in Fig. 3.19, in both cases the absolute value of the average magnetic moment of Mn atoms decreases with temperature not only faster than the average moment of Fe, but also without any regard to the evolution of the bulk magnetization (shown in Fig. 3.19). In the truly isolated case (0.1 at.% Mn) the decrease is almost linear and the curve reaches 0 approximately at Curie temperature. The more concentrated the solution is, the sharper is the decrease.

For comparison, unpublished results on Fe-Cr alloys were kindly provided by our colleague M. Trochet. These results suggest that Cr follows the same decrease

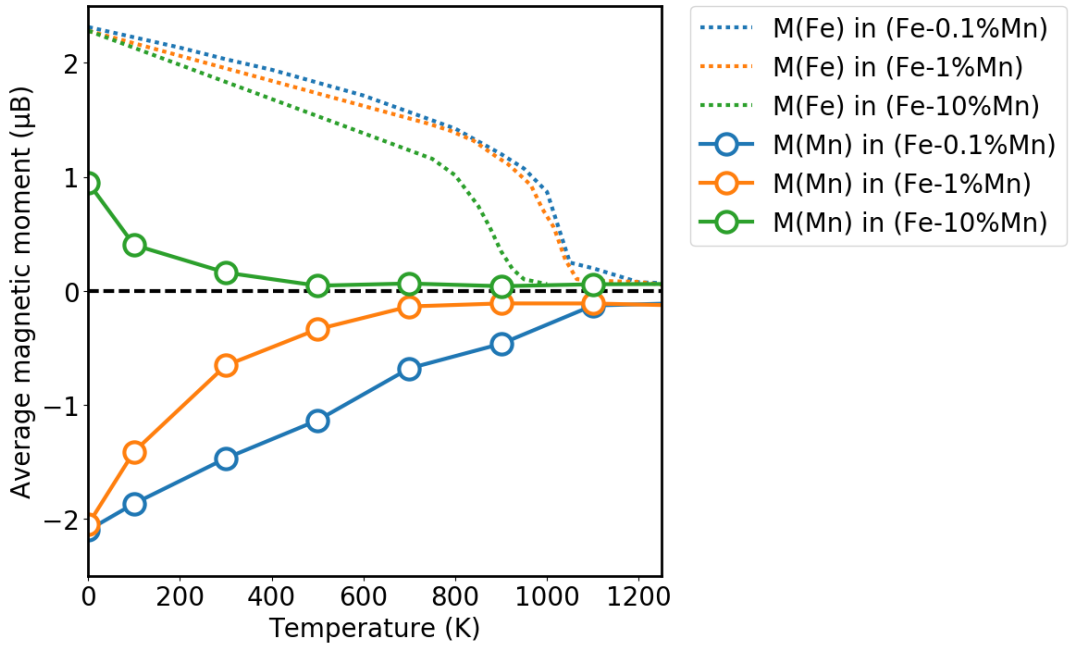

FIGURE 3.19: Temperature evolution of the average magnetic moment of Mn atoms in bcc Fe-Mn at various concentrations (0.1, 1 and 10 % at. Mn). The bulk magnetization of pure bcc Fe is shown as a black dotted line for shape comparison.

shape as Fe, contrary to Mn.

Further analysis or our data shows that the magnetic moment magnitude of Mn atoms tends to increase with temperature in a range between 1.85 and 2.05 μ_B. This leads to the conclusion that the loss of average magnetic moment does not come from the longitudinal fluctuations.

On the other hand, as we know that Mn can couple either parallel or antiparallel with the Fe atoms of the matrix. We know from DFT calculations that one of these minima has a lower energy than the other, depending on the Mn concentration. As the energy difference is not very high between these two states (0.05 eV), it is plausible that increasing temperature tends to redistribute "more randomly" the Mn atoms between AF and FM states.

As shown in Fig. 3.21, the evolution of the FM-Mn ratio with temperature tends to confirm this hypothesis. We can indeed observe that, in agreement with DFT calculations, the ratio of FM-Mn atoms at low temperature is approximately 0% at 0.1 and 1 at.% Mn concentrations, and approximately 67% at 10 at.% Mn concentration. As temperature increases, the ratio of FM-Mn tends to go from 0% (or 67% depending on concentration) to 50%.

We compared in Fig. 3.22 the ratio of FM-Mn among Mn atoms at 0.1 at.% Mn obtained from Monte Carlo simulations, with the expected ratio from Boltzmann theory, expressed as follows:

$$\frac{N_{FM-Mn}}{N_{AF-Mn}+N_{FM-Mn}} = \frac{exp(\frac{-\Delta E}{k_B T})}{1+exp(\frac{-\Delta E}{k_B T})} \tag{3.11}$$

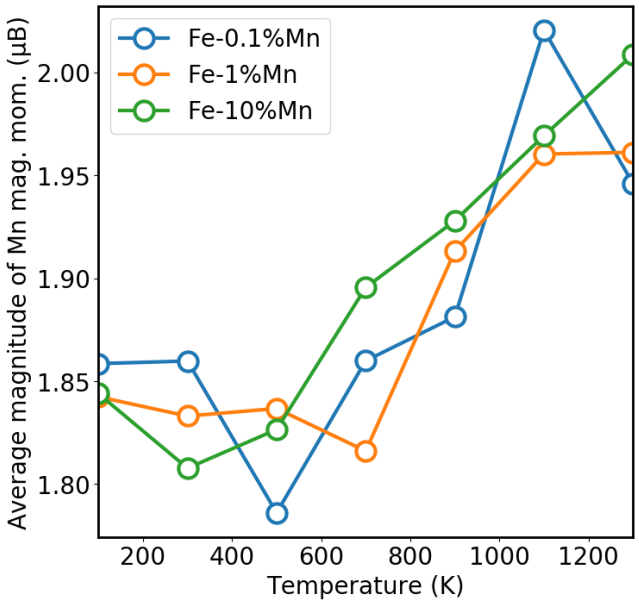

FIGURE 3.20: Temperature evolution of the average magnitude of Mn atoms magnetic moments in bcc Fe-Mn at various concentrations (0.1, 1 and 10 at.% Mn).

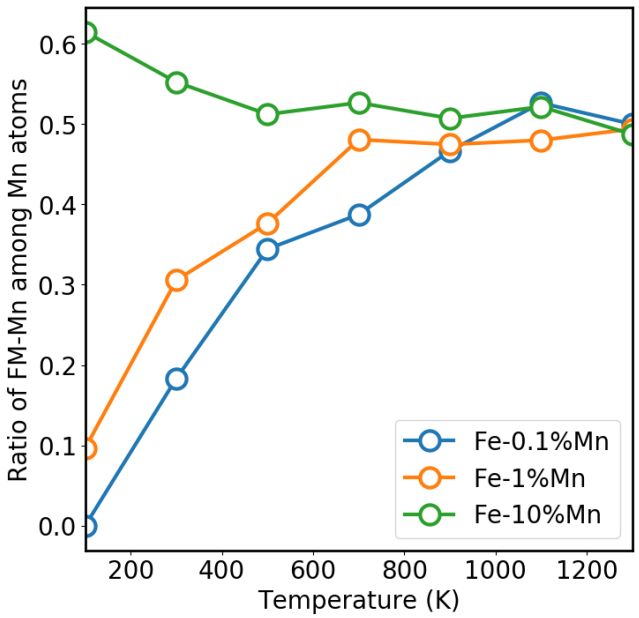

FIGURE 3.21: Temperature dependence of the ratio of FM-Mn among Mn atoms in bcc Fe-Mn at various concentrations (0.1, 1 and 10 % at. Mn).

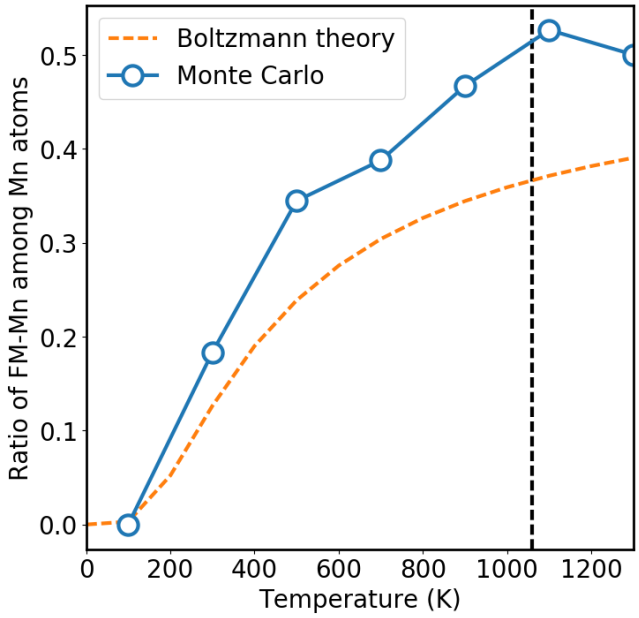

FIGURE 3.22: Temperature dependence of the ratio of FM-Mn among Mn atoms in bcc Fe-Mn at 0.1 at.% Mn compared to the expected ratio from Boltzmann theory (orange dashed line). The deviation is explained by the magnetic disordering of Fe.

with N_{FM-Mn} and N_{AF-Mn} being respectively the number of FM-Mn and AF-Mn atoms, and ΔE being the energy difference between FM-Mn and AF-Mn states obtained from DFT calculations (ΔE = 0.05 eV).

Despite similar overall trends, we notice that as temperature increases the deviation between the two curves increases. This can be explained as the Boltzmann ratio is obtained using the energy difference between AF-Mn and FM-Mn at ground-state. As the magnetic disordering of the matrix increases with temperature, we expect the energy difference between both Mn magnetic states to be lowered, which explains that the ratio goes faster to 50 % than expected from Boltzmann theory.

3.3 Temperature dependance of Fe-Mn mixing energy

As explained in section 3.0.3, the mixing energy of Fe-Mn solid solutions was used in order to fit the non-magnetic interaction parameters of the model. However, knowing that the model predicts a reasonable mixing energy when applied to the magnetic configurations obtained from DFT calculation does not ensure that the Monte Carlo simulations are in good agreement with these results. Indeed, spin Monte Carlo simulations bring the system to the magnetic ground-state predicted by the model, which may differ from the DFT ground-state.

The concentration dependence of bcc Fe-Mn mixing energy is determined by generating Fe-Mn random alloys at various concentrations and by calculating the total energy of these systems. The magnetic state of these random configurations is relaxed via spin Monte Carlo simulation, while the atomic structure is kept constant

in order to prevent the possible appearance of atomic short range order or any phase separation. The mixing energy is then obtained using the following expression:

$$E^{mix}(\text{Fe-Mn}) = \frac{E^{tot}(n\text{Fe} + p\text{Mn}) - nE(\text{Fe}) - pE(\text{Mn})}{n+p} \tag{3.12}$$

where $E^{tot}(n\text{Fe} + p\text{Mn})$ is the total energy of the Fe-Mn solid solution, $E(\text{Fe})$ is the energy per atom of pure bcc Fe (in its lowest energy magnetic state: FM) and $E(\text{Mn})$ is the energy per atom of pure bcc Mn (in the lowest energy magnetic state: spin glass, see section 3.0.2).

These simulations are done on a 16000 atoms system (20x20x20 cubic unit cells). Random solutions are generated by randomly distributing p Mn atoms in the Fe matrix, where p is defined as the total number of atoms multiplied by the imposed Mn atomic concentration. For each temperature and each concentration, $5 \cdot 10^8$ spin flips attempts are performed. In the worst scenario, the convergence is reached after approximately 10^8 steps. We add $4 \cdot 10^8$ MC-steps after convergence for data collection.

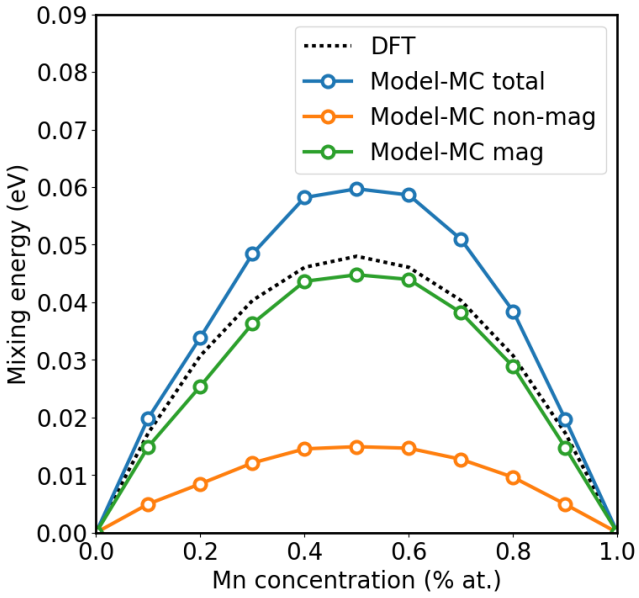

FIGURE 3.23: Mixing energy as a function of Mn atomic concentration. The black dotted line shows the results obtained with DFT for comparison, the blue line shows the total mixing energy obtained from MC simulations, the green and the orange lines respectively show the magnetic and the non-magnetic contributions of the mixing energy obtained via MC simulations.

As can be seen in Fig. 3.23, the mixing energies obtained via Monte Carlo simulations are positive for all the concentrations, which reveals an unmixing tendency in good agreement with the one obtained with DFT calculations. It is in good agreement with earlier DFT [96] and experimental [62] results.

These MC simulations are performed at 1K in order to avoid any temperature effect and to be as comparable as possible with DFT results. Please note that Fig.

3.16 shows the mixing energy obtained using the model on the magnetic ground-state predicted by DFT calculations, while Fig. 3.23 shows the mixing energy from the magnetic ground-state obtained using spin Monte Carlo simulations at 1K.

The present approach allows to easily split the magnetic and non-magnetic contributions, as shown in Fig. 3.23. As can be noticed, magnetic and non-magnetic contributions to the mixing energy have the same order of magnitude, even though the major effect seem to come from the magnetic contribution (The non-magnetic contribution represents approximately one fourth of the total mixing energy).

The same simulations were performed at various temperatures in order to study the effect of temperature on the mixing energy of bcc Fe-Mn random alloys.

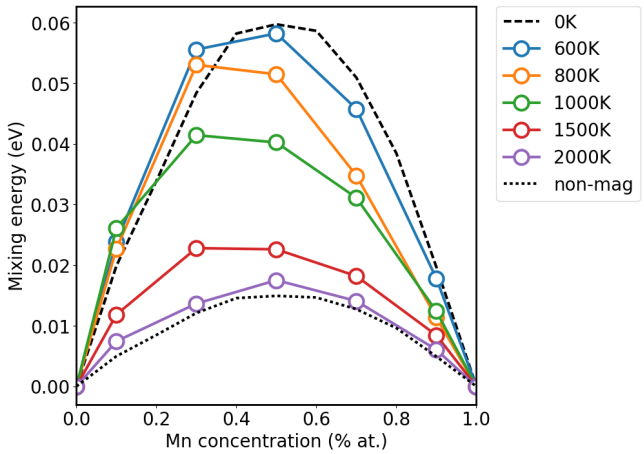

FIGURE 3.24: Mixing energy as a function of Mn atomic concentration for various temperatures. The black dashed line shows the low temperature limit of mixing energy while the black dotted line shows the non-magnetic contribution, also corresponding to the high temperature limit.

As can be observed in Fig. 3.24, the temperature evolution of bcc Fe-Mn mixing energy seems roughly related to the magnetization. Indeed, two regimes can clearly be identified from these results: When below the magnetic transition temperature, the mixing energy curve remains quite similar to the 0K limit, while beyond the magnetic transition temperature, it converges to a high temperature paramagnetic limit. It can be noticed that an asymmetry appears between the Mn-rich and the Fe-rich domains of the mixing energy curves. Indeed, despite the fact that both high and low temperature asymptotes are quite symmetrical, the Mn-rich mixing energy seems to decrease faster at intermediate temperatures than the Fe-rich side. We believe that this asymmetry arises from the difference between the Fe-rich and Mn-rich magnetic transition temperatures. As described in section 3.1, we predict the magnetic transition temperature to decrease with Mn concentration (see Fig. 3.18). (I still have to check the Tc at high Mn concentration)

We note that the decrease of the mixing energy with temperature is only due to the magnetic contribution as there is no atomic exchange in these simulations, which implies that the atomic configuration is constant. Hence, it is not surprising that the

paramagnetic limit of the mixing energy curve is quite similar to the non-magnetic contribution of the 0K mixing energy (shown in Fig. 3.24).

These results suggest that spin disordering favors the mixing of Fe and Mn, while spin ordering favors the phase separation tendency.

3.4 Temperature and concentration evolution of atomic short-range-order

Every Monte Carlo results presented in this chapter up to this point are performed by relaxing the magnetic state of the system while the atomic structure is kept constant. As we are interested in understanding the interplay between the magnetism and thermodynamic properties in bcc Fe-Mn alloys, it is important to study the evolution of the atomic structure. To do so, in addition to the Monte Carlo spin relaxations performed in previous sections, we add atomic relaxations (by relaxation are meant atomic exchanges, we are still working on rigid lattice).

We consider in our study that the characteristic time for spin variations is smaller than the one of atomic-exchanges. Hence, once every N spin-MC steps, an attempt is made to exchange the respective positions of two random atoms, following the Metropolis criterion.

Since we are not considering kinetic properties in the present approach, these spin-MC relaxations only have an effect on the computational efficiency, not on the physical results. Convergence tests were still done in order to ensure that enough spin-MC steps are performed between each atomic-exchanges. For these calculations, 100 spin-MC attempts are done randomly anywhere in the system and 500 spin-MC attempts are performed in the two nearest-neighbor shells of the exchanged atoms, between two atomic-exchanges.

Using the approach previously described, bcc Fe-Mn alloys were studied at various concentrations and temperatures, in order to evaluate the clustering tendency as a function of these two variables. For a given set of concentrations and temperatures, we consider the Cowley-Warren formalism of atomic short-range order [28, 172], being the average over all Mn atoms of the α_i^{Mn} parameter defined as:

$$\alpha_i^{Mn} = 1 - \frac{n_i}{Z_i C_{Fe}} \tag{3.13}$$

where n_i is the number of Fe atoms on the i-th nearest-neighbor shell from the considered Mn atom, Z_i is the coordination on the i-nn shell, and C_{Fe} is the Fe atomic concentration of the system.

For each concentration and temperature, the system is initialized as a random solution (disordered atomic configuration) and the magnetic state is initially thermalized. We note that the initial spin-relaxation is performed using the same simulation settings as the previous sections in order to ensure the convergence of the magnetic

state. Once the system is thermalized, pairs of Fe and Mn atoms are selected randomly and their exchange is validated or not depending on the Metropolis criterion, while the magnetic structure is relaxed on-the-fly as described earlier in this section.

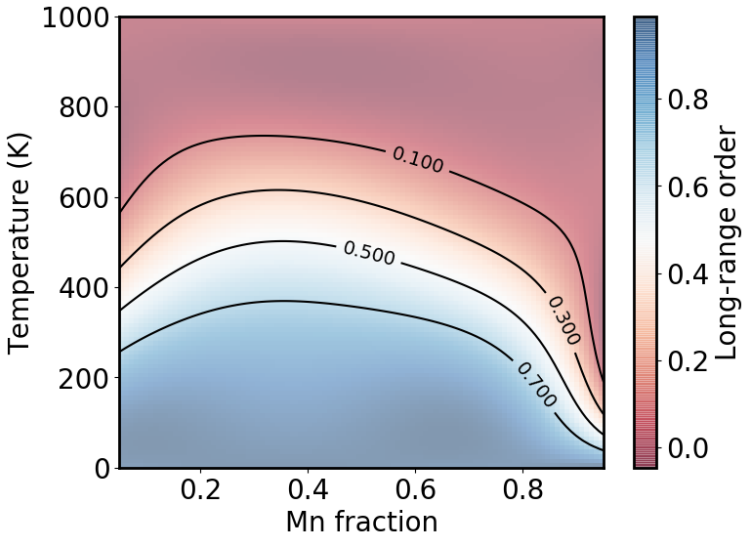

FIGURE 3.25: Cowley-Warren 1*nn* short-range order parameter as a function of Mn atomic concentration and temperature.

In Fig. 3.25 is shown a heatmap of the calculated Cowley-Warren SRO as a function of Mn concentration and temperature.

Looking at the isovalues of the Cowley-Warren short-range order parameter plotted in Fig. 3.25, it can be noticed that temperature evolution of the atomic 1*nn* short-range order is not symmetrical with respect to the Mn atomic concentration. This asymmetry is consistent with the mixing energy being asymmetrical, as shown in section 3.3.

In order to determine the transition between phase separation and solid solution the use of semi-grand canonical simulations is required. However, our canonical simulations still allow to roughly estimate this transition.

As there is no data in the literature concerning this property for α-Fe-Mn systems, we cannot directly compare our results. However, it is possible to compare qualitatively our results by analogy with bcc Fe-Cr alloys.

From the literature [93], we know the concentration dependence of the mixing enthalpy in bcc Fe-Cr. Despite being slightly negative in the Fe-rich domain, the overall behavior follows quite correctly the regular solution model, with a maximum of approximately 100 meV (from DFT-PAW-GGA calculations [93]). As we find approximately 50 meV with similar calculation settings, the transition temperature in bcc Fe-Mn should be roughly half the one of Fe-Cr alloys. Literature studies report the 50% at. Fe-Cr phase separation temperature to be approximately 1100K [146]. If neglecting the effects of vibrational entropy in Fe-Mn, it is then reasonable to expect the 50% at. Fe-Mn phase separation temperature to be around 550K. Please note that this is a very rough reasoning imposed by the lack of literature on this feature.

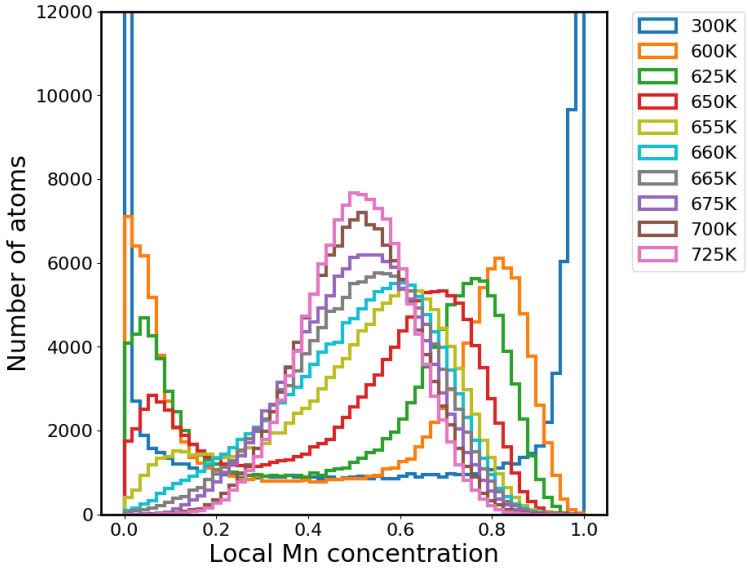

FIGURE 3.26: Distribution of the local Mn concentration calculated on the five nearest-neighbor shells of each atom.

In order to evaluate the transition temperature between phase separation and solid solution, we studied the distribution of local Mn concentration in the system. In practice, the number of Mn atoms among the five nearest-neighbor shells of each atom is counted and plotted as an histogram shown in Fig. 3.26. We determine the transition to be at approximately 660K, as beyond this temperature, we only observe one peak (a mono-phase solid solution) at 50 at. % Mn while below this temperature we notice two peaks revealing two phases (one Fe-rich phase and one Mn-rich phase). This value is in reasonable agreement with the rough approximation expected by analogy with Fe-Cr alloys.

3.5 Effects of external field in Fe-Mn alloys

Among experimental literature studies on Fe-based alloys, many are performed with the use of an external magnetic field. An external field, may it be constant or fluctuating, allows to obtain some key properties of the alloys. For instance, magnetization measurement experiments [181] consist in measuring the magnetic response of the alloy to an oscillating external magnetic field. Also, another example is the polarized neutron scattering experiments [128], for which a constant magnetic field is applied in order to polarize the neutrons. Typical values of these external magnetic fields are lower than 3T [181, 128, 71]. As Mn solutes in bcc Fe exhibit two distinct energy minima depending on its magnetic coupling with Fe atoms of the matrix, applying a magnetic field could in principle favor the ferromagnetic Fe-Mn coupling and induce a bias in experimental results. This hypothesis can be verified using our model. Applying a magnetic field is also useful as it allows for instance to isolate the magnetic effects on chemical decomposition. Finally, the effects of external magnetic

fields on the properties of the alloys is of prime interest for future nuclear fusion applications, as one of the most promising technologies involves very large external fields for magnetic confinement of fusion plasma.

Using the Ising, the Heisenberg or the Generalized Heisenberg models, there is a rather simple way to include external magnetic field effects as it only requires to add a term to the Hamiltonian:

$$H_{field} = H^0 - \sum_{i}^{N} \mu_0 g_i \mathbf{H} \cdot \mathbf{M_i} \tag{3.14}$$

where H^0 is the Hamiltonian without external field, μ_0 is the Bohr magneton, $\mathbf{M_i}$ is the magnetic moment of the $i-$th atom and g_i is the Landé g-factor of the $i-$th atom species. Here, the g-factor was considered for both Fe and Mn equal to 2.01 (dimensionless) [8]. Finally, $\mathbf{H}$ is the external magnetic field applied to the system.

We note however that using this simple approach, possible effects on the magnetic moments magnitude might not be accurately taken into account.

3.5.1 Pure Fe

In order to validate our approach, we determined the effects of an external magnetic field on the Curie temperature of pure bcc Fe. The field dependence of T_C can indeed be found in the literature for comparison.

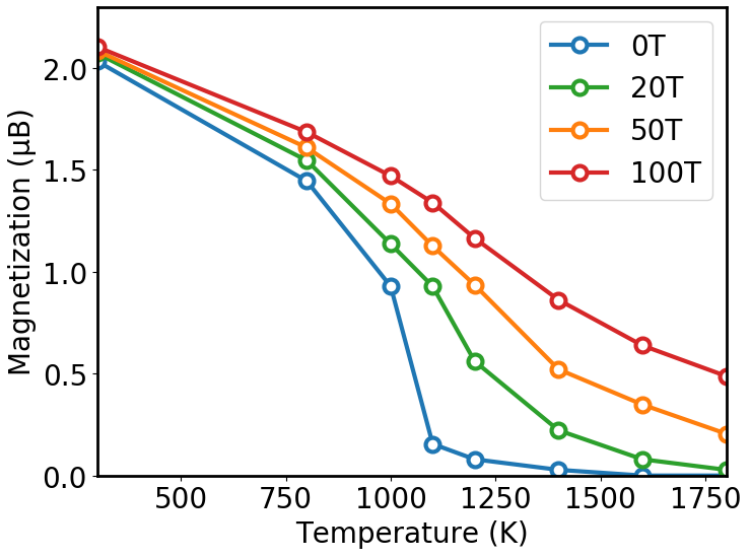

FIGURE 3.27: Temperature dependance of the bulk magnetization of pure bcc Fe with various applied magnetic fields from 0 to 100T

The temperature dependence of Fe magnetization for various values of the external field are shown in Fig. 3.27. As can be noticed, not only the Curie temperature is shifted to higher temperatures when the external field is increased, but the magnetization drop becomes smoother and smoother with the increase of the magnetic field. These results are in very good agreement with a previous spin-lattice dynamics

study [26]. For instance, the difference between the 0T and the 100T magnetization at 800K is 0.3 μ_B in both studies, while this difference at 1200K is 1.2 μ_B in our work and 1.0 μ_B in [26] (these values are obtained visually from the figures of Ref. [26]).

3.5.2 Fe-Mn alloys

Earlier in this chapter (in section 3.18), we have shown that the Curie temperature decreases with the concentration of Mn by approximately 10K per Mn atomic percent. In order to determine if an external magnetic field may affect this property, we have performed simulations in order to determine the temperature dependance of bulk magnetization of Fe-Mn random solutions at 5 at.% Mn, with external magnetic fields up to 100T.

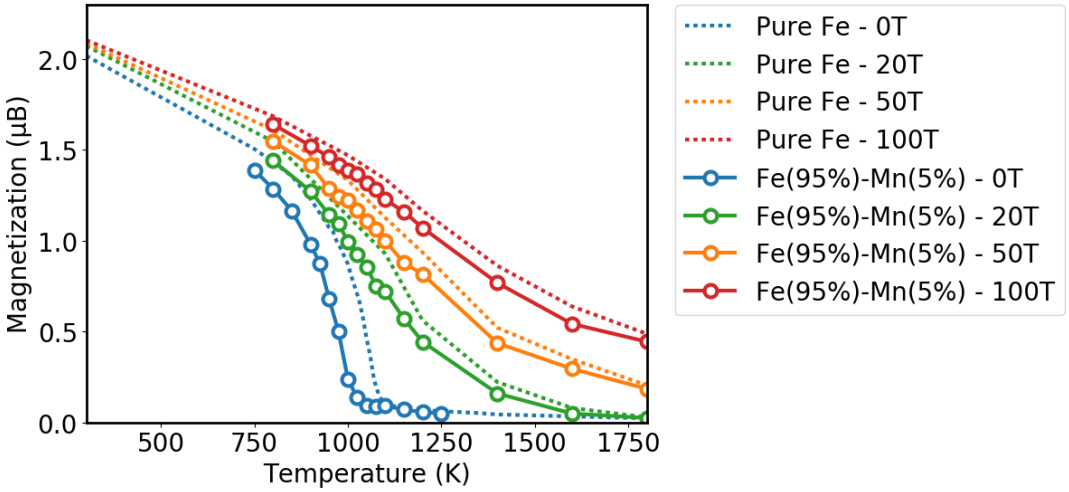

FIGURE 3.28: Temperature dependance of the bulk magnetization of bcc Fe-Mn (5 at.% Mn) with various applied magnetic fields from 0 to 100T

As shown in Fig. 3.28, the effects of Mn concentration on the magnetic transition temperature are similar with and without external magnetic field. With 5 at.% Mn, T_C is lowered by approximately 50K compared to pure Fe, with external fields of 20, 50 and 100T.

These simulations with external magnetic fields also allow to estimate the eventual effects of the field on the relative populations of AF-Mn and FM-Mn states. We performed some tests in order to study the ratio of AF-Mn and FM-Mn on random alloys at 1 at.% Mn concentration. We note that at this concentration without field, the average magnetic moment of Mn atoms is antiparallel to Fe. At 1K, we observe in Fig. 3.29 that the ratio of FM-Mn among the Mn atoms goes from almost 0 without field to almost 100% at 100T. Especially, we notice a sudden transition around 70T which brings from a slight majority of AF-Mn to a huge majority of FM-Mn.

In order to observe the possible effects of temperature on this feature, we also performed the same tests at 77 and 300K, which are typical experimental temperatures [128, 71]. As shown in Fig. 3.29, we note that for a given field, the magnetic

entropy induced by temperature pushes the ratio closer to 50% than the values at 1K. At both 77 and 300K, the transition from a majority of AF-Mn to a majority of FM-Mn is located around 50T, which is lower than at 1K (also because of magnetic entropy).

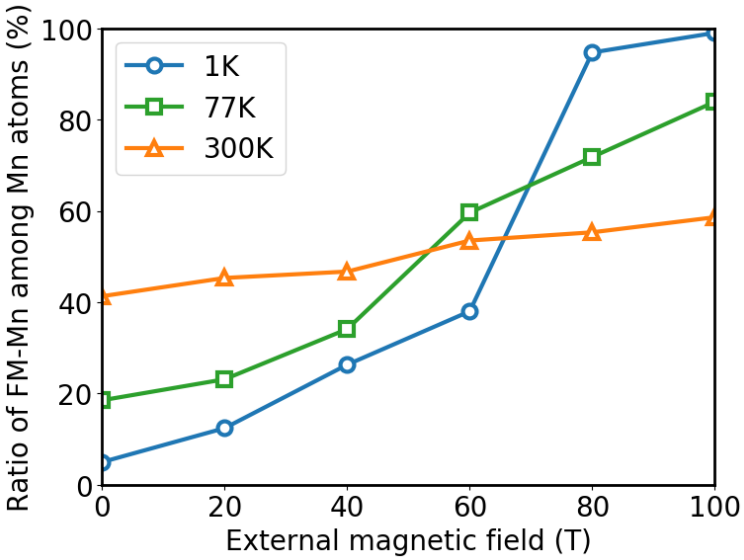

FIGURE 3.29: Ratio of Mn atoms with parallel magnetic moment to Fe atoms at 1, 77 and 300K for external magnetic fields between 0 and 100T.

These results suggest that very high magnetic fields may in principle have a significant effect on the ratio between AF-Mn and FM-Mn populations. However, such field values cannot be reached in standard experimental conditions. Hence, the discrepancies shown in chapter 2 between theoretical and experimental studies concerning the Fe-Mn coupling at low Mn concentration cannot be explained by the use of magnetic fields in these experiments Indeed, aforementioned experiments typically use external magnetic fields between 0 and 3T [181, 128, 71], while we have shown that dozens of Teslas are necessary to have a significant impact on the average magnetic moment of Mn atoms.

3.6 Conclusion

In the attempt of studying finite temperature properties of bcc Fe-Mn alloys, we parameterized an effective interaction model based on DFT results. The parameterization was performed via an iterative procedure, which consists in including one by one as many physical properties derived from DFT calculations as possible. This empirical procedure allowed us to obtain good agreements between DFT results and 1K Monte Carlo simulations with a reasonable fitting dataset. Indeed, the parameters are constrained to verify some general trends, for instance the fact that Mn-Mn magnetic interactions are dominant over Fe-Mn ones. Identifying these trends prior to the fitting allows to obtain a satisfactory model with a limited dataset,

especially compared to machine learning based approaches. We note that including non-collinear DFT calculations in the fitting dataset is essential to obtain a satisfactory model.

Some first finite temperature simulations were then performed in order to evaluate the ability of the approach to predict properties which are not included in the fitting data. For instance, the Mn concentration dependence of the magnetic transition temperature is found in excellent agreement with experimental results.

At variance with most experimental methodologies, which focus on average properties, our approach allows to access the magnetic moment of individual Mn atoms in dilute Fe-Mn alloys. It allowed to study the temperature evolution of the Mn magnetic coupling distribution with Fe, along with the evolution of magnitude of Mn magnetic moments. We observed that contrary to Cr atoms in bcc Fe-Cr alloys, the average magnetic moment of Mn atoms in bcc Fe-Mn does not follow the bulk magnetization decrease. We provide some arguments to explain this behavior.

The temperature dependence of the mixing energy over the whole range of concentration was also determined. The results suggest that the unmixing tendency is highly related to the magnetic order of the system.

As our approach allows to couple magnetic relaxation and atomic exchanges, we performed simulations in order to model the thermodynamic evolution of the system at given temperatures and concentration. This study allowed to roughly estimate the transition temperature between the phase decomposition and solid solution regimes, over the whole range of concentrations. Although there is no experimental data available on this topic, our results seem reasonable by analogy with some studies performed on Fe-Cr alloys.

Finally, first results with the application of an external magnetic field allowed us to investigate the dependence of Curie temperature on the field intensity in pure Fe and dilute Fe-Mn alloys, as well as the ratio of Mn atoms at the FM-Mn state over all Mn atoms, under various field intensities. The results suggest that the discrepancies identified in chapter 2 between experimental and theoretical works concerning the magnetic coupling between Mn and Fe magnetic moments in dilute bcc Fe-Mn alloys is not (only) caused by the use of magnetic fields in the experimental setups.

Such simulation of the evolution of bcc Fe-Mn alloys allows us to study the thermodynamic equilibrium states at any temperature and concentration, but it does not provide any information on the kinetic properties of the systems. As diffusion in Fe-alloys is generally ruled by vacancy-mechanism (successive vacancy-atom nearest-neighbor exchanges), it is necessary to parameterize the properties of a vacancy. In the following chapter, we propose a formalism to parameterize the formation and migration properties of a vacancy, in order to simulate self- and solute diffusion.

Chapter 4

Self- and Mn diffusion in bcc Fe

In this chapter, we propose a continuous approach in order to study the formation and the migration of vacancies and the diffusion in bcc Fe as functions of temperature. Especially, the importance of the use of quantum statistics instead of classical statistics in Monte Carlo simulations is estimated. We first validate our approach on the relatively simple case of pure Fe. The validity of the widely used Ruch model is discussed. Finally, the diffusion of a Mn solute in bcc Fe is studied.

In Fe-systems, as in many other metallic systems, self-diffusion and most substitutional solute diffusion occur via vacancy-mechanism, which consists in consecutive nearest-neighbor atom-vacancy exchanges.

Ab-initio calculations allow to determine the formation and migration properties of a vacancy in bcc Fe at the electronic ground-state [150, 32, 39, 123, 178]. More generally, such properties are quite straightforward to determine in magnetically ordered systems, as there are a countable number of distinct configurations to consider. When taking into account the effects of temperature, one has to cope with magnetic disorder. Methodologies such as the Disordered Local Moment (DLM) approach allow to model paramagnetic systems by generating ideal random spin configurations, ensuring a negligible correlation between the spins [2, 3, 135]. As the magnetic short-range order (MSRO) is by definition neglected, this approach is limited to the study of the asymptotic high temperature behavior of the system. However, some studies [65, 31, 140] have proposed to study intermediate temperatures (for instance near the Curie temperature) using empirical models in order to interpolate the vacancy activation energy (knowing the low and high temperature asymptotic behaviors). In particular, the model proposed by Ruch and Girifalco [137] has widely been used in the literature in order to describe the temperature dependence of vacancy activation energy, which is partially due to the temperature dependence of the magnetic ordering.

Although this approach gives a plausible approximation of the temperature dependence of vacancy properties, it is difficult to study the influence of magnetic short range order on these properties, or to study vacancies in alloys. Indeed the model

only provides average properties for a given temperature, but any local magnetic or chemical state cannot be explicitly described.

In order to study the influence of magnetism on kinetic properties of Fe-based alloys, we propose a continuous approach which does not involve any averaging of magnetic properties in the determination of finite-temperature vacancy properties (magnetic local environments are explicitly considered in the simulations). It consists in parameterizing an effective interaction model with explicit magnetic and chemical variables in order to study the formation and the migration of vacancies as a function of temperature and in particular the effects of magnetic short range order near the magnetic transition temperature.

This chapter aims at validating the approach on pure Fe before considering the Mn solute diffusion in Fe. To do so, formation and migration properties of a vacancy in Fe but also self-diffusion properties are determined using our approach and the effect of various approximations or methodological variations are discussed, such as for instance the use of quantum statistics for low temperature Monte Carlo simulations, instead of classical statistics. Then, the same methodology is applied to the diffusion of a single Mn solute in bcc Fe.

4.0 State of the art

Since the mid-twentieth century, many efforts have been involved in the determination of vacancy properties in pure Fe. Indeed, the understanding of vacancy behavior in a given alloy is a fundamental step towards the determination of many materials properties [8].

Several studies [20, 66, 100] using tracer diffusion experiments obtained estimations of the diffusion activation energy in bcc Fe at various temperatures. This method consists in depositing a thin film of radioactive isotopes (of the same chemical species as the bulk, in our case Fe) at the surface of a polished sample. When the sample is heated, these radio-nucleides are involved in self-diffusion just like a regular bulk atom. Then the average displacement of these radio-nucleides is measured and the coefficient of self-diffusion D^* can be deduced. The diffusion activation energy at a given temperature is derived from this self-diffusion coefficient as it represents the slope of the $D^* = f(T)$ curve.

Vacancy properties can also be studied using positron annihilation experiments. This method allows to detect defects such as vacancies by measuring the spatial variations of the annihilation rate of positrons, which is linked to the local electronic density [29]. The vacancy concentration obtained from positron lifetime measurements leads to the vacancy formation energy.

Finally, resistivity recovery experiments also allow to study the properties of vacancies [104, 50]. The principle is that Fe samples are irradiated at cryogenic temperatures in order to generate displacement damage and immobilize the created defects. Then the sample goes through several annealing processes, while its microstructural

evolution is observed via resistivity measurements. The evolution of the resistivity allows to evaluate the mobility of the defects [50]. This methods is used to obtain the vacancy migration energy, along with other approaches such as internal friction experiments or magnetic after effect, for instance

These experimental approaches to measure vacancy properties are complementary as each provides a specific information.

Theoretical studies of a vacancy in systems presenting chemical order-disorder transitions were performed by Girifalco [48, 47, 49] considering the chemical disorder in $\beta-$ brass. The approach consists in considering a set of pair-interactions depending on the chemical species of both atoms. In this formalism, the formation of a vacancy induces $Z/2$ broken bonds, Z being the coordinance number, as the atom is virtually moved to the side of the system (where half of its bounds are conserved). Concerning the vacancy migration, Girifalco *et al.* define an alternative set of pair-interactions for an atom at the saddle-point (during its migration). The evolution of the vacancy migration energy with temperature is modeled as follows:

$$E^m(T) = E_0^m + C \cdot S^2 \tag{4.1}$$

where S is the long-range order parameter, C is a linear combination of the interaction parameters and $E^m(0)$ is the migration energy in a totally disordered system.

From there, the diffusion coefficient is expressed as a function of the activation energy in the fully disordered system as follows:

$$D = D_0 \cdot \exp(-\frac{Q_0 + \alpha S^2}{k_B T}) \tag{4.2}$$

where α is a linear combination of the pair-interaction parameters.

Ruch *et al.* [137] adapted this approach to the case of a magnetically disordered pure Fe system, considering the spin-up and spin-down atoms (in the approximation of the Ising model) as the two species, by analogy with Girifalco *et al.*. The evolution of the vacancy activation energy with temperature may then be expressed as a function of the activation energy in the fully paramagnetic system and the reduced magnetization (by analogy with the Bragg-Williams long range order parameter for chemically disordered systems). The Ruch model is explicited in the following expression:

$$Q(T) = Q_{PM} \cdot (1 + \alpha S^2) \tag{4.3}$$

where $Q(T)$ is the activation energy at temperature T, Q_{PM} is the paramagnetic activation energy, S is the magnetic order parameter (usually the magnetization) and α is an adjustable paramater.

Several recent theoretical studies [140, 31, 65] apply this approach in order to interpolate the evolution of the properties of a vacancy with temperature in magnetic systems. The principle is either to obtain the ferromagnetic activation energy

using DFT calculations and to extrapolate the temperature dependence using a α value of the literature [65], or to determine both the ferromagnetic activation energy (using DFT) and the paramagnetic activation energy (using for instance the spin-wave expansion or the DLM approach [31]) in order to interpolate the temperature dependence.

This approach presents however practical limitations. For instance, extracting the α parameter from the literature, as done by Huang *et al.* [65], is straightforward in the very documented case of pure bcc Fe. In the case of a specific alloy (with a specific concentration and a specific order), it requires to perform non-trivial tracer diffusion experiments on a sample with an identical structure. Concerning determination of Q_{PM}, it can be achieved by calculating separately the paramagnetic formation and migration contributions with DFT using the disordered local moment (DLM) approach [2, 3, 135, 43]. That method consists in modeling paramagnetic systems by adopting ideal random spin configurations, ensuring a negligible correlation between the spins.

Another approach allowing to study the properties of vacancies as a function of temperature is the spin-lattice dynamics [179, 173, 174]. In particular, a recent study of Wen *et al.* [174] provides a detailed analysis of the vacancy formation, migration and activation properties, showing the temperature dependence of the Gibbs energy, the enthalpy and the entropy of these properties. The approach of this paper is based on an EAM-type empirical interatomic potential while the magnetic interactions are represented with a Heisenberg model. The study also explicitly shows the phonons and the magnons contributions, in addition to the complete spin-lattice dynamics results (including the phonons-magnons coupling). The study also illustrates the differences induced by the use of quantum statistics instead of classical statistics. One of the major advantages of this approach is to take intrinsically into account the coupling between lattice and magnetic excitations. However, the use of (EAM-type) empirical interatomic potentials, which are extremely system-dependent and fastidious to parameterize, makes it difficult to eventually apply this method to alloys.

4.1 Vacancy formation and migration from DFT calculations

4.1.1 Vacancy properties in bcc Fe at magnetic ground-state

Fundamental properties concerning the formation and migration of vacancies in pure bcc Fe can be obtained using DFT calculations. In particular, the properties of a vacancy in ferromagnetic Fe (the ground-state) must be fully understood as this system serves as reference for the following study.

In order to determine the vacancy formation enthalpy in pure bcc Fe, a vacancy is inserted in an ideal 128-atom bcc Fe system by removing one of the atoms. The system is fully-relaxed (system volume and position of the atoms). The presence of the vacancy induces noticeable lattice distortions, namely the local lattice constant goes from 2.832 Åin the bulk to 2.737 Åaround the position of the vacancy. Atomic

positions relaxation induced by the vacancy must then be taken into account when performing such calculations. Also, if the volume is not relaxed, a -8.7 kbar residual pressure, resulting in a 0.0065 eV difference is noticed compared to the non-relaxed calculations, which is negligible.

We note that the presence of a vacancy has an effect on surrounding magnetic moments. Compared to the nominal bulk value of 2.21 μ_B, the nearest-neighbor atoms of the vacancy exhibit a magnetic moment magnitude of 2.41 μ_B while its next nearest-neighbors show a magnitude of 2.06 μ_B. From the $3nn$ distance, the effect of the vacancy on Fe atoms magnetic moment is negligible, as seen in Fig. 4.1.

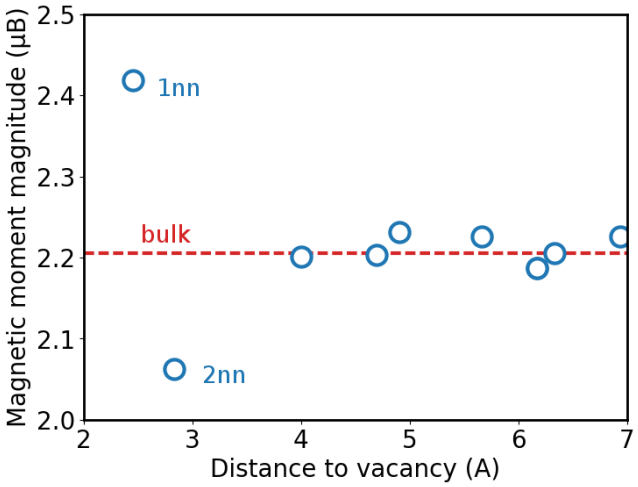

FIGURE 4.1: Magnetic moment magnitude of Fe atoms as a function of the distance to the vacancy. The bulk reference value is given as the red dotted line. The influence of the vacancy on surrounding magnetic moments is mainly contained within the two nearest-neighbor shells.

We have performed a Voronoï tessellation of the system which shows that the nearest-neighbors of the vacancy have a significantly higher Voronoï volume than bulk atoms while the next-nearest neighbors of the vacancy have a Voronoï volume slightly lower than the bulk atoms.

As seen in Fig. 4.2, the variation of the magnetic moments seems fully correlated to the variations of the local charge induced by the presence of the vacancy. Both magnetic moments and local charges are obtained by integrating the Fe PDOS. Although the local charge highly depends on the integration criterion, it is still possible to compare the relative values in order to evaluate its variation.

The vacancy formation enthalpy is determined using the expression described in equation 1.9 of the method chapter (see section 4.1). We find a value of 2.201 eV, in good agreement with the literature as theoretical studies (in which the ferromagnetic state properties are calculated via DFT) report values between 2.13 and 2.23 eV [65, 31, 140, 32, 123]. Our result also agrees with an experimental positron annihilation study [29] reporting 2.0 ± 0.2 eV. Concerning the migration enthalpy, our NEB calculations (see section 4.1 of the method chapter) lead to 0.69 eV, also in good agreement

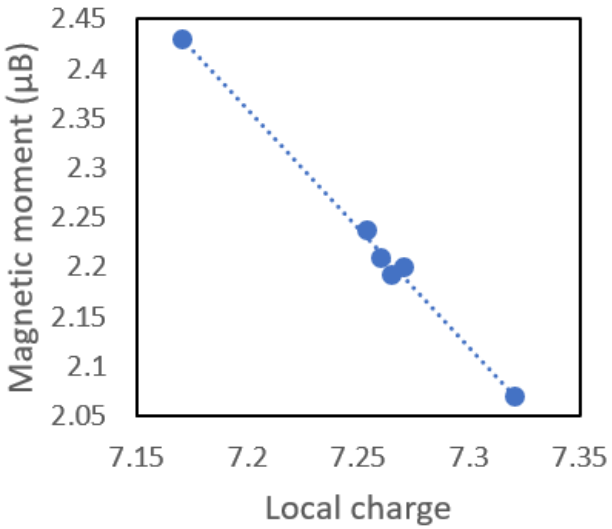

FIGURE 4.2: Magnetic moment magnitude of Fe atoms as a function of the local charge. Although the value of this local charge depends on the integration criterion, the relative value shows a clear trend.

with previous studies [39, 65, 31, 140, 159].

Using the frozen phonon method described in section 1.1.7, the jump attempt frequency and the vacancy formation entropy were calculated. However, determining these values from DFT calculations is known to provide very inaccurate results, as the numerical values highly depend on calculation parameters such as the elementary atomic displacement, the system size, etc... For instance, between constant pressure and constant volume calculations, the formation entropy varies from 3.26 to 4.80 k_B and the jump attempt frequency varies from 12.59 to 12.92 THz. The effect of this uncertainty is discussed in section 4.4. Fig. 4.4 and 4.3 give an insight on the results dispersion between various literature studies. No experimental study has ever been able to determine this value, while theoretical works give very dispersed results. The distinct studies seem to agree on the fact that the vacancy formation entropy is located between 1 and 5 k_B, while the attempt frequency is found between 10^{12} and 10^{14} Hz.

4.1.2 Influence of the magnetic structure on vacancy properties

In order to evaluate the influence of the bulk magnetic structure on the vacancy formation and migration enthalpies, analogous calculations are performed with various magnetic structures, both ordered (simple, double and quadruple layer antiferromagnetic) and disordered (collinear magnetic random configurations). These calculations are done with two distinct paradigms concerning the atomic positions relaxation. The most approximated one consists in using the relaxed atomic configuration of the corresponding ferromagnetic system. This approach allows to take into account the lattice distortions induced by the vacancy or the migrating atom, but without considering the displacements induced by the specific magnetic ordering.

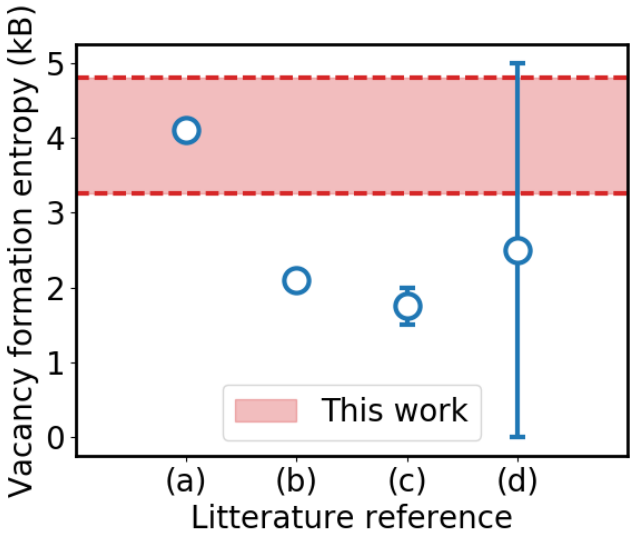

FIGURE 4.3: Comparison of the vacancy formation entropy obtained in this study compared to the values found in the literature: (a)[98] using the DFT frozen phonons method; (b)[59] using the determinant method with a Chang-Graham potential; (c)[131]; (d)[145] using positrons annihilation.

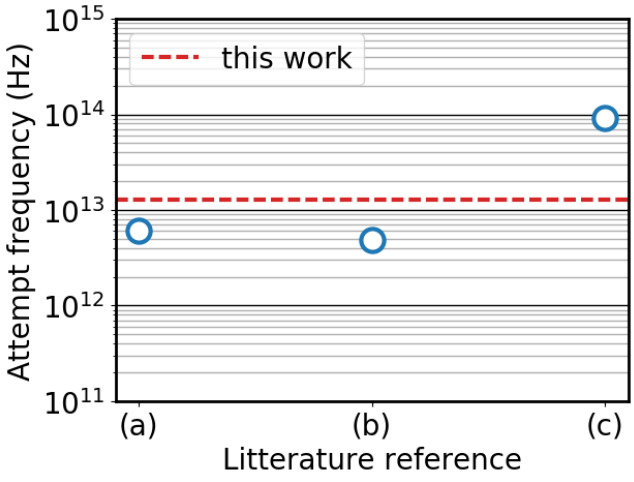

FIGURE 4.4: Comparison of the vacancy jump attempt frequency obtained in this study compared to the values found in the theoretical literature: (a)[107] simply considering the Debye frequency of α-iron; (b)[33] using the frozen phonons approach with the Einstein approximation; (c)[169] using an empirical pair potential.

The second approach consists in fully relaxing the atomic structure for each distinct magnetic structure, which is more accurate but induces higher computational costs. As fully relaxed calculations of magnetic random configurations are computationally very heavy, the vacancy formation and migration enthalpies in magnetically disordered systems was computed using ideal ferromagnetic systems, with randomized collinear magnetic moments on the two nearest interaction shells of the vacancy.

In table 4.1 and 4.2 are summed up the formation and migration enthalpies obtained using both volume- and full-relaxation, as well as non-relaxed calculations for comparison. As expected, volume relaxation has a minor effect on formation and migration enthalpies in systems which have an equilibrium volume close to the one of FM bcc Fe. Concerning AF and NM systems, the volume-relaxation has a significant effect since the equilibrium atomic volume is very different than the one of FM bcc Fe. (FM: 11.36Å^3, AF: 10.89Å^3 and NM: 10.48Å^3).

We note that in the case of magnetically disordered systems, the non-relaxed calculations exhibit a residual pressure systematically inferior to 10kBar, which we estimate to be a reasonable error-bar.

As shown in Tables 4.1 and 4.2, differences can be noticed between volume-relaxed and fully-relaxed calculations (at most 0.4 eV for formation and 0.2 eV for migration) while the same energy hierarchy between various magnetic orders is conserved. As the difference is not negligible, two distinct models parameterized with each dataset are compared in the following sections.

In the case of migration energy, it can be noticed in Table 4.2 that some values are negative. Despite the semantic issue of dealing with negative "barriers", these values have a physical meaning, being that the energy of the system is higher when all atoms are in a stable lattice position compared to having one atom at the migration saddle-point. This phenomenon only occurs in high energy magnetic configurations (such as antiferromagnetic for instance). We have checked that including or not these values in the fitting dataset has a negligible effect on the resulting parameters. Also, these high energy configurations have an extremely low probability of happening within the Monte Carlo simulation. Thus, there is no reason to expect such negative migration energies in the simulations.

In order to better understand the effect of the local magnetic order on the vacancy formation, we calculate for each magnetic configuration, the $1nn$ spin pair-correlation function of the atom which is replaced by a vacancy. The spin pair-correlation function I_{PC} is calculated using the following expression:

$$I_{PC} = \sum_{j}^{Z} \frac{\mathbf{M}_0 \cdot \mathbf{M}_j}{M_0 M_j} \tag{4.4}$$

where Z is the coordination number (here $Z = 8$), $\mathbf{M}_j$ is the magnetic moment of the $j-$th atom, M_j is its magnitude and the index 0 is associated to the concerned atom which is to be replaced by a vacancy.

Relaxation	FM	AFQ-1	AFQ-2	AFD	AF	NM	Disordered
Non-relaxed	2.201	1.694	2.290	1.899	1.265	1.007	1.406 - 1.979
Volume-relaxed	2.201	1.758	2.382	1.861	0.939	0.573	-
Fully-relaxed	2.201	1.496	2.122	1.604	-	-	1.228 - 1.484

TABLE 4.1: Formation energy of a vacancy in bcc Fe for various magnetic states. Non-relaxed means that the volume and the atomic positions of the systems are those of FM bcc Fe, volume-relaxed means that the volume of the system is relaxed but the atomic positions are those of FM bcc Fe and finally fully-relaxed means that the volume and the atomic positions are relaxed. AFQ-1 and AFQ-2 stand for anti-ferromagnetic quadruple layer with the vacancy being respectively near (AFQ-1) and far (AFQ-2) from the magnetic domain wall.

Relaxation	FM	AFQ-1	AFQ-2	AFD-1	AFD-2	AF	NM	Disordered
Non-relaxed	0.685	0.469	0.171	0.281	0.296	-0.427	0.345	-0.277 - 0.598
Volume-relaxed	0.685	0.794	0.171	0.457	0.386	-0.255	0.137	-
Fully-relaxed	0.685	0.719	0.092	0.280	-	-	-	-0.354 - 0.615

TABLE 4.2: Migration energy of a vacancy in bcc Fe for various magnetic states. Non-relaxed means that the volume and the atomic positions of the systems are those of FM bcc Fe, volume-relaxed means that the volume of the system is relaxed but the atomic positions are those of FM bcc Fe and finally fully-relaxed means that the volume and the atomic positions are relaxed. AFQ-1 stands for a migration inside a magnetic domain (between layers 2 and 3 out of 4) while AFQ-2 stands for a migration between two magnetic domains. AFD-1 stands for a migration inside a magnetic domain while AFD-2 stands for a migration between two magnetic domains.

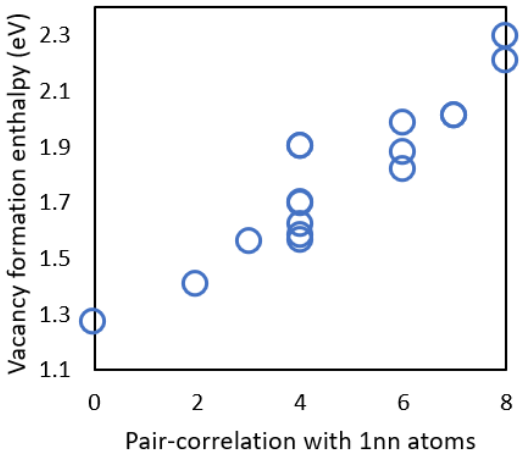

FIGURE 4.5: Correlation between the vacancy formation energy and the spin pair-correlation between the atom (which is replaced by a vacancy) and its nearest-neighbors. In the X-axis, 0 means that all the nearest-neighbors have an opposite spin to the deleted atom, while 8 means that the first interaction shell is fully ferromagnetically coupled with this atom.

As shown in Fig. 4.5, the formation energy of a vacancy seem to be highly correlated with the local magnetic environment. This behavior is quite expected since the ferromagnetic order is the most stable. It is then more difficult to form a vacancy in ferromagnetic bcc Fe. To the contrary, the creation of a vacancy is more favorable where there is the least ferromagnetic interaction.

To conclude, not only has the presence of a vacancy a noticeable effect on the surrounding magnetic moments of Fe atoms, but the magnetic state of the system has a significant impact on the formation and migration enthalpies of a vacancy. We propose to parameterize an effective interaction model with explicit magnetic and chemical variables in order to study the formation and the migration of vacancies as a function of temperature and in particular the effects of magnetic short range order near the magnetic transition temperature.

4.2 Vacancy formation with the interaction model

4.2.1 Model parameterization

The modeling of vacancies in an Heisenberg-like model is not trivial. In the easiest way, as adopted in a recent study [140], the presence of a vacancy is modeled by deleting an atom, it is then simply characterized by the absence of the interactions related to this atom. Such straightforward modeling may lead to an underestimation of the influence of the vacancy on its magnetic environment. In order to model the formation of vacancies, it is possible to make the interaction parameters dependent on the presence or not of a vacancy. Based on the results obtained concerning the effects of a vacancy on the surrounding atoms magnetic moment magnitude, our

approach consist in parameterizing the presence of the vacancy using distinct (A_i, B_i) on-site parameters to describe the magnetic state of atoms nearest or next-nearest neighbors of a vacancy. The complete Hamiltonian of the system is given in equation 4.5.

$$H = \sum_{i}^{N} A_i M_i^2 + B_i M_i^4 + \sum_{i}^{N}\sum_{n}^{P}\sum_{j}^{Z} J_{ij}^{(n)} \mathbf{M}_i \cdot \mathbf{M}_j + \sum_{i}^{N}\sum_{n}^{P}\sum_{j}^{Z} V_{ij}^{(n)} \tag{4.5}$$

where P is the maximum range of interactions in terms of neighbor shells, Z is the number of neighbors of each interaction range and $\mathbf{M}_i$ is the magnetic moment of the ith atom, M_i is the corresponding magnitude, and $V_{ij}^{(n)}$ represent the chemical pair-interaction between species of atoms i and j, at range n.

This approach allows to keep a unique set of pair-interaction parameters while modifying the effective interaction energy of the atoms surrounding the vacancy (since their magnetic moment magnitude changes). We believe that this approach is a reasonable compromise between the proper modeling of the vacancy and the complexity of the model.

As described in section 4.1.2, random magnetic structures have been modeled with two distinct approximations. The atomic positions are either relaxed depending on the magnetic structure, or the ferromagnetic atomic configuration is conserved (in both cases, the positions relaxations due to the presence of vacancy is considered). In order to evaluate the effects of considering or not such position relaxations, the model was fitted to both datasets, separately. We note that the parameters of the two models are deviating by less than 10%.

Contrary to DFT calculations, Monte Carlo simulations do not allow to determine the vacancy formation energy by directly creating a vacancy and calculating the induced ΔF. Indeed, the energy noise is too important to obtain consistent results this way. Instead, we propose an indirect approach in order to calculate the vacancy formation free energy as a function of temperature via Monte Carlo simulations, by determining the relative vacancy equilibrium between a system at finite temperature and the equivalent system at ground-state. The principle of this approach is detailed in the section 1.2.4 of the method chapter.

In practice, these Monte Carlo simulations were performed on 16000 atoms systems (20x20x20 bcc unit cells). For each temperature, the thermal equilibrium is first reached by performing 5.10^8 spin-MC steps (using the Metropolis algorithm). Once the system is at thermal equilibrium, a vacancy is created by removing a random atom and by updating the magnitude of its nearest- and next nearest-neighbors with the corresponding equilibrium magnitude (the equilibrium magnitude changes because of the distinct A_i and B_i on-site parameters). Then the vacancy is exchanged (using the Metropolis algorithm) with random atoms among both S_1 and S_2 systems (nomenclature given in section 1.2.4). In order to ensure the convergence of the relative vacancy concentration between the two systems, 10^7 vacancy exchanges are performed. In between the vacancy exchange attempts, 100 random spin-MC steps

are performed, around the vacancy up to its 5nn shell, in order to better explore the phase-space and to cancel the magnetic bias induced by the exchanges. Indeed, the S_2 system being kept perfectly ferromagnetic, the continuous exchanges between the two systems tends to create a ferromagnetic order in the S_1 system. This bias is totally handled by performing 100 spin-MC steps for each vacancy exchange attempt.

4.2.2 Results and discussions

The orange curve in Fig. 4.6 shows the results obtained with this approach. We note that both models (with and without atomic relaxations) lead to the exact same curve. The effect on formation free energy of considering the atomic positions relaxation due to the magnetic disorder is negligible. As can be noticed, the formation free energy (the magnetic free energy of vacancy formation) decreases with temperature, following the decrease of the magnetization. It seems legitimate as the low temperature ferromagnetic order stabilizes the structure and tends to prevent the vacancy formation, while the progressive loss of the ferromagnetic order with temperature weakens the structure and facilitate the vacancy formation. Above T_c, although the magnetization equals to 0, the formation free energy does not sharply falls to the asymptotic paramagnetic value, but instead decreases smoothly up to 1200K. We believe that this feature is caused by the residual magnetic short-range order, which is shown in section 3.0.1 of chapter 3.

As described in chapter 3 and in the literature [12], the temperature dependence of the average magnetization is very sensitive to the consideration of the Bose-Einstein distribution instead of the Boltzmann distribution in the Monte Carlo simulations. Since we observe that the vacancy formation free energy seems to depend on the magnetization, it is important to evaluate if the use of quantum statistics has an impact on vacancy properties.

The blue curve in Fig. 4.6 shows the results of similar calculations, except using the Bose-Einstein distribution (using the η function determined in chapter 3). The difference between the two curves is significant, which shows that quantum statistics are required to accurately predict the temperature dependence of vacancy formation free energy from Monte Carlo simulation, over the $T < T_C$ temperature range.

Concerning the low temperature limit of the vacancy formation free energy, the model reproduces the value obtained with DFT calculations in the FM regime (2.201 eV). Concerning the high temperature limit, most theoretical studies of the literature report values between 1.77 and 1.98 eV using either Spin-Lattice Dynamics [174] or the Ruch model with the DLM approach [65, 31], in good agreement with the experimental results of DeSchepper *et al.* [29] (1.78 ± 0.1 eV, at 1200K). However, one theoretical study [140] reports a surprisingly low value of the paramagnetic formation energy of 1.54 eV, despite describing the paramagnetic state using the DLM approach (as in [65] and [31]). Concerning our work, we obtain a formation free energy of 1.99 eV at the paramagnetic limit using our approach. Despite being on the

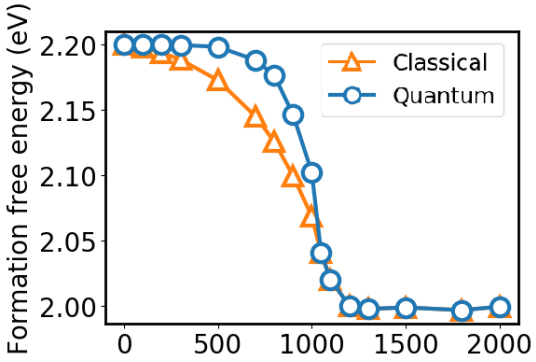

FIGURE 4.6: Comparison of the vacancy formation free energy obtained from Monte Carlo simulation using classical (orange) and quantum (blue) statistics

higher limit of the literature range, this value is in reasonable agreement with most studies.

In this work, we are considering the 2000K equilibrium magnetic configuration as "paramagnetic state". It is a highly non-collinear magnetic state, where the average magnetic moment is 0 and where the residual magnetic short-range order is approximately 0.05. We have checked at higher temperatures (up to 10000K, where both the magnetization and the magnetic short-range order are 0) that this residual magnetic short-range order has no significant effect on the vacancy formation free energy. We note that the paramagnetic state considered in the DFT-DLM approach is generally a collinear random magnetic state, which may induce eventual discrepancies between the two methods.

Concerning the evolution of the formation energy with temperature, the comparison of the spin-dynamics results of Wen *et al.* [174] with our results, both using quantum statistics, reveals an overall agreement. In both studies the formation energy decreases with temperature more and more sharply up to the Curie temperature, and then converges to the paramagnetic threshold. The difference between the ferromagnetic and the paramagnetic vacancy formation energies is certainly the most comparable quantity. The only available experimental value (to the best of our knowledge) is 0.21 eV via positron annihilation [29] with which we have an excellent agreement as our approach gives δE^f_{FM-PM} = 0.20 eV. The results of the theoretical literature go from δE^f_{FM-PM} = 0.15 eV using the DFT spin-wave method for the description of the paramagnetic state [31] to 0.32 eV [174] using Spin-Lattice Dynamics. However, we note that when $T < T_C$ the decrease rate obtained by Wen *et al.* [174] is larger compared to our results, which leads to a deviation at intermediary temperatures (typically between 400K and 900K) (for instance at 800K there is a 0.05 eV difference between both studies).

It is important to note that G^f_{mag} obtained from our Monte Carlo simulation not only contains the enthalpy H^f but also the magnetic configurational entropy S^f_{mag}.

The quantity G^f_{mag} plotted in Fig. 4.6 may then be expressed as follow:

$$G^f_{mag} = H^f - T \cdot S^f_{mag} \tag{4.6}$$

and may straightforwardly be decomposed into these two contributions using equations 4.7 and 4.8.

$$S^f_{mag} = -\frac{\partial G^f_{mag}}{\partial T} \tag{4.7}$$

$$H^f = G^f_{mag} - T \cdot \frac{\partial G^f_{mag}}{\partial T} \tag{4.8}$$

As can be seen in Fig. 4.7, although the formation free energy is monotonously decreasing with temperature, the magnetic entropy and enthalpy contributions both exhibit a peak near the Curie temperature. We note that both curves of Fig. 4.7 are in good agreement with the spin-dynamics results of Wen *et al.* [174], concerning both the position and the height of this peak. Indeed, concerning the enthalpy, our studies shows that the summit of the peak reaches 0.7 eV higher than the ferromagnetic formation enthalpy (0.6 eV in [174]). Concerning the magnetic entropy, Wen *et al.* find the maximum of the peak at $8k_B$ while our study gives $9k_B$. The fact that we obtain a higher peak is consistent with the fact that our study shows a slower decrease of the formation energy in the ferromagnetic regime, which involved a sharper decrease near the Curie temperature.

Please note that as our simulations are performed on rigid-lattice, we compare here with the spin-dynamics contribution of the work of Wen *et al.* [174], but this study also provides spin-lattice dynamics results which also include the lattice contribution and the coupling of both. Hence, the formation free energy, enthalpy and entropy presented here only represent the magnetic contribution of these quantities.

Sandberg *et al.* [140] also provide a graph of the vacancy formation enthalpy as a function of temperature. Although the quantitative comparison with our results isn't possible as the enthalpy is given as a function of the J_0 parameter which numerical value isn't provided, the qualitative comparison reveals that the peak found in this study has a lower maximum than the one in our work, in regard to the ferromagnetic formation enthalpy.

4.3 Vacancy migration

4.3.1 Model parameterization

In order to simulate the vacancy migration free energy, our approach consists in fitting another interaction model, with the same formalism, for the saddle-point. The role of this saddle-point Hamiltonian is to model the energy barrier of the migration (see section 1.2.5 in the method chapter). As shown in the results of section 4.1.2,

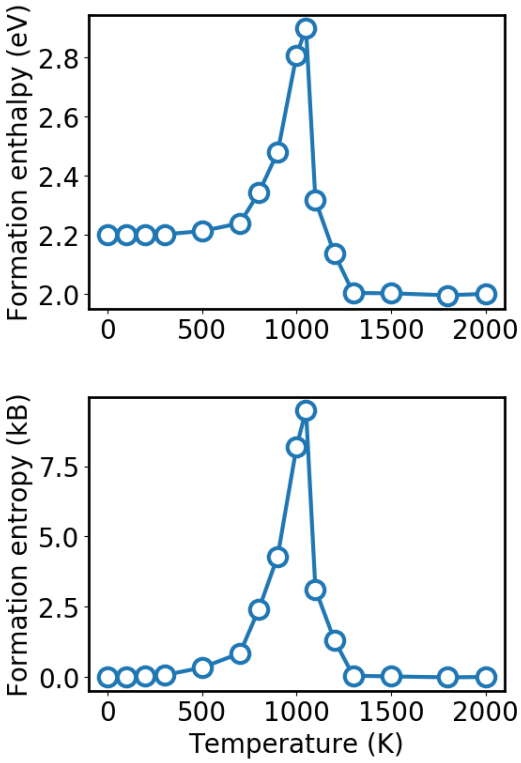

FIGURE 4.7: Vacancy formation enthalpy (a) and formation magnetic entropy (b), obtained from Monte Carlo simulations using equations 4.7 and 4.8.

the migration barrier should not be considered constant as it highly depends on the local magnetic state. To model this feature, the parameters are fitted on the migration barriers in various magnetic environments.

The total expression of the saddle-point Hamiltonian is shown in the following expression:

$$H^* = A^* M_0^2 + B^* M_0^4 + \sum_n^P \sum_j^Z J_{0j}^{*(n)} \mathbf{M_0} \cdot \mathbf{M}_j + \sum_n^P \sum_j^Z V_{0j}^{*(n)} \tag{4.9}$$

where P is the maximum range of interactions in terms of neighbor shells, Z is the number of neighbors of each interaction range and $\mathbf{M_0}$ is the magnetic moment of the saddle-point atom, M_0 is the corresponding magnitude and $J_{0j}^{*(n)}$ represent the magnetic pair-interaction between the saddle point atom and its neighbors (at range n). A^* and B^* are the magnetic on-site parameters of the saddle-point atom. In the present model are considered the interactions between the saddle-point atom and its neighbors up to the second nearest-neighbor shell. The migration energies are obtained by subtracting the energy of the system with an atom at saddle-point to the energy of the system with a vacancy in a lattice site (obtained with the model described in section 4.2).

Consistently with the calculations of formation free energy, the saddle-point model was fitted to two distinct datasets in order to evaluate the effect of considering the

relaxation of atomic positions due to the magnetic disorder. We note that the parameters of the two saddle-point models are deviating by at most 15%.

In practice, these Monte Carlo simulations were performed on 16000 atoms systems (20x20x20 bcc unit cells). For each temperature, the thermal equilibrium is first reached by performing 5.10^8 spin-MC steps (using the Metropolis algorithm). Once the system is at thermal equilibrium, a vacancy is created by removing a random atom and updating the magnitude of its nearest- and next nearest-neighbors with the corresponding equilibrium magnitude. From this point, the migration is simulated performing atomic jumps of the vacancy's nearest-neighbors. When using the residence time algorithm, 10^6 atomic-MC steps are performed in order for the vacancy to visit a sufficient number of magnetic environments. Using the Metropolis algorithm, 10^6 atomic-MC steps in the high-temperature domain (higher than 800K) gives similar results as the residence time algorithm. However, at low temperature the extremely low jump success rate induces insufficient statistics when using the Metropolis algorithm. Between each atom-vacancy exchange, 100 spin MC steps are performed among the whole system, and 500 more are performed among the five nearest-neighbor shells of the vacancy. This supplemental local relaxation allows to avoid any magnetic memory effect which may bias the random walk of the vacancy.

The fitting of these parameters is done twice, with volume-relaxed and fully-relaxed calculations in order to evaluate the impact of considering one approximation or the other. The comparison of the migration free energy evolution with temperature, calculated using both sets of parameters shows that the choice of approximation has no significant effect. It can be explained by the fact that the interaction model we are using may represent a stronger approximation than the consideration or not of fully-relaxation.

4.3.2 Results and discussions

The orange curve in Fig. 4.8 shows the results obtained with these simulations. As can be noticed, the migration free energy decreases with temperature, following the decrease of the total magnetization, although the decrease seems smoother than the formation free energy. Above T_c, the migration free energy decreases also more smoothly than the formation free energy, it reaches the paramagnetic asymptotic value around 2000K.

We note a very slight deviation between the models with and without atomic position relaxations (due to magnetic disorder). It leads to a difference of 0.03 eV at 1K while at higher temperatures, this difference is hidden in the statistical noise of the simulations. This deviation is very reasonable, considering the amount of computational time needed for these atomic position relaxations.

The same simulations are also performed with quantum statistics. The blue curve in Fig. 4.8 shows these results (using the same η function as in Chapter 3). The difference between the two curves is here also significant, which shows that quantum statistics are required to correctly predict both formation and migration

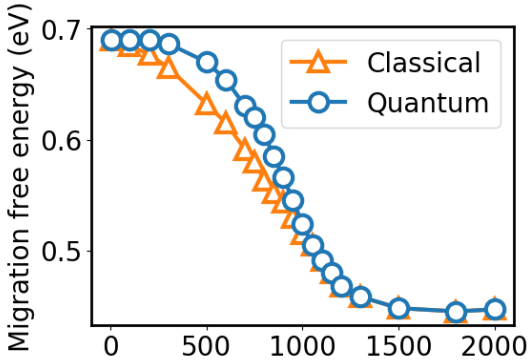

FIGURE 4.8: Comparison of the vacancy migration free energy obtained from Monte Carlo simulation with classical (orange) and quantum (blue) statistics

properties of vacancies from Monte Carlo simulation, all over the $T < T_c$ temperature range.

Concerning the low temperature limit of the vacancy migration free energy (0.685 eV), the model reproduces the value obtained with DFT calculations in the FM state. (using the NEB method, see section 4.1). Concerning the high temperature limit, literature theoretical studies (using the DLM approach) [65, 31, 140] report values between 0.40 and 0.43 eV in the paramagnetic regime while we obtain a migration free energy of 0.43 eV using our approach, which shows a good agreement. Using spin-lattice dynamics, Wen *et al.* [174] find 0.85 and 0.64 eV respectively in the ferromagnetic and the paramagnetic state.

Concerning the evolution of the migration energy with temperature, the comparison of the spin-dynamics results of Wen *et al.* [174] with our results, both using quantum statistics, reveals a significant discrepancy. Indeed, the spin-dynamics results provided by Wen *et al.* reveal a difference of 0.045 eV between the ferromagnetic and paramagnetic migration energies while using spin-lattice dynamics, e.g. including phonons contribution and the magnon-phonon coupling, the same study shows a 0.21 eV difference. In our study (without including phonons contribution and the magnon-phonon coupling), this energy difference equals to 0.26 eV while Sandberg *et al.* and Ding *et al.* respectively report 0.30 and 0.21 eV differences. In other words, the study of Wen *et al.* suggest that magnetism has a negligible influence on the evolution of the migration energy, which seems inconsistent with the DFT results.

Following the same method as in section 4.2.2, the migration free energy was decomposed into the enthalpy and the magnetic entropy. As can be seen in Fig. 4.9, the migration enthalpy and magnetic entropy contributions both exhibit a peak near the Curie temperature. Although no quantitative agreement can be expected with Wen *et al.* [174], since this study suggest that the magnetic contribution to the vacancy migration is negligible, both studies exhibit a peak of the magnetic entropy and the enthalpy near the Curie temperature.

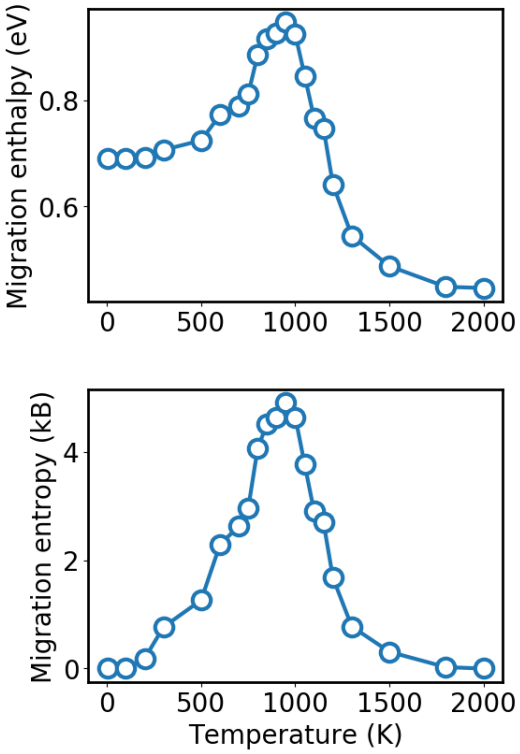

FIGURE 4.9: Vacancy migration enthalpy (a) and magnetic entropy (b), obtained from Monte Carlo simulations applying equations 4.7 and 4.8 to the case of migration (instead of formation).

4.3.3 Activation energy

The vacancy activation free energy, being the addition of the formation and the migration energies, is a fundamental property of materials as it captures the main properties of vacancies, but also because it is directly linked to self-diffusion (see section 4.4).

In the ferromagnetic regime (at the low temperature limit), we find an activation free energy of 2.89 eV by summing the formation and migration energies obtained so far. This results is in good agreement with the experimental literature which shows values between 2.63 and 3.10 eV using tracer diffusion experiments (see Table 4.4). Our result is also in agreement with the theoretical literature which shows results between 2.77 and 2.87 eV for the DLM + Ruch model approach [31, 65, 140] and 3.09 eV for the spin-lattice dynamics approach [174]. (see Table 4.4)

In the paramagnetic regime (at the high temperature limit), we find an activation free energy of 2.43 eV, which is in the range of the literature theoretical results going from 1.94 to 2.56 eV [65, 174, 31, 140]. We note that the particularly low value of 1.94 eV found by Sandberg *et al.* is directly linked to the low value of paramagnetic formation energy of 1.54 eV discussed earlier. The other theoretical values are between 2.41 and 2.56 eV [65, 174, 31]. Despite being at the lower limit of the range, our result is in reasonable agreement with experimental studies reporting paramagnetic activation energies between 2.48 and 2.92 eV obtained via tracer diffusion experiments

Reference	H^f_{FM} (eV)	H^m_{FM} (eV)	H^f_{PM} (eV)	H^m_{PM} (eV)
This work	2.20	0.69	1.99	0.43
Huang *et al.* [65]	2.23	0.64	-	-
Wen *et al.* [174]	2.24	0.85	1.91	0.64
Ding *et al.* [31]	2.13	0.64	1.98	0.43
Sandberg *et al.* [140]	2.17	0.70	1.54	0.40
Tapasa *et al.* [159]	-	0.65	-	-
DeSchepper *et al.* [29]	2.00	-	1.79	-

TABLE 4.3: Representative vacancy energetic properties of the literature. H^f_{FM} and H^f_{PM} represent the vacancy formation magnetic free energies in respectively ferromagnetic and paramagnetic state and H^m_{FM} and H^m_{PM} represent the vacancy migration magnetic free energies in respectively ferromagnetic and paramagnetic state.

[66, 17, 44, 53, 170, 20, 61, 69, 100, 84].

Certainly the most important feature to compare is the difference between the ferromagnetic and the paramagnetic activation energies, as it reveals in what extent does this quantity evolve over the whole temperature range. In our case, this difference is found to be ΔQ_{FM-PM} = 0.46 eV. It is comparable to the literature results as most values are found between 0.38 and 0.54 eV both in the theoretical and the experimental sides [66, 61, 100, 65, 31, 174], to the exception of an experimental study [69] showing 0.14 eV and a theoretical study [140] showing 0.89 eV.

From the values of vacancy activation free energy at magnetic ground-state and in the asymptotic high-temperature paramagnetic regime, it is possible to apply the Ruch model in order to interpolate the vacancy formation free energy at any temperature. Using our values of Q_{FM}, Q_{PM} and M, it results in a α=0.191 coefficient. Although the value of α may not be relevant to compare with literature data as it depends on the values of Q_{FM} and Q_{PM}, we note that our result is within the usual values found in the previous studies. As can be seen in Table 4.4, most values are located between 0.148 and 0.207 (both theoretical and experimental) [66, 61, 100, 65, 31, 174] to the exception of an experimental study [69] showing 0.056 eV and a theoretical study [140] showing 0.479 eV.

In order to evaluate the validity of the Ruch model (see section 4.0) at intermediate temperatures, the results of our calculations are plotted in the panel A of Fig. 4.10 along with the Ruch model obtained from our values of Q_{FM}, Q_{PM} and M. As can be noticed, the Ruch model gives an overall very accurate approximation of the vacancy activation free energy. When $T > T_C$, a slight difference between the two approaches is observed. Indeed, following the Ruch model, at any temperature above T_C, the activation free energy has the exact same value as the high-temperature paramagnetic limit. Using our approach, the residual magnetic short-range order (see Fig. 3.3 in chapter 3) above T_C induces a smoother temperature convergence of the activation free energy. In order to quantify the discrepancies, the root mean square difference

Reference	Approach	Q_{FM} (eV)	Q_{PM} (eV)	α	D_0
This work	theo.	2.89	2.43	0.191	1.8E-5
Huang *et al.* [65]	theo.	2.87	2.48	0.159	6.70E-5
Wen *et al.* [174]	theo.	3.09	2.56	0.207	-
Ding *et al.* [31]	theo.	2.77	2.41	0.149	-
Sandberg *et al.* [140]	theo.	2.77	1.94	0.479	8.46E-5
Tapasa *et al.* [159]	theo.	-	-	-	2.30E-5
Iijima *et al.* [66]	exp.	3.00	2.60	0.156	2.80E-4
Borg *et al.* [17]	exp.	-	2.92	-	1.20E-2
Geise *et al.* [44]	exp.	-	2.92	-	1.20E-2
Graham *et al.* [53]	exp.	-	2.48	-	2.00E-4
Walter *et al.* [170]	exp.	-	2.49	-	2.00E-4
Buffington *et al.* [20]	exp.	-	2.48	-	1.90E-4
Hettich *et al.* [61]	exp.	2.94	2.53	0.162	1.00E-4
James *et al.* [69]	exp.	2.63	2.49	0.056	2.00E-4
Luebbehusen *et al.* [100]	exp.	2.95-3.10	2.57-2.68	0.148-0.157	0.68-1.23E-3
Kucera *et al.* [84]	exp.	-	2.71	-	1.10E-3
DeSchepper *et al.* [29]	exp.	2.87	-	-	-

TABLE 4.4: Representative diffusion parameters of the literature. Q_{FM} and Q_{PM} represent the vacancy activation energies in respectively ferromagnetic and paramagnetic state. α is the coefficient that appears in the Ruch model, corresponding to $\alpha = Q_{FM}/Q_{PM} - 1$. D_0 is the pre-exponential factor of the self-diffusion coefficient. "theo." and "exp." respectively stand for theoretical and experimental approaches.

between the two approaches is calculated using the following expression:

$$RMS(Q) = \frac{\sqrt{\sum(Q - Q_{Ruch})^2}}{N} \tag{4.10}$$

where Q and Q_{Ruch} are the activation energies calculated using respectively our approach and the Ruch model. In Table 4.5, the results are shown for the activation free energy but also for the formation and the migration free energies. N is the number of data points. The root mean square difference between the two approaches represents 0.70% of the average activation free energy, which definitely shows the good agreement between both methods.

Quantity	Root mean square difference
Q	0.70% (1.28%)
E^f	0.75% (1.68%)
E^m	0.96% (1.83%)

TABLE 4.5: Root mean square difference of the activation, formation and migration free energies between the Ruch model and our approach, calculated using the expression 4.10. The values between parenthesis represent the largest difference of each quantity.

Considering separately the vacancy formation and migration energies, our results are also compared to the Ruch model, as illustrated respectively in panels B and C of Fig. 4.10. Concerning the formation free energy, the Ruch model and our method show some slight discrepancies in the domain below T_C. Indeed, the formation free energy obtained via the Ruch model decreases more rapidly with temperature than our results. However, when $T > T_C$, both approach give similar results, as the magnetic short range order doesn't seem to have a significant effect on the vacancy formation free energy. Concerning the evolution of the migration free energy as a function of temperature, both models give similar results below T_C, while the domain beyond T_C shows significant differences, that we believe to be caused by the magnetic short-range order. As shown in Table 4.5, the average difference between the two methods represents respectively 0.75% of the average formation free energy and 0.96% of the average migration free energy.

From these results, it seems clear that the Ruch model allows a very good approximation of the temperature evolution of activation, formation and migration energies in pure Fe. However, it should be noted that the Ruch model requires to know the evolution of the magnetization as a function of temperature (for instance from experimental literature) and it implies to either use a literature value of the α parameter, or to determine the activation free energy in both ferromagnetic and paramagnetic states. Such values can easily be found in the case of pure bcc Fe as it has been heavily studied for decades, while it may be challenging in a given alloys at a given concentration and with given chemical short-range orders. Hence the Ruch model isn't easily transferable to the study of vacancy properties in alloys, while our

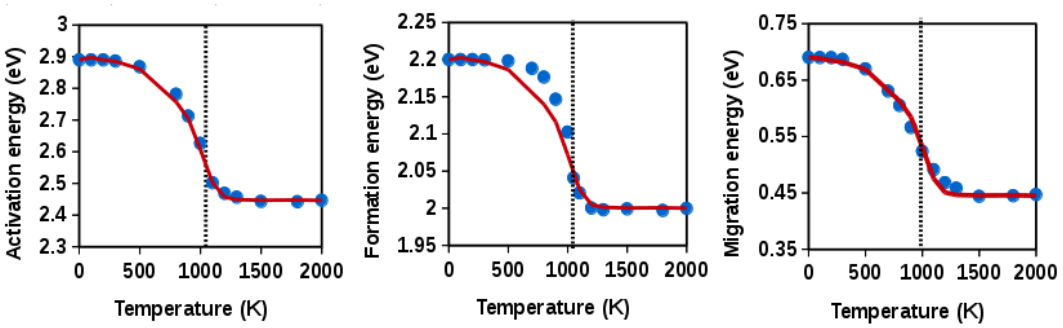

FIGURE 4.10: Vacancy activation (A), formation (B) and migration (C) free energies obtained from Monte Carlo simulation with quantum statistics (blue) compared to the Ruch model (red) applied to our values of Q_{FM}, Q_{PM} and M

approach is quite adaptable considering that it only requires to fit the parameters of the interaction model on DFT calculations.

4.4 Self-diffusion in bcc Fe

The ability to properly predict vacancy properties in bcc Fe allows to determine the self-diffusion coefficient by performing Monte Carlo tracer diffusion simulations, considering each atom of the system as a tracer [117, 111]. The principle and practical details of this approach are described in the section 1.2.6 of the method chapter. Although this approach requires heavy calculations in order to obtain a statistically significant mean square displacement, it has the advantage to directly take into account any eventual effect of magnetic disorder and short-range order in the diffusion coefficients (and atomic disorder and short-range order for alloys).

As we have shown that the use of Bose-Einstein distribution has a noticeable effect on vacancy formation and migration energies, we believe it is more consistent to determine the self-diffusion coefficient also using quantum statistics.

In practice, these Monte Carlo simulations were performed on 16000 atoms systems (20x20x20 cubic unit cells). For each temperature, the thermal equilibrium is first reached by performing 5.10^8 spin-MC steps (using the Metropolis algorithm). Once the system is at thermal equilibrium, a vacancy is created by removing a random atom and updating the magnitude of its nearest- and next nearest-neighbors.

From this point, the diffusion is simulated by performing atomic jumps of one of the nearest-neighbor atoms of the vacancy. When using the residence time algorithm, 10^9 atomic-MC steps are performed, which allow to obtain a mean square displacement of at least 1000 jump-distances. If using the Metropolis algorithm, the high-temperature domain is equally easy to study as the mean square displacement reaches easily significant statistics. However, low-temperature calculations of tracer diffusion with Metropolis algorithm are much more difficult than with the residence time algorithm. For instance at 100K, 10^9 atomic-MC steps are required to reach a mean square displacement value of 1 jump-length (which is very insufficient). In

between these atomic jumps, 100 spin MC steps are performed among the whole system, and 500 more are performed among the five nearest-neighbor shells of the vacancy, in order to prevent any magnetic memory effect which may bias the random walk of the vacancy.

The combination of these two approaches allows to calculate the temperature dependence of the correlation factor f_0, by considering the ratio between diffusion coefficients obtained respectively via tracer diffusion and the analytical approach. We use this method to make sure that $f_0 = 0.727$. Any deviation from this value suggests an insufficient magnetic relaxation between the atomic jumps.

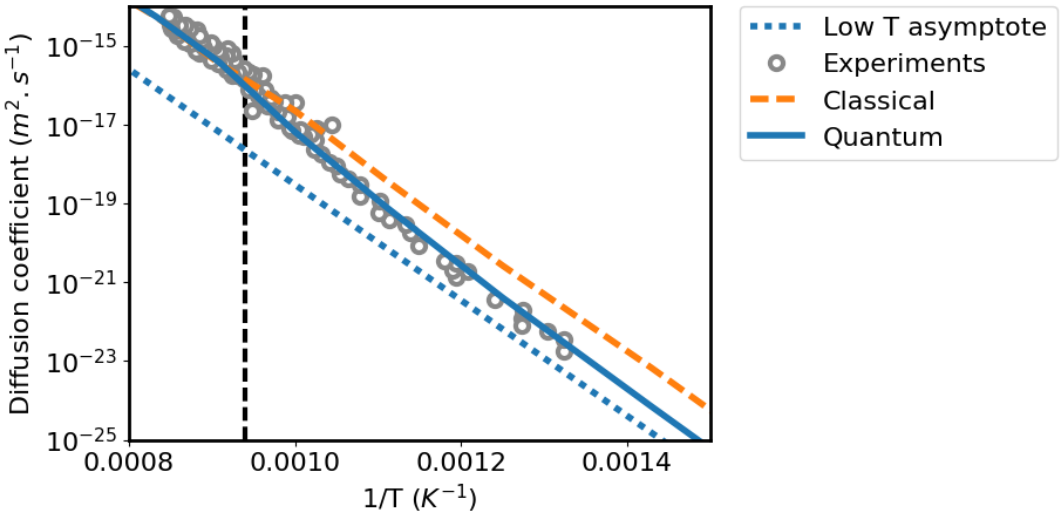

FIGURE 4.11: Self-diffusion coefficient as a function of temperature obtained via Monte Carlo simulations using the Bose-Einstein distribution (blue solid line) or the Boltzmann distribution (orange dashed line) compared with experimental results [53, 170, 20, 69] (grey circles). The blue solid line and the blue dotted line shows the low temperature asymptote of the blue solid line.

The self-diffusion coefficient obtained via Monte Carlo simulations is shown in Fig. 4.11. As discussed in section 4.1.1, the DFT determination of jump attempt frequency and vacancy formation entropy have large uncertainties, depending on computational details. As both these values intervene in the pre-exponential factor of the diffusion coefficient, the self-diffusion curve contains significant vertical errorbars. We note however that this uncertainty only leads to an eventual rigid shift of the curve, but doesn't affect its shape. In this work, we consider the same D_0 prefactor in ferromagnetic and paramagnetic states.

The solid blue curve in Fig. 4.11 shows the results of our approach, using quantum statistics. As can be seen, solid line and the experimental grey circles are in good agreement. Not only our asymptotic values of Q_{FM} and Q_{PM} are in the range of experimental results, but also the acceleration of self-diffusion around the Curie temperature is correctly predicted. Especially, this acceleration is intrinsically predicted with our approach, without involving an empirical drop of the activation free energy near T_C.

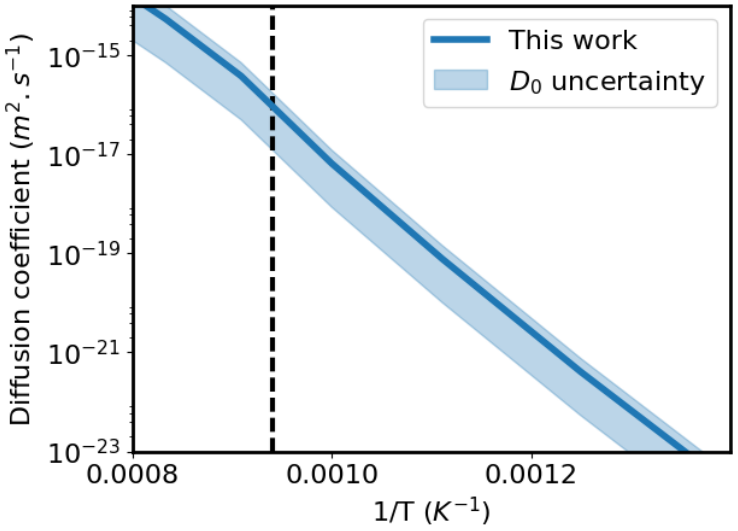

FIGURE 4.12: Self-diffusion coefficient as a function of temperature obtained via Monte Carlo simulations using the Bose-Einstein distribution (blue solid line). The light blue band shows the vertical uncertainty of the blue solid line.

Fig. 4.11 also shows the results obtained with classical statistics (orange dashed line), which confirms that using the Boltzmann distribution in the MC simulations doesn't allow to faithfully model the temperature dependence of self-diffusion, as the deviation of Arrhenius law is highly underestimated. Finally, Fig. 4.11 also shows the low temperature asymptote of self-diffusion using quantum statistics, in order to better identify the deviation from Arrhenius law near T_C.

We note that in earlier studies focused on W and Ta metals [141, 142], it was shown that electronic excitations may significantly contribute to the diffusion coefficient. According to a recent study [65] on self-diffusion in bcc Fe, this electronic contribution is relatively small, inducing an increase of the self-diffusion coefficient by at most a factor 3. Although we did not determine this electronic contribution by ourselves, we choose as a D_0 the average between the value we obtained with constant volume frozen phonons calculations, and three times this value (to take into account the aforementioned uncertainty). The error bars shown in the Fig. 4.12 include this factor 3 of uncertainty, but also the uncertainty due to computational details. For instance, considering constant pressure instead of constant volume calculations changes the D_0 from $9.1 \cdot 10^{-5}$ to $2.0 \cdot 10^{-5}$.

Our final value of D_0, based on constant volume calculations and including the uncertainty induced by electronic entropy, is $1.8 \cdot 10^{-4}$. By comparison with the values of D_0 found in the literature (see Table 4.4), our value of D_0 is in good agreement with several experimental studies [53, 170, 20, 69].

Fig. 4.13 shows the comparison between our approach and the Ruch model (applied to our values of Q_{FM}, Q_{PM} and $M(T)$). As can be seen, both methods give almost the same results, which is not surprising as we have shown that the temperature dependence of the activation energy is very similar with both approaches. This

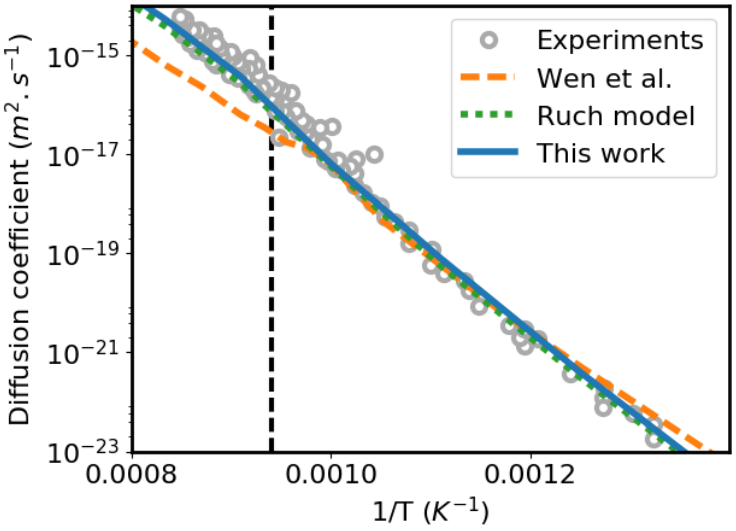

FIGURE 4.13: Self-diffusion coefficient as a function of temperature obtained via Monte Carlo simulations (blue solid line) and using the Ruch model (green dotted line), compared with experimental data [53, 170, 20, 69] (grey) and the spin-lattice dynamics approach (orange dashed line) in [174] using the quantum statistics.

observation definitely validates the use of the Ruch model for the modeling of self-diffusion in bcc Fe. However, as explained earlier, it does not provide any conclusion towards the applicability of this model to solute diffusion.

It is also important to compare our results with the work of Wen *et al.* using spin-lattice dynamics to predict the self-diffusion of Fe, as both methods provide the temperature evolution of self-diffusion without any empirical temperature dependence (contrary to the Ruch model). As can be seen in Fig. 4.13, the spin-lattice dynamics approach qualitatively captures the phenomenon. The orange dashed line shows an increasing self-diffusion coefficient with temperature, presenting a slight acceleration near T_C followed by a change of slope. However, the agreement is not quantitative between the orange curve and the experimental grey dots, which certainly depends on the empirical interatomic potential which is used.

4.5 Mn diffusion in bcc Fe

In a ferromagnetic system such as bcc Fe, most solute diffusion coefficients show a sudden acceleration and therefore a deviation from the Arrhenius law around the Curie temperature of Fe. This feature observed in many experimental studies [156, 133, 91, 139] is known to be related to the magnetic transition of Fe. As we have shown in the previous sections for the case of self-diffusion in Fe, the transition from the ferromagnetic regime to the paramagnetic regime induces a significant decrease of the vacancy formation and migration free energies. However, some available experimental studies concerning the diffusion of Mn in bcc Fe suggest that this acceleration of solute diffusion near T_C does not seem visible.

Early experimental studies [75, 99] performed between 900 and 1200K indeed suggest a perfectly Arrhenian behavior. The limited temperature range of these two studies make any definitive conclusion somehow difficult.

Recently, S. Divinski has kindly provided us some unpublished experimental tracer diffusion results which seem to confirm the absence of a "kink" near T_C in the temperature evolution of the Mn diffusion coefficient in bcc Fe.

To the best of our knowledge, only one theoretical study has attempted to predict the temperature evolution of the Mn diffusion coefficient in bcc Fe. Messina *et al.* [108] have reported that their approach does not allow to predict correctly the experimental diffusion coefficient of Mn, which is different from the other solutes.

In order to provide a prediction from the modeling point of view and to better understand these observations, we propose in this section to study the diffusion of a single Mn atom in pure bcc Fe in the presence of a vacancy, to mimic the thermal diffusion of Mn in the extremely dilute Fe-Mn system.

4.5.1 Mn-vacancy interaction in FM bcc Fe

Before modeling the Mn diffusion in bcc Fe, the first step is to study the properties of a vacancy in the presence of a single Mn atom in bcc Fe. To do so, we have performed DFT calculations including one Mn solute and one vacancy in a pure Fe 128-atom system. All the DFT approximations adopted here are the same as in previous sections.

We have checked that in the FM state, Mn-vacancy interaction is negligible beyond a 2*nn* distance, we therefore apply the LeClaire model in an existing analytical form. Each key configuration of the LeClaire 10-frequency model was studied using DFT, both in FM bcc Fe and in 9 distinct disordered magnetic structures (actually locally disordered, in the two nearest-neighbor shells of the vacancy). For each atomic configuration, the equilibrium volume of pure Fe is conserved and the atomic positions are relaxed in the FM state. For all saddle-point configurations, NEB calculations are performed at constant volume. The disordered spin structure calculations are then performed using the atomic positions of the corresponding ferromagnetic system.

Mn-Vac distance	1*nn*	2*nn*
AF-Mn in FM Fe	0.15	0.11
FM-Mn in FM Fe	-0.12	-0.06
Disordered (average)	0.01	-0.03

TABLE 4.6: Binding energies (in eV) between a Mn solute and a vacancy, at 1*nn* and 2*nn* distances (further interactions are considered negligible). The two first rows show the results in ferromagnetic Fe with the Mn moment coupled either antiparallel or parallel to the moments of Fe atoms. The last row shows the average results in magnetically disordered configurations.

Barrier	ω_2	ω_3	ω_4	$\omega_{3'}$	$\omega_{4'}$	$\omega_{3''}$	$\omega_{4''}$	ω_5	ω_0
AF-Mn in FM Fe (in eV)	0.42	0.65	0.61	0.69	0.57	0.65	0.56	0.75	0.69
Disordered (average) (in eV)	0.30	0.43	0.37	0.47	0.33	0.45	0.47	0.53	0.43

TABLE 4.7: Barrier energies of vacancy migration following the nomenclature of the LeClaire model. The corresponding jumps are schematically shown in Fig. 4.14

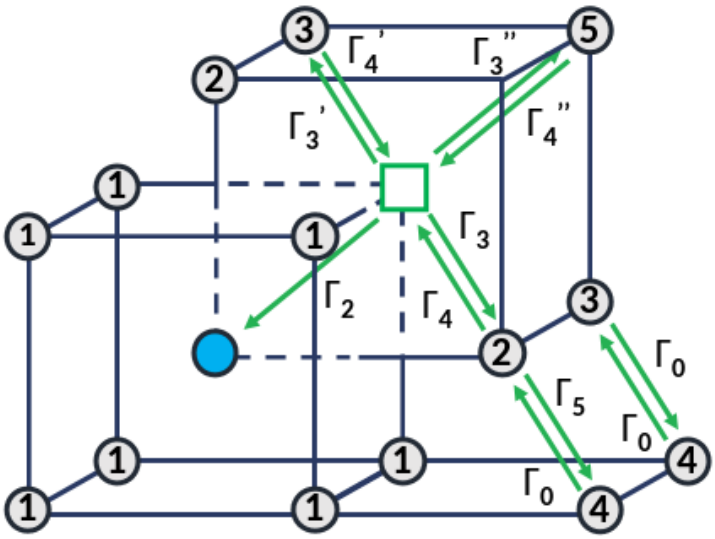

FIGURE 4.14: Schematic representation of the ten jump frequencies necessary to calculate the solute diffusion following the model of LeClaire [92].

Table 4.6 shows a summary of these results, by providing the Mn-vacancy binding energy at 1nn and 2nn distances. It can be noticed that the Mn-Vacancy interaction is attractive at both 1nn and 2nn distances when the Mn magnetic moment is antiparallel to the moments of Fe atoms. Our results are in good agreement with a previous theoretical study [51] which reports similar values in FM state (0.16 and 0.11 eV attractions respectively for 1nn and 2nn Mn-vacancy binding energies) and which also shows that the Mn-vacancy binding energy is negligible in DLM state. To the contrary, FM-Mn shows a repulsive interaction with the vacancy. In other words, the presence of the vacancy increases the energy difference between the two states of Mn from 0.05 eV to 0.27 eV, as shown in chapter 2. We consider all the Mn-vacancy interactions negligible beyond the 2nn distance.

Table 4.7 shows the key barriers based on the LeClaire model. All the values in ferromagnetic Fe are in excellent agreement with the ab-initio results of Messina *et al.* [108].

4.5.2 Model parameterization

In order to model the diffusion of Mn in bcc Fe, the parameters of pure Fe (including a vacancy) are conserved, and so are the Mn on-site parameters and the Fe-Mn exchange coupling parameters when the vacancy is farther than the second-nearest neighbor shell of the Mn atom.

Similarly to the case of pure Fe, the vacancy formation energy in the two nearest-neighbor shells of the Mn solute is parameterized by introducing distinct on-site magnetic terms for the Mn atom, when it is nearest- or next-nearest neighbor of a vacancy.

Also, as shown in DFT calculations, the presence of the vacancy increases the energy difference between AF-Mn and FM-Mn states. That is why we also introduce distinct values of the Fe-Mn exchange coupling parameters when the vacancy is at 1nn and 2nn distance of the Mn solute. Please note that for the sake of simplicity, as we are working in this section with a single Mn atom, the concentration dependence of Fe-Mn magnetic interactions is simplified to the particular case of an isolated Mn atom.

Finally, we introduce a saddle-point model with the same formalism as the one of pure Fe described in section 4.3. It consists in five distinct parameters: the exchange coupling parameters between a Mn saddle-point atom and a Fe lattice site atom up to the second nearest-neighbor shell of the saddle-point, a set of on-site magnetic parameters $A_{Mn}*$ and $B_{Mn}*$ and finally a chemical on-site term, as in the case of Fe.

The parameters of the model are given in Appendix.

4.5.3 Results and discussion

The first step of this study is to determine the vacancy formation energy in the nearest-neighbor shell of the Mn solute. Consistently with the case of pure Fe, we

do not determine directly the formation energy of the vacancy. Instead, we proceed indirectly by evaluating the equilibrium vacancy concentration ratio between pure FM Fe (at a given temperature) and the nearest-neighbor shell of a Mn solute, as explained in section 1.2.4 of the method chapter.

We note that in order to obtain results that can be compared with the self-diffusion of bcc Fe, we use in this section the quantum statistics, with the same method as in pure Fe. Since the system is extremely dilute, we do not adapt the approach to the presence of Mn, eventhough there is a Mn atom in the system.

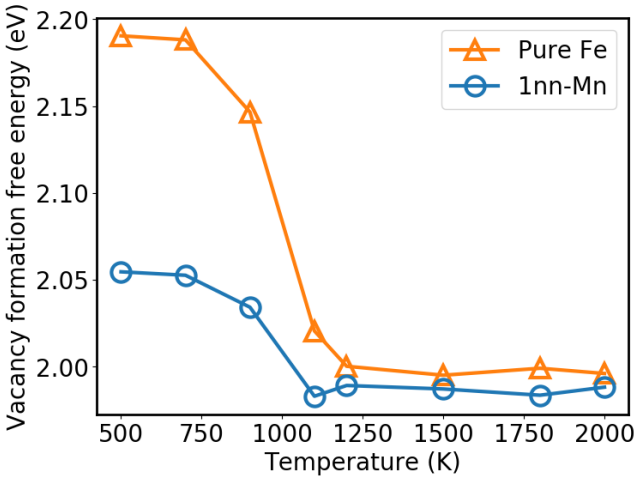

FIGURE 4.15: Temperature dependence of the vacancy formation free energy, in pure Fe (orange) and in the nearest-neighbor shell of a Mn solute.

Figure 4.15 shows the vacancy formation energy in both bcc Fe and and at $1nn$ distance of a Mn solute in Fe, as functions of temperature. As can be noticed, at low temperature the vacancy formation energy at $1nn$ distance from the vacancy is approximately 0.15 eV lower than the formation energy in pure Fe, which is consistent with the binding energy obtained via ab-initio calculations. As the temperature increases, this energy difference is reduced to approximately 0 in the paramagnetic regime, consistently with the DFT results in magnetically disordered state.

As a starting point, the diffusion of Mn in bcc Fe can be evaluated as explained in the method chapter, using the LeClaire model [92]:

$$D^A_{B*} = a^2 C_v^{1nn-Mn} f_2 \Gamma_2 \tag{4.11}$$

where Γ_2 is the jump frequency of the solute-vacancy exchange, identified in Fig. 4.14. It is obtained from the migration energy with the following expression:

$$\Gamma_2 = \nu_2 \exp\left(\frac{-\Delta E_2^{mig}}{k_B T}\right) \tag{4.12}$$

with ν_2 the attempt frequency and E_2^{mig} the migration energy of the Mn-vacancy exchange, as identified in Fig. 4.14.

In equation 4.11, C_v^{1nn-Mn} is the equilibrium vacancy concentration in the nearest-neighbor shell of a Mn solute in Fe and f_2 is the solute diffusion correlation factor, expressed as:

$$t_1 = -\frac{\Gamma_2}{\Gamma_2 + 3\Gamma_3 + 3\Gamma_3' + \Gamma_3'' - \frac{\Gamma_3\Gamma_4}{\Gamma_4+F\Gamma_5} - \frac{2\Gamma_3'\Gamma_4'}{\Gamma_4'+3F\Gamma_0} - \frac{\Gamma_3''\Gamma_4''}{\Gamma_4''+7F\Gamma_0}} \tag{4.13}$$

where Γ_i are the distinct jump frequencies identified in Fig. 1.3 and F is a structure-dependent parameter, its value is 0.512 in the bcc structure [92].

In order to obtain the temperature dependence of Γ_2, we perform migration simulations with a vacancy and a Mn solute at various temperatures in order to estimate the average E_2 barrier. The migration is simulated by using the residence time algorithm, 10^9 atomic-MC steps are performed. Between these atomic jumps, 100 spin MC steps are performed among the whole system, and 500 more are performed among the five nearest-neighbor shells of the vacancy. The average E_2 barrier obtained is shown in Fig. 4.16 along with the migration energy in pure Fe, for comparison.

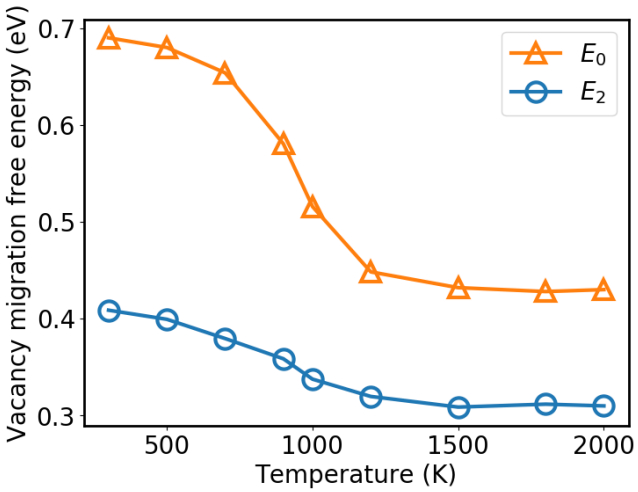

FIGURE 4.16: Temperature dependance of the Mn-vacancy exchange barrier (in blue) compared to the vacancy migration energy in pure Fe (in orange).

At low temperature, the average E_2 barrier is found in agreement with DFT calculations at 0.42 eV, lower than the migration barrier in Fe by 0.28 eV. At the high temperature limit, the average E_2 barrier converges to 0.30 eV, only 0.13 eV below the migration energy in paramagnetic Fe. In the same simulations, the average value of all other key energy barriers can also be determined.

Fig. 4.17 shows the temperature evolution of the various barrier energies of the Leclaire model. The values of E_2 and E_0 are determined over the whole range of temperatures, while the values of the other barriers are determined at low and high temperature limits and interpolated using the temperature dependence of E_0. A

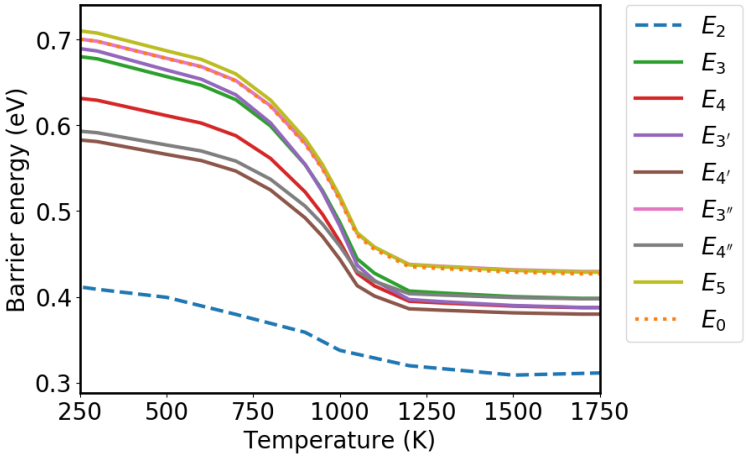

FIGURE 4.17: Temperature evolution of the various barrier energies of the LeClaire model.

complementary value of these barriers is calculated at 1000K in order to confirm that the interpolation is accurate enough.

As all the components of expression 4.11 are known, the LeClaire diffusion coefficient of Mn in bcc Fe can be determined, as a function of temperature.

In order to first validate the approach, we have performed tracer diffusion Monte Carlo simulations imposing a 1K spin temperature (while the atomic temperature is allowed to evolve), in order to constrain the magnetic structure to the magnetic ground-state. The diffusion coefficient resulting from these simulations is in excellent agreement with the Leclaire model, based on the FM system properties.

The vacancy formation entropy in the nearest-neighbor shell of a Mn atom and the attempt frequency of the Mn-vacancy atomic exchange are determined in the FM state via DFT frozen phonons approach. In order to be consistent with the rest of our work, these calculations are performed at constant volume. We found $S^f_{1nn} = 5.5k_B$ (4.8 k_B in pure Fe) and ν_2 = 2.8 THz (ν_0 = 12.6 THz).

Knowing the tracer diffusion coefficient and the LeClaire diffusion coefficient, it is possible determine the actual f_2 correlation factor of the tracer simulations. Fig. 4.18 shows the agreement between the correlation factor of the tracer simulations in constrained FM state and the LeClaire model. We note that although it cannot be seen in the figure because of the scale, we checked that the value of the f_2 converges to an asymptotical value around 0.7 at very high temperature (approx. 0.6 at 6000K).

The same tracer simulations are also performed without the constraint on the spin-temperature. The results are this time compared to the LeClaire model based on spin-temperature dependent properties (for instance, the frequencies used to calculate the f_2 factor depend on the magnetic state of the system).

Fig. 4.18 shows the comparison between the f_2 correlation factor obtained via tracer diffusion and the Leclaire model. It can be noticed that despite the statistical noise of the tracer simulations, both approaches are in overall good agreement.

We also note that the f_2 factor or the FM-constrained calculations is smaller than

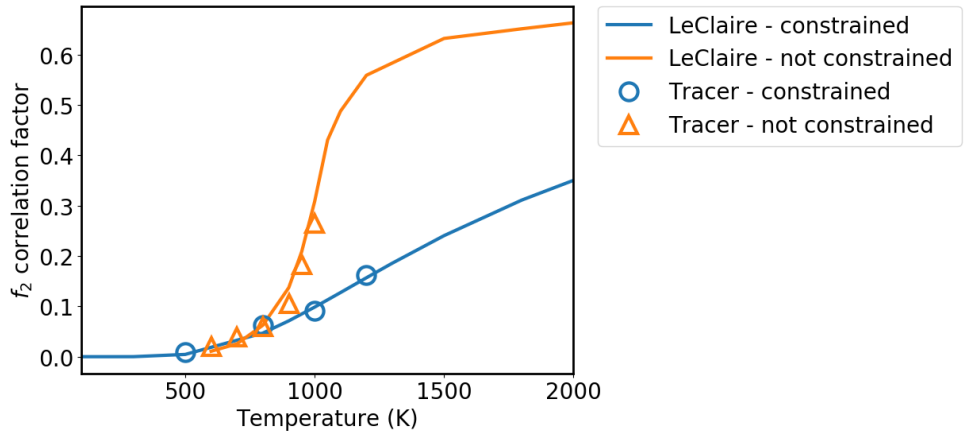

FIGURE 4.18: Temperature dependence of the f_2 correlation factor obtained via LeClaire model and tracer diffusion simulations. The calculations with a constrained low spin temperature are in blue, while the calculations were the atomic and the spin temperatures are equal are in orange.

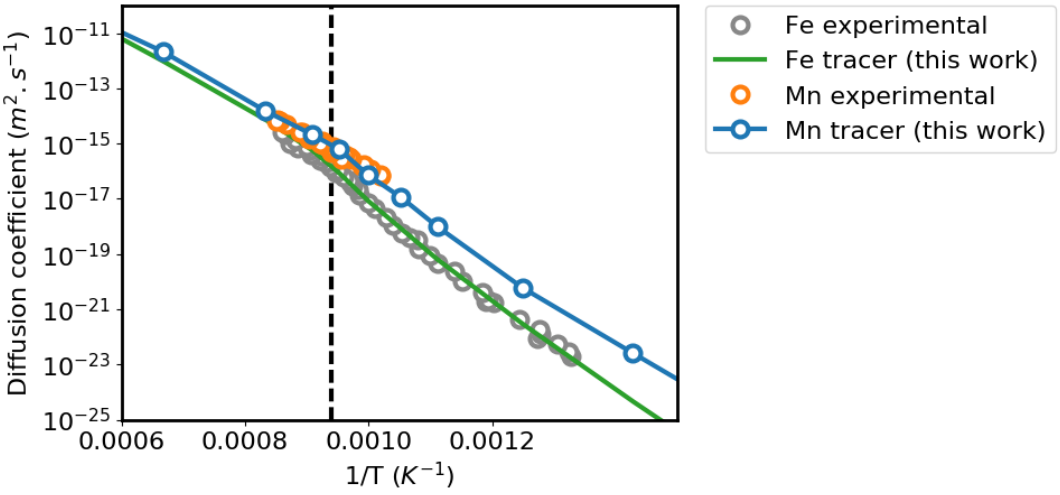

FIGURE 4.19: Diffusion coefficient of Fe and Mn in bcc Fe as functions of temperature, compared with experimental data of Mn diffusion [75, 77, 99] and Fe self-diffusion [66].

the f_2 factor including magnetic relaxations. This result is consistent with a larger dispersion of the various barriers in FM state compared to PM state, as shown in Fig.4.17.

We compare in Fig. 4.19 the temperature dependence of the Mn diffusion coefficient with the self-diffusion coefficient of Fe. It can be noticed that in the case of Mn diffusion, the deviation from Arrhenius law near T_C is much smaller than in the case of Fe. The Mn diffusion curve is much more linear (in logarithmic scale) than the self-diffusion curve which exhibits an acceleration near the magnetic transition temperature, but also a significant change of slope between FM and PM regimes.

This is interesting since the only theoretical study (to the best of our knowledge) which has attempted to predict the temperature evolution of the Mn diffusion coefficient in bcc Fe [108] could not predict correctly the absence of "kink" near T_C. We note that to account for the effects of the transition between FM and PM states, this study adopts a model which provides the activation energy at all temperatures as a function of low and high temperature asymptotical activation energies of Fe diffusion and the magnetic excess enthalpy. Such approach may not be able to properly describe the singular case of Mn.

Also, a study of Ding *et al.* [31] reports a 0.5 eV difference between the paramagnetic and the ferromagnetic activation energy of Mn diffusion which is very different from our results (we note that this study shows a very close value of ΔQ_{FM-PM} for the self-diffusion as our work).

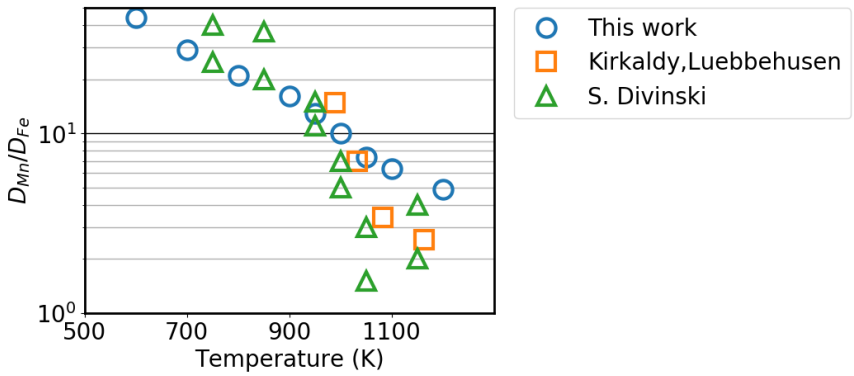

FIGURE 4.20: Ratio between the Mn diffusion coefficient and the Fe self-diffusion coefficient.

Fig. 4.20 shows the ratio between the Mn diffusion coefficient and the Fe self-diffusion coefficient, both obtained via tracer simulations. For comparison, S. Divinski kindly provided such (unpublished) data obtained via tracer experiments. The lowest temperature results available from the experimental side is 750K, at which the ratio is between 10 and 30. The ratio decreases with temperature up to T_C where its value is between 1.5 and 3. Beyond T_C, this ratio slightly increases up to 1150K (which is the highest available data) its value is between 2 and 4. For comparison, as shown in Fig. 4.20, between 700 and 800 the calculated ratio goes from 29 to 20, in good agreement with experimental data. It decreases and reaches between 5 and

7 at T_C, which is in reasonable agreement with the results of Divinski. In the paramagnetic state, the ratio calculated in our work seems to converge to 2. The overall agreement is good, accounting for error-bars in both simulations and experiments.

We determined in this section that the formation and migration energy of a vacancy at $1nn$ distance of a Mn atom are closer to the values in pure Fe in the paramagnetic regime, compared to the ferromagnetic regime (see Fig. 4.15 and Fig. 4.16. This feature suggest that in the dilute case, the magnetic effects are dominant over the chemical effects. As the shape of the diffusion coefficient curve is mainly dictated by the temperature dependance of the activation energy, it is interesting to roughly estimate among other solutes if the deviation from Arrhenius law is related to the values of solute-vacancy binding energy and solute migration energy in ferromagnetic state.

In a recent study [108], a clear trend is identified between the solute-vacancy binding energy and the $3d-$band filling of the solute. The only exception is Mn, which has a higher binding energy and a lower migration energy than what is expected from the general parabollic trend. This deviation may provide a possible explanation for the anomaly of Mn diffusion.

Referring to the systematic study of Messina *et al.* [108], we identified that the solute-vacancy binding energy and the solute migration energy of Ti is quite close to those of a Mn solute (obtained via DFT calculations, in FM bcc Fe). In the case of Co, both migration and binding energies are very far from the values of Mn. Cu also shows significant differences with Mn, in a lesser extent than Co (see Table 4.8).

Solute	$E^{bind}_{sol-vac}$	E^{mig}_{sol}
Mn	0.18	0.42
Ti	0.22	0.38
Cu	0.25	0.50
Fe	0.00	0.70
Co	-0.03	0.75

TABLE 4.8: Solute-vacancy binding energy and migration energy of various solutes in bcc Fe. DFT data obtained from Messina *et al.* [108]

The ferromagnetic activation energy of Mn and Ti diffusion are rather close to the paramagnetic activation energy of self-diffusion. If we assume that the dispersion between the Q_{PM} of solute and self-diffusion is much reduced compared to the FM state (as we observe in the case of Mn), this should also lead to a small $Q_{PM} - Q_{FM}$ difference in the case of Ti. We then expect Ti to also show a rather small "kink" in the diffusion coefficient of Ti near T_C.

In order to verify this hypothesis, we compare in Fig. 4.21 the experimental diffusion coefficients of various solutes in bcc Fe. Please note that to focus on the shape of the curves and their slope, all the curves are shifted such as their diffusion coefficient are equal in the paramagnetic regime (at 1150K).

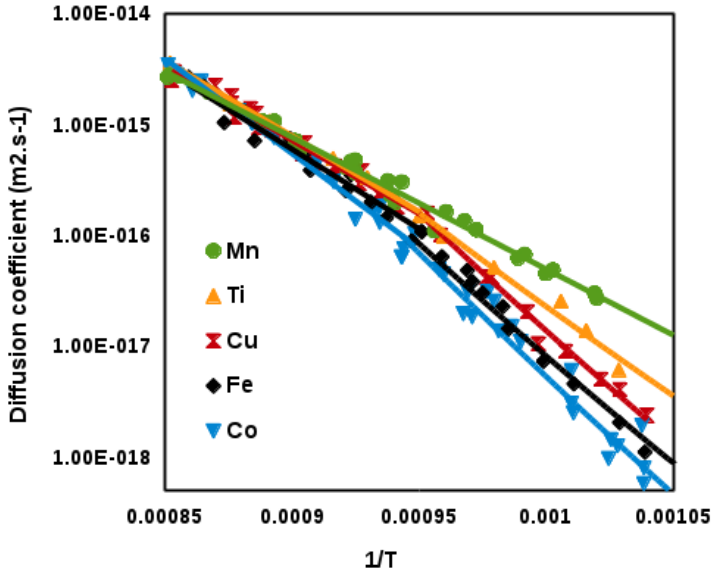

FIGURE 4.21: Experimental diffusion coefficients of various solutes in bcc Fe. Data: Ti [77], Cu [156, 133, 91, 139], Mn [75, 77, 99], Fe [53, 170, 20, 69], Co [18, 106, 67].

We observe that the behavior of Ti solutes is indeed closer to the diffusion curve of Mn (with a tiny "kink"), compared to the other solutes. To the opposite, the diffusion coefficient of Co shows a very strong "kink". Finally, the diffusion coefficient of a Cu solute is in between the behaviors of Fe and Mn.

Please note that this is a very rough comparison which aims at verifying the plausibility of this hypothesis. A deeper study of these solutes (similar to what is done with Mn in this work) is required for a definitive conclusion.

4.6 Conclusion

In Fe-based alloys, self- and most substitutional solute diffusions are generally ruled by vacancy-mechanism (successive vacancy-atom nearest-neighbor exchanges), it is thus necessary to parameterize the formation and the migration properties in order to figure out the role of magnetism on self-diffusion.

In order to validate the approach before studying the solute diffusion, the first step was to parameterize the formation and migration of a vacancy in pure bcc Fe. It is achieved by modeling the presence of a vacancy as an absence of atom and the variation of the surrounding magnetic moments. The migration energy of the vacancy is modeled using a saddle-point Hamiltonian, with a similar formalism (with the coefficients fitted on DFT barrier calculations with magnetic disorder).

As shown through the chapter, there is an overall good agreement between our

approach and existing experimental results. Not only the ferromagnetic and paramagnetic activation energies are in good agreement with the literature, but our approach also allows to determine independently the formation and the migration energy, which repartition is not trivial and plays a crucial role in out-of-equilibrium phenomena. Also, our Monte Carlo simulations directly predict the self-diffusion coefficient as a function of temperature, in excellent agreement with experimental studies. Especially, the deviation from Arrhenius law near the Curie temperature is directly predicted, without any empirical correction. Finally, the change of slope between the ferromagnetic and the paramagnetic regimes is also correctly predicted.

We also compared our work to other theoretical approaches that allow to predict the self-diffusion of Fe. One the one hand, various studies use the Ruch model in order to interpolate the activation energy at intermediate temperatures while providing either both low and high temperature asymptotes, or the ferromagnetic activation energy along with the α parameter of the Ruch model (extracted from the experimental literature). Although we have shown there is a very good agreement between our approach and the Ruch model, it implies to either determine the paramagnetic activation (for instance using DFT with the DLM approach) which is not straightforward, or to obtain the correct value of α which is easy in the case of bcc Fe but much more challenging in alloys. Also, our approach naturally takes into account the interplay between magnetic and chemical order, which is essential for the study of alloys. On the other hand, recent spin-lattice dynamics studies are showing interesting results on the prediction of vacancy properties and self-diffusion in bcc Fe. However, these calculations are based on EAM-type empirical interatomic potentials which are difficult to parameterize, especially for alloys. Also, the computational cost of spin-lattice dynamics simulations limits the simulation space and time scales. However, a major advantage of this method is that it takes directly into account the coupling between phonons and magnons, which makes it more reliable, although it still depends on the potential which is used.

As shown in this chapter, the largest uncertainty of our approach comes from the determination of the diffusion pre-factor D_0 which cannot be accurately predicted. Although it does not impact the temperature dependence of the diffusion coefficient, it induces a vertical uncertainty over the whole curve.

Finally, the same methodology was applied to the case of Mn solute diffusion in bcc Fe at extreme dilution limit (one single solute atom). We have found that the activation energy of Mn diffusion at low temperature is close to the paramagnetic activation energy of self-diffusion, which leads to a particularly small difference between the Mn diffusion Q_{FM} and Q_{PM}. Using both tracer diffusion simulations and the LeClaire model, we have shown that the acceleration of diffusion near T_C is highly reduced in the case of Mn compared to the self-diffusion of Fe. These early results are in excellent agreement with experimental observations and may contribute to the understanding of the diffusion anomaly of Mn in bcc Fe, which is a step forward compared to the available theoretical literature.

Conclusions and perspectives

The purpose of this three-years work was to push forward the understanding of the interplay between magnetism, thermodynamics and diffusion in bcc Fe-Mn alloys. From the very beginning of the PhD, exciting challenges arised, mainly from the singular magnetic properties of Mn solutes in bcc Fe.

In order to face these challenges, several tools and methodologies were involved. Firstly, ab-initio calculations allowed us to probe the energetic and magnetic properties of bcc Fe-Mn alloys at the ground-state as functions of the alloy concentration and local chemical environment. In the first-principles study presented in chapter 2, we confirmed that a single atom Mn solute in bcc Fe exhibits two colinear energy minima, either parallel or anti-parallel to the Fe moments, the latter being the ground-state. Interestingly, the relative energy of these two minima is highly sensitive to minor changes of the Mn local environment, due to the presence of a high Mn majority-spin electronic density around the Fermi level. Especially, we found a significant correlation between the local charge density and the magnetic coupling preference of a Mn atom with the Fe atoms of the matrix. More precisely, we identified that an increase of the local charge density, caused for instance by the presence of a covalent interstitial impurity (e.g. carbon or nitrogen) tends to favor the FM Fe-Mn coupling. In the opposite, the presence of a vacancy nearby tends to favor the AF Fe-Mn coupling. These results are also consistent with another recent theoretical study [74] showing that a compressive hydrostatic pressure tends to favor the FM Fe-Mn coupling and vice-versa.

Small n-Mn clusters are found to be energetically favorable, consistently with the unmixing tendency found for the bcc Fe-Mn alloys. Various collinear and non-collinear magnetic minima are found for the Mn dimer, which are rather close in energy. It is relevant to point out that our results suggest a dominance of Mn-Mn magnetic interactions over the Fe-Mn interactions, both exhibiting an antiferromagnetic tendency, especially for the $1nn$ and $2nn$ distances (contrary to Fe-Cr alloys). A vacancy is found to further stabilize the Mn clusters and reciprocally, the formation energy of a vacancy becomes smaller in a Mn-rich than in a Fe-rich local environment. We note that this behavior may promote a rather fast diffusion of Mn nanoclusters, similarly to the case of bcc Fe-Cu alloys.

Locally random Fe-Mn solid solutions were systematically investigated for a large range of Mn concentrations. Consistently with experimental findings, the average magnetic moment of the alloys decreases linearly with increasing Mn content. In addition, the average Mn moment tends to be antiparallel (resp. parallel) to lattice Fe moments for Mn concentrations smaller (resp. larger) than approximately 7 at.%

Mn. It is not clear whether the same trend is observed experimentally or not as the literature contains contradictory results at low Mn concentrations (less than 2 at.% Mn). However, at concentrations higher than 2 at.%, experimental works all agree on the fact that the average Mn moment tends to be parallel to Fe. We showed that considering clusters instead of random solutions lowers this transition to approximately 2 at.% Mn, which may be a plausible explanation of these discrepancies. Also, we have shown that the magnetic state of Mn solutes in bcc Fe is highly dependent of the exchange-correlation functional and the lattice constant, which lowers the trust we put in these DFT calculations.

As magnetism plays a significant role in the thermodynamic properties of Fe-based alloys, we aimed at studying these interplays in bcc Fe-Mn alloys.

In addition to providing a better understanding of the ground-state magnetic and energetic properties in bcc Fe-Mn alloys, the ab-initio results obtained in this work were used to parameterize an effective interaction model, explicitly taking into account magnetic and chemical variables. As described in chapter 3, the parameterization of this model was not trivial at all because of the complexities induced by Mn magnetism. The parameters of the model were fitted progressively, on key properties of bcc Fe-Mn alloys and following general trends identified via DFT calculations (for instance the dominance of Mn-Mn interactions over the Fe-Mn ones), which allow to model quite complex phenomena with a rather limited dataset. Also, non-collinear magnetic calculations were included in the fitting dataset in order to avoid artificially stable configurations at low temperature.

The model was coupled with rigid-lattice Monte Carlo simulations in order to simulate various finite temperature properties of bcc Fe-Mn alloys. Although the general approach is quite common in the literature, we innovated by systematically coupling two Monte Carlo simulations respectively on magnetic and chemical degrees of freedom, which allow to model the evolution of the atomic configuration (atom pair-exchanges), while relaxing the magnetic state of the system on-the-fly.

As shown in the application examples of chapter 3, this approach allows to predict for instance the temperature evolution of the mixing energy, at any concentration. Also, we roughly estimated the temperature of transition between solid solution and phase decomposition over the whole range of concentration, Finally, this approach allowed to predict the evolution of the Curie temperature as a function of Mn concentration in excellent agreement with experimental results.

Also, this approach allows to easily include external magnetic fields. Some examples of applications are shown in chapter 3, exhibiting for instance the increase of T_C with the external field, in pure Fe and Fe-Mn.

Such simulation of the evolution of bcc Fe-Mn alloys allows us to study the thermodynamic equilibrium states at any temperature and concentration, but it does not provide any information on the kinetic properties of the systems. As diffusion in Fe-alloys is frequently ruled by vacancy-mechanism (successive vacancy-atom

nearest-neighbor exchanges), it was necessary to parameterize the properties of a vacancy.

The study of the effects of magnetism on diffusion is particularly interesting as it has been shown experimentally that the diffusion of Mn in bcc Fe, contrary to every other transition metal, does not show any acceleration near the Curie temperature, compared to the Arrhenius law. The work presented on chapters 4 aims at better understanding this anomaly.

In order to validate the approach, we first parameterized models to address the presence of a vacancy at a lattice site and at a saddle-point, respectively. The temperature evolution of self-diffusion was predicted via tracer diffusion Monte Carlo simulations, in very good agreement with experimental results. We found that the use of quantum statistics is necessary to accurately reproduce the deviation from Arrhenius law around the Curie temperature. We point out the satisfactory accuracy of the Ruch model to predict the temperature dependence of the self-diffusion coefficients, if knowing the activation energy in the fully paramagnetic regime (estimated for instance using DFT with the DLM approach) and the temperature dependence of the magnetization. We also compared our results with the Spin-Lattice dynamics approach, which gives satisfactory results in pure Fe, but highly depends on the empirical interatomic potential which is used.

Finally, the same methodology was applied to the case of Mn solute diffusion in bcc Fe at extreme dilution limit (one single solute atom). We have shown using tracer diffusion simulations that the diffusion acceleration near T_C is highly reduced in the case of Mn compared to the self-diffusion of Fe. This behavior is related to a particularly small difference between the ferromagnetic and paramagnetic activation energies. These early results are in excellent agreement with experimental observations and may help to understand the diffusion anomaly of Mn in bcc Fe, which is a step forward compared to the available theoretical literature.

As usual in scientific research, the work on this topic is far from being over. We have studied in detail some key features of magnetic and energetic properties of bcc Fe-Mn alloys, and developed simulation models and tools for the thermodynamics and diffusion in bcc Fe and Fe-Mn as functions of temperature and across the Curie point. These approaches should be easily transferred for the study of other metal magnetic alloys, and extended to other kinetic properties such as ordering or phase decomposition.

The perspectives of this work may be sorted in two categories: improvements and extensions.

The former category concerns all the possible ways of improvements of our approach, as many approximations or choices have been done.

Concerning the first-principles calculations, we opted for the GGA exchange-correlation functional and the PAW approach as it is known to be highly reliable for Fe-based alloys. As shown by Olsson *et al.* [124] or even by our own benchmarks, the magnetic coupling preference of a Mn atom with the Fe moments of the matrix

highly depends on the ab-initio methodology. Although our choice is justified by the tests done via all-electrons calculations using Wien2k, the inconsistencies with experimental results are troublesome. On this issue, supplemental efforts may be done on both sides, by performing additional *ab-initio* studies with diverse methodological variations (exchange-correlation functional, pseudo-potential...). Further experimental systematic studies may also be done, including magnetic measurements, microstructural observations and chemical analysis, in order to achieve a closer modeling (by comparison with these experiments).

Still concerning the DFT based study, we have shown in chapter 2 that the collinear magnetic configurations of a Mn-dimer are almost degenerate with several non-collinear magnetic configurations. Despite this result, we ignored the possible non-collinear configurations in the case of Mn-clusters, because of the computational cost of such a study. It would however be interesting to explore the possible non-collinear configurations of these Mn-clusters, some could have lower energy than the collinear ground-states we identified.

Of course, the parameterization of the model may always be improved, by completing the data-set (for instance with aforementioned non-collinear configurations of Mn-clusters) and by adding local environment dependent or many-body interactions, if necessary.

Also, our Monte Carlo simulations are performed on rigid lattice, which is a very practical approximation. Although it represents a substantial amount of work, it would be interesting to parameterize an off-lattice model, with interatomic distance dependent interactions. As it is far from being straightforward, a compromise could be to refine the current approach by adding an elastic correction term to the rigid lattice model.

Finally, considering quantum statistics in Monte Carlo simulations has a significant impact on some properties (e.g. self-diffusion in bcc Fe). So far, we did not use the Bose-Einstein distribution in alloys simulations as it represents a significant amount of additional work, but evaluating the quantum effects in Fe-Mn alloys would be highly interesting.

In addition to these improvements of our methodology, other perspectives also arise from this thesis. Indeed, the approaches shown in this work may (and should, I think) be applied to complementary features that we could not focus on during these three years.

Concerning the DFT based study, the effects on Mn magnetism of a plethora of defects may be investigated, while we limited ourselves to vacancies and C, N and O interstitial impurities. To begin with, a more systematic study with various concentrations of vacancies or interstitial impurities may be interesting, to determine whether the trend identified in chapter 2 is consistent with higher defect concentrations or not. This ab-initio study may also include extended defects, such as dislocations or interfaces. Also, it would be interesting to complete the study with the fcc phase of Fe-Mn alloys, to perform a systematic comparison of properties between

bcc and fcc phases, and eventually to study the interface between a bcc Fe-rich phase and a fcc Mn-rich phase.

Concerning the model approach, we have studied so far the diffusion of a single Mn atom in bcc Fe, in other words Mn diffusion in bcc Fe-Mn at infinite dilution. It would be interesting to extend this study to more concentrated alloys and to determine the effect of Mn concentration on diffusion properties. Also, a systematic study of solute diffusion in Fe, at least in the very dilute limit, would help to better understand the atypical case of Mn, and to further verify and justify our predictions. The extention of the present model to various solutes in the dilute limit should be rather straightforward.

The bcc-fcc Fe-Mn properties comparison could be extended to finite temperatures by parameterizing a similar effective interaction model for fcc Fe-Mn alloys. Also, despite being a tedious work, parameterizing the effects of extended defects with a similar approach as ours could lead to the study of grain-boundary diffusion, which is highly interesting, and which is currently being experimentally investigated.

Finally, other perspectives could also be the study of diffusion under external magnetic field and the kinetics of ordering or phase decomposition in alloys.

In anyway, the remaining work to perfectly understand the interplay between magnetism, thermodynamics and diffusion in Fe-Mn is titanic, and I am thankful for the opportunity I got to modestly contribute to the effort.

Appendix: Interaction model parameters

In this appendix are provided all the numerical values of the interation model parameters used in the chapters 3 and 4 of this thesis.

The Hamiltonian for the study of Fe-Mn alloys, used in chapter 3, is given in equation 14.

$$H = \sum_{i}^{N} A_i M_i^2 + B_i M_i^4 + \sum_{i}^{N}\sum_{n}^{P}\sum_{j}^{Z} J_{ij}^{(n)} \mathbf{M}_i \cdot \mathbf{M}_j + \sum_{i}^{N}\sum_{n}^{P}\sum_{j}^{Z} V_{ij}^{(n)} \tag{14}$$

where P is the maximum range of interactions in terms of neighbor shells, Z is the number of neighbors of each interaction range, $\mathbf{M}_i$ is the magnetic moment of the ith atom, M_i is its magnitude and $V_{ij}^{(n)}$ represents the chemical pair-interaction between species of atoms i and j, at range n. A_i and B_i are the magnetic on-site terms of the i-th atom.

The parameters of this model are given in the following tables.

Interactions	J^1_{Fe-Fe}	J^2_{Fe-Fe}	J^3_{Fe-Fe}	J^4_{Fe-Fe}	J^5_{Fe-Fe}
Value (meV)	-3.39	-2.26	-0.83	0.42	0.44

TABLE 9: Magnetic interaction parameters between two Fe atoms in a stable position (not at saddle point)

Interactions	A^0_{Fe}	B^0_{Fe}
Value (meV)	-259.0	27.6

TABLE 10: Magnetic on-site terms of Fe atoms in a stable position.

Interactions	V^1_{Fe-Fe}	V^2_{Fe-Fe}
Value (meV)	-10.85	8.18

TABLE 11: Chemical interaction parameters of the model between two Fe atoms in a stable position.

Interaction	J^1_{Mn-Mn}	J^2_{Mn-Mn}	J^3_{Mn-Mn}	J^4_{Mn-Mn}	J^5_{Mn-Mn}
Value (meV)	1.51	1.30	0.26	-0.98	0.53

TABLE 12: Magnetic interaction parameters between two Mn atoms in a stable position.

Interactions	A_{Mn}	B_{Mn}
Value (meV)	-37.70	6.93

TABLE 13: Magnetic on-site terms of Mn atoms in a stable position.

Interactions	V^1_{Mn-Mn}	V^2_{Mn-Mn}	V^3_{Mn-Mn}	V^4_{Mn-Mn}	V^5_{Mn-Mn}
Value (meV)	4.63	-1.93	-1.06	-0.19	0.25

TABLE 14: Chemical interaction parameters between two Mn atoms in a stable position.

The expression of Fe-Mn interaction parameters is:

$$J^n_{Fe-Mn} = \left[J^n_0 \cdot \frac{\theta - 90}{90}\right] + \left[a \cdot [Mn]^4_{loc} + b \cdot [Mn]^3_{loc} + c \cdot [Mn]^2_{loc} + d \cdot [Mn]_{loc} + e\right] \tag{15}$$

where the J^n_0 is the original J^n_{Fe-Mn} parameter, before considering the angle and concentration dependencies. This parameter ensures the range dependence of the interaction (Since the angle and concentration dependencies do not depend on the interaction range). θ is the angle between the Mn magnetic moment and the average of the spins of the Fe atoms in the two nearest-neighbor shells of the considered Mn atom. $[Mn]_{loc}$ is the local Mn concentration (in the five nearest-neighbor shells around the concerned atom).

Interaction	J^1_0	J^2_0	J^3_0	J^4_0	J^5_0
Value (meV)	0.057	0.066	0.042	0.089	0.026

TABLE 15: J^n_0 coefficients that contribute to the magnetic interaction parameters between a Fe atom and a Mn atom in a stable position.

Interaction	a	b	c	d	e
Value (meV)	6.50E-8	-8.40E-6	3.83E-4	-7.16E-3	3.04E-2

TABLE 16: Parameters of the polynomial function ensuring the local Mn concentration dependence of Fe-Mn magnetic interaction parameters.

Interactions	V^1_{Fe-Mn}	V^2_{Fe-Mn}
Value (meV)	-6.09	3.75

TABLE 17: Chemical interaction parameters between a Fe atom and a Mn atom, both in a stable position.

For the study of pure Fe with a vacancy on a lattice site, the Hamiltonian given in expression 14 is applied, and all the previous parameters of pure Fe (Tables 9, 11 and 10) are used.

The presence of the vacancy is parameterized using distinct sets of on-site magnetic terms for the atoms at $1nn$ and $2nn$ distances of the vacancy. These distinct parameters are given in the following Table.

Interactions	A^0_{Fe}	B^0_{Fe}	A^1_{Fe}	B^1_{Fe}	A^2_{Fe}	B^2_{Fe}
Value (meV)	-259.0	27.6	-250.2	24.7	-285.7	35.2

TABLE 18: Magnetic on-site terms of Fe atoms in a stable position (not at saddle point). The "0" exponent concerns bulk Fe-atoms, the "1" exponent concerns the Fe-atoms at $1nn$ distance from a vacancy and the "2" exponent concerns the Fe-atoms at $2nn$ distance from a vacancy

For the study of vacancy migration and self-diffusion in pure Fe, we use the saddle-point Hamiltonian given in expression 16.

$$H^* = A^* M_0^2 + B^* M_0^4 + \sum_n^P \sum_j^Z J_{0j}^{*(n)} \mathbf{M}_0 \cdot \mathbf{M}_j + \sum_n^P \sum_j^Z V_{0j}^{*(n)} \tag{16}$$

where P is the maximum range of interactions in terms of neighbor shells, Z is the number of neighbors of each interaction range and $\mathbf{M_0}$ is the magnetic moment of the saddle-point atom, M_0 is the corresponding magnitude and $J_{0j}^{*(n)}$ represent the magnetic pair-interaction between the saddle point atom and its neighbors (at range n). A^* and B^* are the magnetic on-site parameters of the saddle-point atom.

Interactions	J^{*1}_{Fe-Fe}	J^{*2}_{Fe-Fe}	A^*_{Fe}	B^*_{Fe}
Value (meV)	-10.3	4.7	-170.1	15.6

TABLE 19: Saddle point parameters of Fe atoms, including the magnetic exchange coupling parameters at $1nn$ and $2nn$ distance of the saddle-point and the magnetic on-site terms.

Interactions	V^{*1}_{Fe-Fe}	V^{*2}_{Fe-Fe}
Value (meV)	-10.85	8.18

TABLE 20: Chemical interactions at $1nn$ and $2nn$ distance between a Fe atom at saddle-point and a Fe atom at a stable position.

For the study of Mn diffusion in Fe, the Hamiltonians given in expressions 14 and 16 are used. All the previous parameters of pure Fe with vacancies (Tables 9, 11, 21 and 25) are used. Also, the parameters of Mn are used (Tables 13, 23, 16 and 29).

The effects of the vacancy on the Mn solute are parameterized using distinct sets of on-site magnetic terms for the Mn solute at $1nn$ and $2nn$ distances of the vacancy but also distinct sets of magnetic Fe-Mn interactions when the Mn solute is at $1nn$ and $2nn$ distances of the vacancy. These distinct parameters are given in the following Tables.

Interactions	A^0_{Mn}	B^0_{Mn}	A^1_{Mn}	B^1_{Mn}	A^2_{Mn}	B^2_{Mn}
Value (meV)	-37.70	6.93	-116.2	8.54	-37.70	6.93

TABLE 21: Magnetic on-site terms of Fe atoms in a stable position (not at saddle point). The "0" exponent concerns bulk Fe-atoms, the "1" exponent concerns the Fe-atoms at $1nn$ distance from a vacancy and the "2" exponent concerns the Fe-atoms at $2nn$ distance from a vacancy

Interaction	J^1_{0-1nn}	J^2_{0-1nn}	J^3_{0-1nn}	J^4_{0-1nn}	J^5_{0-1nn}
Value (meV)	0.232	0.261	0.187	0.327	0.138

TABLE 22: Magnetic interaction parameters of the model between a Fe atom and a Mn atom in a stable position when the Mn atom is at $1nn$ distance of a vacancy.

Interaction	J^1_{0-2nn}	J^2_{0-2nn}	J^3_{0-2nn}	J^4_{0-2nn}	J^5_{0-2nn}
Value (meV)	0.189	0.212	0.151	0.267	0.110

TABLE 23: Magnetic interaction parameters of the model between a Fe atom and a Mn atom in a stable position when the Mn atom is at $2nn$ distance of a vacancy.

Interactions	J^{*1}_{Mn-Fe}	J^{*2}_{Mn-Fe}	A^*_{Mn}	B^*_{Mn}
Value (meV)	5.06	-3.99	-116.2	8.54

TABLE 24: Saddle point parameters of Mn atoms, including the magnetic exchange coupling parameters at $1nn$ and $2nn$ distances of the saddle-point and the on-site magnetic parameters.

Interactions	J^{*1}_{Fe-Mn}	J^{*2}_{Fe-Mn}
Value (meV)	10.28	-4.66

TABLE 25: Magnetic exchange coupling parameters at $1nn$ and $2nn$ distances between a Fe atom at saddle-point and a Mn atom in a stable position.

Interactions	$V^1_{Fe-Mn}(1nn)$	$V^2_{Fe-Mn}(1nn)$
Value (meV)	30.2	-17.3

TABLE 26: Chemical interaction parameters between a Fe atom and a Mn atom, both in a stable position, when the Mn atom is the nearest neighbor of a vacancy

Interactions	$V^1_{Fe-Mn}(2nn)$	$V^2_{Fe-Mn}(2nn)$
Value (meV)	-30.2	17.3

TABLE 27: Chemical interaction parameters between a Fe atom and a Mn atom, both in a stable position, when the Mn atom is the next nearest neighbor of a vacancy

Interactions	V^{*1}_{Fe-Mn}	V^{*2}_{Fe-Mn}
Value (meV)	-10.85	8.18

TABLE 28: Chemical interaction parameters between a Fe atom at saddle point and a Mn atom in a stable position

Interactions	V^{*1}_{Mn-Fe}	V^{*2}_{Mn-Fe}
Value (meV)	29.7	0.01

TABLE 29: Chemical interaction parameters between a Mn atom at saddle point and a Fe atom in a stable position

In order to check the overall quality of the models parameterization, the six graphs of Fig. 22 show the correlation between the DFT and the model predictions (using the DFT configurations as input).

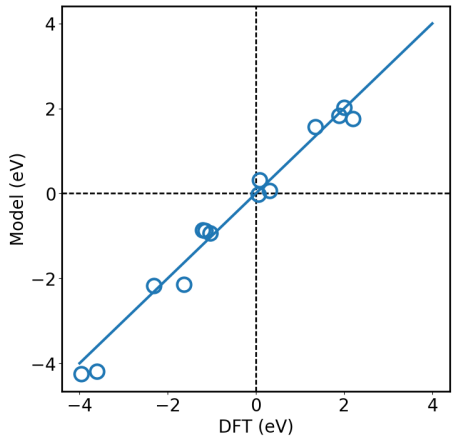

(a) Energy differences between various magnetic configurations of pure Fe.

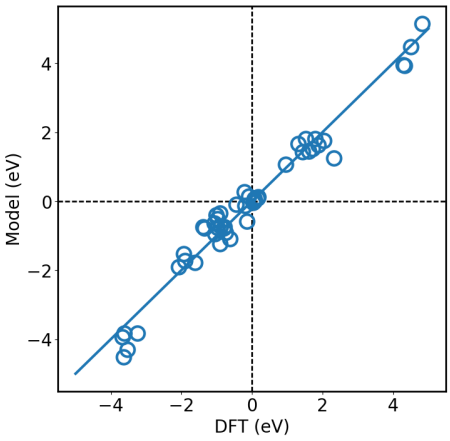

(b) Energy differences between various magnetic configurations of pure Fe with one vacancy

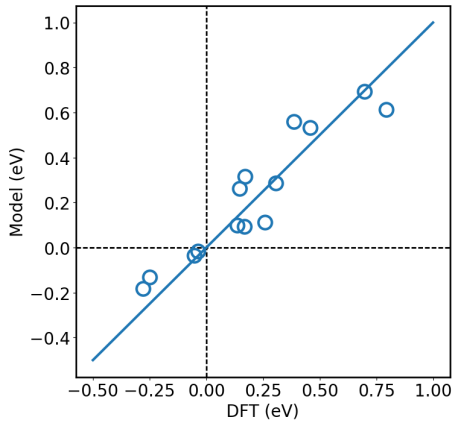

(c) Migration barriers in pure Fe with various magnetic configurations.

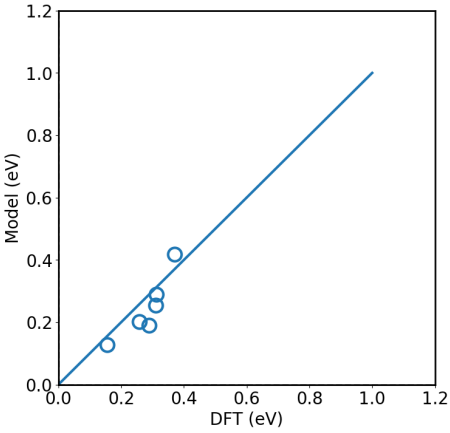

(d) Mn migration barriers in pure Fe with various magnetic configurations.

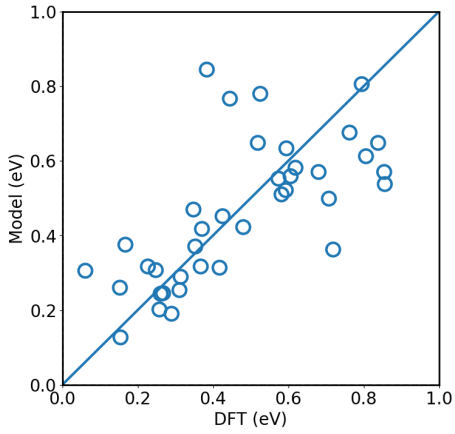

(e) Various migration barriers around a Mn solute in pure Fe, with various magnetic configurations.

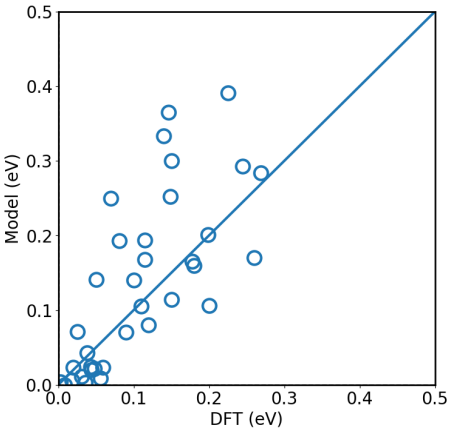

(f) Mn-vacancy binding energy in pure Fe, with various magnetic configurations.

FIGURE 22: Correlation between the DFT and the model predictions (using DFT configurations as input). The straight lines show x=y.

Bibliography

[1] Y. Adda and J. Philibert. *La diffusion dans les solides*. Institut national des sciences et techniques nucléaires, 1966.

[2] B. Alling, T. Marten, and I. A. Abrikosov. In: *Nature Mater.* 9 (2010), p. 283.

[3] B. Alling, T. Marten, and I. A. Abrikosov. In: *Phys. Rev. B* 82 (2010), p. 184430.

[4] P. D. Anderson and R. Hultgren. In: *Trans. A. I. M. E.* 224 (1962), p. 842.

[5] V. I. Anisimov et al. In: *Phys. Rev. B* 37 (1988), p. 5598.

[6] V. P. Antropov, B. N. Harmon, and A. N. Smirnov. In: *J. Magn. Magn. Mater.* 200 (1999), p. 148.

[7] S. Arajs. In: *Phys. Stat. Sol.* 11 (1965), p. 121.

[8] N. W. Ashcroft and D. Mermin. *Solid State Physics*. Saunders College Publishers, 1976.

[9] A. Bakaev et al. In: *J. Nucl. Mater.* 444 (2014), p. 237.

[10] C. Barouh et al. In: *Phys. Rev. B* 90 (2014), p. 054112.

[11] W. Bendick and W. Pepperhoff. In: *Acta Metall.* 30 (1982), p. 679.

[12] L. Bergqvist and A. Bergman. In: 2 (2018), p. 013802.

[13] H. Bhatkar et al. In: *J. Magn. Magn. Mater.* 423 (2017), p. 46.

[14] S. Bigdeli and M. Selleby. In: *Calphad* 64 (2019), p. 185.

[15] K. E. Bloechl. In: *Phys. Rev. B* 50 (1994), p. 17953.

[16] S. Blügel et al. In: *Phys. Rev. B* 35 (1987), p. 3271.

[17] R. J. Borg and Birchenall C. E. In: *Trans. A. I. M. E.* 218 (1960), p. 980.

[18] R. J. Borg and D. Y. F. Lai. In: *Acta Metall.* 11 (1963), p. 861.

[19] M. Born and R. Oppenheimer. In: *Adv. Phys.* 389 (1927), p. 457.

[20] F. S. Buffington, K. Hirano, and M. Cohen. In: *Acta Metall.* 9 (1961), p. 434.

[21] J. B. J Chapman, P-. W. Ma, and S. L. Dudarev. In: *Phys. Rev. B* 99 (2019), p. 184413.

[22] C. T. Chen et al. In: *Phys. Rev. Lett.* 75 (1995), p. 152.

[23] Q. Chen and B. Sundman. In: *J. Phase Equilibria* 22 (2001), p. 631.

[24] Y. Chen et al. In: *Phys. Rev. B* 31 (1985), p. 6775.

[25] H. R. Child and J. W. Cable. In: *Phys. Rev. B* 13 (1976), p. 227.

[26] C. P. Chui and Y. Zhou. In: *AIP Advances* 4 (2014), p. 087123.

[27] M. F. Collins and G. G. Low. In: *Proc. Phys. Soc.* 86 (1965), p. 535.

[28] J. M. Cowley. In: *Phys. Rev.* 77 (1950), p. 669.

[29] L. De Schepper et al. In: *Phys. Rev. B* 27 (1983), p. 5257.

[30] W. A. Dench and O. Kubaschewski. In: *J. Iron Steel Inst.* 201 (1963), p. 140.

[31] H. Ding, V. I. Razumovskiy, and M. Asta. In: *Acta Mater.* 70 (2014), p. 130.

[32] C. Domain and C. Becquart. In: *Phys. Rev. B* 65 (2002), p. 024103.

[33] C. Domain and C. Becquart. In: *Phys. Rev. B* 71 (2005).

[34] M. Doyama. In: *Trans. Jpn. Inst. Met.* 25 (1986), p. 808.

[35] A. Einstein. In: *Adv. Phys.* 17 (1905), p. 549.

[36] A. Einstein. In: *Adv. Phys.* 19 (1906), p. 371.

[37] O. Eriksson et al. In: *Phys. Rev. B* 45 (1992), p. 2868.

[38] S. Frota-Pessoa, R. B. Muniz, and J. Kudrnovsky. In: *Phys. Rev. B* 62 (2000), p. 5293.

[39] C.-C. Fu, F. Willaime, and P. Ordejon. In: *Phys. Rev. Lett.* 92 (2004), p. 175503.

[40] C-.C. Fu et al. In: *Phys. Rev. B* 91 (2015), p. 094430.

[41] B. Fultz. In: *Progress in Mat. Sci.* 55 (2010), p. 247.

[42] I. Galanakis. In: *Phys. Rev. B* 71 (2004), p. 012413.

[43] D. Gambino and B. Alling. In: *Phys. Rev. B* 98 (2018), p. 064105.

[44] J. Geise and C Herzig. In: *Z. Metallkde.* 78 (1987), p. 291.

[45] P. Giannozzi. In: *J. Phase Equilibria* 21 (2009), p. 395502.

[46] P. Giannozzi. In: *J. Phase Equilibria* 29 (2017), p. 465901.

[47] L. Girifalco. In: *J. Phys. Chem. Solids* 23 (1962), p. 1171.

[48] L. Girifalco. "Diffusion". In: (1960).

[49] L. A. Girifalco. In: *Mater. Sci. Engin.* 9 (1972), p. 61.

[50] B. Gomez-Ferrer. "Resistivity Recovery in Fe and Fe-Cr alloys". In: (2016).

[51] O. I. Gorbatov et al. In: *J. Nucl. Mater.* 475 (2016), p. 140.

[52] S. Gosh et al. In: *Eur. Phys. J. B* 23 (2001), p. 455.

[53] D. Graham and D. H. Tomlin. In: *Philos. Mag.* 8 (1963), p. 1581.

[54] O. Grotheer, C. Ederer, and M. Faehnle. In: *Phys. Rev. B* 63 (2001), p. 100401.

[55] J. Hafner and D. Hobbs. In: *Phys. Rev. B* 68 (1 2003), p. 014408.

[56] R. Hafner et al. In: *Phys. Rev. B* 65 (2002), p. 184432.

[57] S. V. Halilov et al. In: *Europhys. Lett.* 39 (1997), p. 91.

[58] P. Hanggi, P. Talkner, and M. Borkovec. In: *Rev. Mod. Phys.* 62 (1990), p. 251.

[59] R. D. Hatcher, R. Zeller, and P. H. Dederichs. In: *Phys. Rev. B* 19 (1979), p. 5083.

[60] H. C. Herper, E. Hoffmann, and P. Entel. In: *Phys. Rev. B* 60 (1999), p. 3839.

[61] G. Hettich, H. Mehrer, and K. Maier. In: *Scr. Metall.* 11 (1977), p. 795.

[62] M. Hillert and M. Waldenstrom. In: *Scand. J. Metall.* 6 (1977), p. 211.

[63] D. Hobbs, J. Hafner, and D. Spisak. In: *Phys. Rev. B* 68 (1 2003), p. 014407.

[64] P Hohenberg and W. Kohn. In: *Phys. Rev.* 136 (1964), B864.

[65] S. Huang et al. In: *Acta Mater.* 58 (2010), p. 1982.

[66] Y. Iijima, K. Kimura, and K. Hirano. In: *Acta Metall.* 36 (1988), p. 2811.

[67] Y. Iijima et al. In: *Mater. Trans. Jpn. Inst. Metals* 34 (1993), p. 20.

[68] V. Jaccarino, L. R. Walker, and G. K. Wertheim. In: *Phys. Rev. Lett.* 14 (1965), p. 89.

[69] D. W. James and G. M. Leak. In: *Philos. Mag.* 14 (1966), p. 701.

[70] D. E. Jiang and E. A. Carter. In: *Phys. Rev. B* 67 (2003), p. 214103.

[71] F. Kajzar and G. Parette. In: *Phys. Rev. B* 22 (1980), p. 5471.

[72] S. G. Kang et al. In: *J. Phys. Soc. Jpn* 36 (1974), p. 975.

[73] F. Keffer. *Handbuch der Physik, 18, pt. 2*. Springer-Verlag, New York.

[74] D. M. King et al. In: *Phys. Rev. B* 98 (2018), p. 024418.

[75] J. S. Kirkaldy, P. N. Smith, and R. C. Sharma. In: *Met. Trans.* 4 (1973), p. 624.

[76] T. P. C. Klaver, R. Drautz, and M. W. Finnis. In: *Phys. Rev. B* 74 (2006), p. 094435.

[77] P. Klugkist and Ch. Herzig. In: *Phys. Stat. Sol.* 148 (1995), p. 413.

[78] F. Koermann et al. In: *Phys. Rev. B* 83 (2011), p. 165114.

[79] W. Kohn and L. J. Sham. In: *Phys. Rev.* 140 (1965), A1133.

[80] G. Kresse and J. Furthmueller. In: *Commun. Math. Phys.* 6 (1996), p. 15.

[81] G. Kresse and J. Furthmueller. In: *Phys. Rev. B* 54 (1996), p. 11169.

[82] G. Kresse and J. Hafner. In: *Phys. Rev. B* 47 (1993), p. 558.

[83] G. Kresse and J. Joubert. In: *Phys. Rev. B* 59 (1999), p. 1758.

[84] J. Kucera et al. In: *Acta Metall.* 22 (1974), p. 135.

[85] N. I. Kulikov and C. Demangeat. In: *Phys. Rev. B* 55 (1997), p. 3533.

[86] D. Landau and K. Binder. *A Guide to Monte Carlo Simulations in Statistical Physics*. Cambridge University Press, 2005.

[87] M. Y. Lavrentiev, D. Nguyen-Manh, and S. L. Dudarev. In: *Phys. Rev. B* 81 (2010), p. 184202.

[88] M. Y. Lavrentiev et al. In: *Phys. Rev. B* 84 (2011), p. 144203.

[89] M. Y. Lavrentiev et al. In: *Physical Chemistry Chemical Physics* 16 (2014), p. 16049.

[90] M. Y. Lavrentiev et al. In: *J. Appl. Phys.* 120 (2016), p. 043902.

[91] V. A. Lazarev and V. M. Golikov. In: *Fiz. Metal. Metalloved* 29 (1970), p. 598.

[92] A. D. Leclaire. "Physical Chemistry: An advance treatise". In: 10 (1970).

[93] M. Levesque et al. In: *Phys. Rev. B* 84 (2011), p. 184205.

[94] C. Li, F. Sommer, and E. J. Mittemeijer. In: *Mater. Sci. Engin.* A325 (2002), p. 307.

[95] A. J. Liechtenstein et al. In: *J. Magn. Magn. Mater.* 67 (1987), p. 65.

[96] S. Lintzen et al. In: *J. Alloys. Comp..* 577 (2013), p. 370.

[97] P. Liu et al. In: *Phys. Rev. B* 90 (2014), p. 024103.

[98] G. Lucas and R. Schaüblin. In: *Nucl. Instrum. Meth. B* 267 (2009), p. 3009.

[99] M. Luebbehusen. "Diploma work, Univ. Muenster". 1984.

[100] M. Luebbehusen and H. Mehrer. In: *Acta Metall. Mater.* 36 (1988), p. 2811.

[101] P.-W. Ma and S. L. Dudarev. In: *Phys. Rev. B* 91 (2015), p. 054420.

[102] E. Martinez and C-. C. Fu. In: *Phys. Rev. B* 84 (2011), p. 014203.

[103] E. Martinez et al. In: *Phys. Rev. B* 86 (2012), p. 224109.

[104] H. Matsui, S. Takehana, and M. W. Guinan. In: *J. Nucl. Mater.* 155-157 (1988), p. 1284.

[105] N. I. Medvedeva, D. C. Van Aken, and J. E. Medvedeva. In: *J. Phase Equilibria* 23 (2011), p. 32.

[106] H. Mehrer, D. Hoepfel, and G. Hettich. *DIMETA 82, Diffusion in Metals and Alloys*. Trans. Tech. Publ., Switzerland, 1983.

[107] L. Messina et al. In: *Phys. Rev. B* 90 (2014), p. 104203.

[108] L. Messina et al. In: *Phys. Rev. B* 93 (2016), p. 184302.

[109] M Methfessel and A T Paxton. In: *Phys. Rev. B* 40 (1989), p. 3616.

[110] A. A. Mirzoev, M. M. Yalalov, and D. A. Mirzaev. In: *Phys. Met. Metall.* 101 (2006), p. 341.

[111] Y. Mishin, J. Schimmelpfennig, and G. Borchardt. In: *J. Physique* 7 (1997), p. 1797.

[112] H J Monkhorst and J D Pack. In: *Phys. Rev. B* 13 (1976), p. 5188.

[113] H. A. Mook, J. W. Lynn, and R. M. Nicklow. In: *Phys. Rev. Lett.* 30 (1973), p. 556.

[114] C. Moran, C. Ederer, and M. Faehnle. In: *Phys. Rev. B* 67 (2003), p. 012407.

[115] E. G. Moroni et al. In: *Phys. Rev. B* 56 (1997), p. 15629.

[116] A. Moslang et al. In: *Hyperfine Int.* 15 (1983), p. 409.

[117] G. E. Murch and S. J. Rothman. In: *Philos. Mag. A.* 43 (1981), p. 229.

[118] D. Music et al. In: *Appl. Phys. Lett.* 91 (2007), p. 191904.

[119] Y. Nakai and N. Kunitomi. In: *J. Phys. Soc. Jpn* 39 (1975), p. 1257.

[120] J. Neugebauer and T. Hickel. "Density Functional Theory in Materials Science". In: 3 (Sept. 2013), pp. 438–448.

[121] A. S. Nikonenko. In: *Fiz. Metal. Metalloved* 16 (1963), p. 776.

[122] P. Olsson, I. A. Abrikosov, and J. Wallenius. In: *Phys. Rev. B* 73 (2006), p. 104416.

[123] P. Olsson, C. Domain, and J. Wallenius. In: *Phys. Rev. B* 75 (2007), p. 014110.

[124] P. Olsson, T. P. C. Klaver, and C. Domain. In: *Phys. Rev. B* 81 (2010), p. 054102.

[125] P. Olsson et al. In: *J. Nucl. Mater.* 321 (2003), p. 84.

[126] C. Paduani et al. In: *J. Appl. Phys.* 70 (1991), p. 7524.

[127] M. Pajda et al. In: *Phys. Rev. B* 64 (2001), p. 174402.

[128] G. Parette. In: *J. Appl. Phys.* 69 (1991), p. 6135.

[129] J. P. Perdew, K. Burke, and M. Ernzerhof. In: *Phys. Rev. Lett.* 77 (1999), p. 3865.

[130] V. Pierron-Bohnes, P. Cadeville, and F. Gauthier. In: *J. Phys. F: Met. Phys.* 82 (1983), p. 184430.

[131] S. S. Pohlong and P. N. Ram. In: *J. Phase Equilibria* 10 (1999), p. 10901.

[132] P. Radhakrishna and F. Livet. In: *Solid State Commun.* 25 (1978), p. 597.

[133] S. J. Rothman et al. In: *J. Appl. Phys.* 39 (1968), p. 5041.

[134] A. V. Ruban and V. I. Razumovskiy. In: *Phys. Rev. B* 86 (2012), p. 174111.

[135] A. V. Ruban et al. In: *Phys. Rev. B* 75 (2007), p. 054402.

[136] M. Rubinstein, G. H. Strauss, and J. Dweck. In: *Phys. Rev. Lett.* 17 (1966), p. 41.

[137] L. Ruch et al. In: *J. Phys. Chem. Solids* 37 (1976), p. 469.

[138] C. Sadron. In: *Ann. Phys. Paris* 17 (1932), p. 371.

[139] G. Salje and M. Feller-Knieppmeier. In: *J. Appl. Phys.* 48 (1977), p. 1833.

[140] N. Sandberg et al. In: *Phys. Rev. B* 92 (2015), p. 184102.

[141] A. Satta, F. Willaime, and S. De Gironcoli. In: *Phys. Rev. B* 57 (1998), p. 11184.

[142] A. Satta, F. Willaime, and S. De Gironcoli. In: *Phys. Rev. B* 60 (1999), p. 7001.

[143] O. Schneeweiss et al. In: *Phys. Rev. B* 96 (2017), p. 014437.

[144] E. Schrödinger. In: *Adv. Phys.* 385 (1926), p. 437.

[145] A. Seeger. In: *Phys. Stat. Sol.* 167 (198), p. 289.

[146] O. Senninger et al. In: *Acta Mater.* 73 (2014), p. 97.

[147] V. A. Shabashov et al. In: *Philos. Mag.* 20 (2017).

[148] S. Shallcross et al. In: *Phys. Rev. B* 73 (2006), p. 104443.

[149] D. A. Shirley, S. S. Rosenblum, and E. Mathias. In: *Phys. Rev.* 170 (1968), p. 363.

[150] P. Soederlind et al. In: *Phys. Rev. B* 61 (2000), p. 2579.

[151] F. Soisson, A. Barbu, and G. Martin. In: *Acta Mater.* 44 (1996), p. 3789.

[152] F. Soisson and C-. C. Fu. In: *Phys. Rev. B* 76 (2007), p. 214102.

[153] J. M. Soler et al. In: *J. Phase Equilibria* 14 (2002), p. 2745.

[154] R Soulairol, Cyrille Barreteau, and Chu-Chun Fu. In: *Phys. Rev. B* 94 (2016), p. 024427.

[155] R. Soulairol, C-. C. Fu, and C. Barreteau. In: *Phys. Rev. B* 84 (2011), p. 155402.

[156] G. R. Speich, J. A. Gula, and R. M. Fisher. *The electron Microprobe*. Wiley, New York.

[157] D Spisak and J. Hafner. In: *J. Magn. Magn. Mater.* 168 (1997), p. 257.

[158] M. B. Stearns and S. S. Wilson. In: *Phys. Rev. Lett.* 13 (1964), p. 313.

[159] K. Tapasa et al. In: *Acta Mater.* 55 (2007), p. 1.

[160] A Togo and I Tanaka. In: *Scr. Mater.* 108 (2015), p. 1.

[161] M. Van Schilfgaarde and V. P. Antropov. In: *J. Appl. Phys.* 85 (1999), p. 4827.

[162] E. Vincent, Becquart C., and C. Domain. In: *Nucl. Instrum. Meth. B* 228 (2005), p. 137.

[163] E. Vincent, Becquart C., and C. Domain. In: *J. Nucl. Mater.* 351 (2006), p. 88.

[164] G. H. Vineyard. In: *J. Phys. Chem. Solids* 3 (1957), p. 21.

[165] O. Vollmer, R. Kohlhass, and M. Braun. In: *Z. Naturforschg.* 21 (1966), p. 181.

[166] O. Vollmer, R. Kohlhass, and M. Braun. In: *Z. Naturforschg.* 21 (1966), p. 181.

[167] M. Von Smoluchowski. In: *Adv. Phys.* 21 (1906), p. 756.

[168] D. C. Wallace, P. H. Sidles, and G. C. Danielson. In: *J. Appl. Phys.* 31 (1960), p. 168.

[169] J. Wallenius et al. In: *Phys. Rev. B* 69 (2004), p. 094103.

[170] C. M. Walter and N. L. Peterson. In: *Phys. Rev.* 178 (1969), p. 922.

[171] C. S. Wang, B. M. Klein, and H. Krakauer. In: *Phys. Rev. Lett.* 54 (1985), p. 1852.

[172] B. E. Warren. "X-ray diffraction". In: (1990).

[173] H. Wen, P. W. Ma, and C. Woo. In: *J. Nucl. Mater.* 440 (2013), p. 428.

[174] H. Wen and C. Woo. In: *J. Nucl. Mater.* 470 (2016), p. 102.

[175] G. K. Wertheim et al. In: *Phys. Rev. Lett.* 12 (1964), p. 24.

[176] V. T. Witusiewicz, F. Sommer, and E. J. Mittemeijer. In: *J. Phase Equil. Diff.* 25 (2004), pp. 346–354.

[177] C. Wolverton, V. Ozolins, and M. Asta. In: *Phys. Rev. B* 69 (2004), p. 1440109.

[178] K. L. Wong et al. In: *J. Nucl. Mater.* 227 (2009), p. 386.

[179] C. Woo et al. In: *Phys. Rev. B* 91 (2015), p. 104306.

[180] X. Wu, Z. Liu, and T. Luo. In: *J. Appl. Phys.* 123 (2018), p. 085109.

[181] H. Yamauchi et al. In: *J. Phys. Soc. Jpn* 36 (1974), p. 971.

[182] Y. You and M. F. Yan. In: *Physica B* 417 (2013), p. 57.

[183] R. Zeller. In: *J. Phys. F: Met. Phys.* 17 (1987), p. 2123.

[184] A. Zunger et al. In: *Phys. Rev. Lett.* 65 (1990), p. 353.

université PARIS-SACLAY
ÉCOLE DOCTORALE
Ondes et Matière (EDOM)

Titre : Corrélations entre le magnétisme, la thermodynamique et la diffusion dans les alliages Fe-Mn cubiques centrés : des premiers principes aux températures finies

Mots clés : magnétisme, thermodynamique, diffusion, simulation atomistique

Résumé : Dans les alliages $3d$, les propriétés magnétiques des solutés peuvent être extrêmement sensibles aux environnements chimiques locaux, et avoir un impact crucial sur diverses propriétés thermodynamiques et cinétiques.
Afin de comprendre les propriétés fondamentales de ces alliages, la première partie de ce travail est dédiée à l'étude ab-initio des effets de l'environnement chimique local sur l'état magnétique des solutés de Mn dans le Fe-Mn. Diverses configurations contenant du Mn, isolé ou sous forme d'amas, en présence de lacunes ou d'impuretés interstitielles sont étudiées et leur configuration magnétique de plus basse énergie est déterminée.
Un modèle effectif d'interactions est paramétré à partir des données ab-initio afin d'étudier les propriétés des alliages Fe-Mn à température finie. Les propriétés clés sont identifiées et le modèle est validé à basse température en reproduisant les résultats ab-initio. L'utilisation de ce modèle couplé à des simulations Monte Carlo permet de simuler l'évolution chimique des alliages Fe-Mn en fonction de la température et de la concentration en Mn, tout en relaxant la structure magnétique en temps réel. Afin d'illustrer les possibles applications de ce modèle, diverses propriétés sont étudiées telles que la dépendance en concentration de la température de Curie ou encore l'évolution en température de l'énergie de mélange et de l'ordre atomique à courte distance.
Puisque dans ces alliages la diffusion est en général régie par mécanisme lacunaire, nous proposons aussi un formalisme prenant en compte explicitement les effets de l'ordre magnétique local sur les propriétés des lacunes. Par simulations Monte Carlo de traceurs, cette approche prédit la dépendance en température de l'auto-diffusion dans le Fe en excellent accord avec les études expérimentales. La déviation de la loi d'Arrhénius proche de la température de Curie est directement prédite, ainsi que le changement de pente entre les régimes ferromagnétique et paramagnétique. La précision du modèle de Ruch, couramment utilisé dans la littérature, est discutée au vu des résultats obtenus. Enfin, cette approche est appliquée à la diffusion d'un soluté de Mn dans le Fe pur et comparée aux résultats expérimentaux.

Title : Interplay between magnetism, thermodynamics and diffusion in bcc Fe-Mn alloys : from first principles to finite temperatures

Keywords : magnetism, thermodynamics, diffusion, atomistic simulation

Abstract : In $3d$ alloys, magnetic properties of solutes can be extremely sensitive to local chemical environments and can have a crucial impact on various thermodynamic and kinetic properties.
In order to properly understand the fundamental properties of these alloys, the first part of this work is dedicated to the study of the effects of local chemical environment on the magnetic state of Mn solutes in bcc Fe-Mn by means of Density Functional Theory. Namely, configurations containing Mn, being isolated or forming a cluster, and in the presence of vacancies or interstitial impurities are investigated and their lowest-energy magnetic configuration is determined.
The ab-initio data produced are then used to parameterize an effective interaction model in order to study the properties of Fe-Mn alloys at finite temperature. The key features of Fe-Mn alloys are identified, and the model is validated at low temperature by reproducing ab-initio predictions. Using this model coupled to Monte Carlo simulations, we simulate the chemical evolution of Fe-Mn properties depending on temperature and Mn concentration while relaxing the magnetic structure on-the-fly. In order to illustrate the validity and the applicability of the model, we examine certain finite temperature properties of bcc Fe-Mn alloys such as the concentration dependence of the Curie temperature or the temperature evolution of the mixing energy and the atomic short-range order.
Since diffusion in Fe and Fe-Mn alloys is generally ruled by vacancy-mechanism, we also propose a formalism to take explicitly into account the properties of vacancies in the interaction model and the effect of local magnetic state on these properties. Using tracer diffusion Monte Carlo simulations, this approach predicts the temperature dependence of self-diffusion in bcc Fe in excellent agreement with experimental results, including the deviation from Arrhenius law around the Curie temperature and the change of slope between the ferromagnetic and paramagnetic regimes. The accuracy of the widely used Ruch model is discussed in the light of the present results. Finally, we apply this approach to the diffusion of a Mn solute in bcc Fe and compare with experimental results.

Université Paris-Saclay
Espace Technologique / Immeuble Discovery
Route de l'Orme aux Merisiers RD 128 / 91190 Saint-Aubin, France